NASA/CR—2012-217416

A Computational Study for the Utilization of Jet Pulsations in Gas Turbine Film Cooling and Flow Control

Final Report

Olga V. Kartuzova
Cleveland State University, Cleveland, Ohio

Notice for Copyrighted Information

September 2012

NASA STI Program . . . in Profile

Since its founding, NASA has been dedicated to the advancement of aeronautics and space science. The NASA Scientific and Technical Information (STI) program plays a key part in helping NASA maintain this important role.

The NASA STI Program operates under the auspices of the Agency Chief Information Officer. It collects, organizes, provides for archiving, and disseminates NASA's STI. The NASA STI program provides access to the NASA Aeronautics and Space Database and its public interface, the NASA Technical Reports Server, thus providing one of the largest collections of aeronautical and space science STI in the world. Results are published in both non-NASA channels and by NASA in the NASA STI Report Series, which includes the following report types:

- TECHNICAL PUBLICATION. Reports of completed research or a major significant phase of research that present the results of NASA programs and include extensive data or theoretical analysis. Includes compilations of significant scientific and technical data and information deemed to be of continuing reference value. NASA counterpart of peer-reviewed formal professional papers but has less stringent limitations on manuscript length and extent of graphic presentations.

- TECHNICAL MEMORANDUM. Scientific and technical findings that are preliminary or of specialized interest, e.g., quick release reports, working papers, and bibliographies that contain minimal annotation. Does not contain extensive analysis.

- CONTRACTOR REPORT. Scientific and technical findings by NASA-sponsored contractors and grantees.

- CONFERENCE PUBLICATION. Collected papers from scientific and technical conferences, symposia, seminars, or other meetings sponsored or cosponsored by NASA.

- SPECIAL PUBLICATION. Scientific, technical, or historical information from NASA programs, projects, and missions, often concerned with subjects having substantial public interest.

- TECHNICAL TRANSLATION. English-language translations of foreign scientific and technical material pertinent to NASA's mission.

Specialized services also include creating custom thesauri, building customized databases, organizing and publishing research results.

For more information about the NASA STI program, see the following:

- Access the NASA STI program home page at *http://www.sti.nasa.gov*

- E-mail your question to *help@sti.nasa.gov*

- Fax your question to the NASA STI Information Desk at 443–757–5803

- Telephone the NASA STI Information Desk at 443–757–5802

- Write to:
  STI Information Desk
  NASA Center for AeroSpace Information (CASI)
  7115 Standard Drive
  Hanover, MD 21076–1320

NASA/CR—2012-217416

A Computational Study for the Utilization of Jet Pulsations in Gas Turbine Film Cooling and Flow Control

Final Report

Olga V. Kartuzova
Cleveland State University, Cleveland, Ohio

Prepared under NASA Interagency Agreement No. NNC07IA10I
(through U.S. Navy Agreement No. N00189–07–P–A253)
Prepared under Grant No. DE–FC26–06NT42853

National Aeronautics and
Space Administration

Glenn Research Center
Cleveland, Ohio 44135

September 2012

Acknowledgments

The author gratefully acknowledges the National Aeronautics and Space Administration for sponsoring the airfoil flow control work. Dr. Anthony J. Strazisar, Dr. James D. Heidmann, and Dr. David E. Ashpis of the NASA Glenn Research Center served as grant technical monitors. The computer time provided by the Ohio Super Computer (OSC), which has been made available as part of the center's mission to support Ohio Universities, is greatly appreciated. The author is grateful to the International Gas Turbine Institute (IGTI) for supporting a trip to the ASME Turbo Expo 2009 conference to present work on the L1A airfoil flow control. The author would like to thank the Mechanical Engineering Department of the Cleveland State University, U.S. Department of Energy and Zonta International Amelia Earhart Fellowship for the partial financial support of this project. The author would also like to thank advisor Dr. Mounir Ibrahim for his great help and constructive advice during the course of this research. Thanks also due to Dr. Ralph Volino from the U.S. Naval Academy for numerous discussions, advice, and experimental data he provided for validating computational models used in this work.

This work was sponsored by the Fundamental Aeronautics Program at the NASA Glenn Research Center.

Level of Review: This material has been technically reviewed by NASA technical management.

Available from

NASA Center for Aerospace Information
7115 Standard Drive
Hanover, MD 21076–1320

National Technical Information Service
5301 Shawnee Road
Alexandria, VA 22312

Available electronically at http://www.sti.nasa.gov

A Computational Study for the Utilization of Jet Pulsations in Gas Turbine Film Cooling and Flow Control

by Olga V. Kartuzova

ABSTRACT

Jets have been utilized in various turbomachinery applications in order to improve gas turbines performance. Jet pulsation is a promising technique because of the reduction in the amount of air removed from compressor, which helps to increase turbine efficiency. In this work two areas of pulsed jets applications were investigated, first one is film cooling of High Pressure Turbine (HPT) blades and second one is flow separation control over Low Pressure Turbine (LPT) airfoil using Vortex Generator Jets (VGJ)

The inlet temperature to the HPT significantly affects the performance of the gas turbine. Film cooling is one of the most efficient methods for cooling turbine blades. This technique is simply employing cool air discharged from rows of holes into the hot stream. Using pulsed jets for film cooling purposes can help to improve the effectiveness and thus allow higher turbine inlet temperature without affecting the blade's life. Engine cost will thus be reduced by providing the same capacity from smaller, lighter engines. Fuel consumption will be lowered, resulting in lower fuel cost. Effects of the film hole geometry, blowing ratio and density ratio of the jet, pulsation frequency and duty cycle of blowing on the film cooling effectiveness were investigated in the present work.

As for the low-pressure turbine (LPT) stages, the boundary layer separation on the suction side of airfoils can occur due to strong adverse pressure gradients. The problem is exacerbated as airfoil loading is increased. If the boundary layer separates, the lift from the airfoil decreases and the aerodynamic loss increases, resulting in a drop in an overall engine efficiency. A significant increase in efficiency could be achieved if separation could be prevented, or minimized. Active flow control could provide a means for minimizing separation under conditions where it is most severe (low Re), without causing additional losses under other conditions (high Re). Minimizing separation will allow improved designs with fewer stages and fewer airfoils per stage to generate the same power. The effects of the jet geometry, blowing ratio, density ratio, pulsation frequency and duty cycle on the size of the separated region were examined in this work. The results from Reynolds Averaged Navier-Stokes and Large Eddy Simulation computational approaches were compared with the experimental data.

TABLE OF CONTENTS

Page

ABSTRACT .... **iii**

NOMENCLATURE .... **vii**

LIST OF TABLES .... **ix**

LIST OF FIGURES .... **x**

CHAPTER

I. INTRODUCTION **1**

1.1 Pulsed Jets Film Cooling 1

1.2 Flow Separation Control over LPT airfoil Using Pulsed VGJs 2

II. NUMERICAL METHODS AND TURBULENCE MODELS **5**

2.1 Equations solved 5

2.2 Turbulence Modeling 6

2.2.1 The standard $k-\varepsilon$ model (SKE) 7

2.2.2 The standard $k-\omega$ model (SKW) 7

2.2.3 The realizable $k-\varepsilon$ model (RKE) 8

2.2.4 The shear-stress transport $k-\omega$ model (SKW-sst) 9

2.2.5 The v^2-f model (V2F) 10

2.2.6 The Transition-sst (4 equations) model (Trans-sst) 11

2.2.7 Large Eddy Simulation (LES) 14

III. PART 1: PULSED JETS FILM COOLING **17**

3.1 Literature Review 17

3.2 Computational model and boundary conditions 19

3.2.1 Cylindrical film hole geometry 20

3.2.2 Film hole with laterally diffused exit 22

3.3 Results and discussion 23

3.3.1 Code validation 23

3.3.2 Effect of Pulsation Frequency 29

3.3.3 Effect of Jet Blowing Ratio 46

3.3.4 Effect of Jet geometry 52

3.3.5 Spatially Averaged Film Cooling Effectiveness 56

IV. PART 2: FLOW CONTROL OVER LPT AIRFOIL USING PULSED VGJs .. 62

4.1 Literature Review 62

4.1.1 Flow Separation and Transition on LPT Airfoils 62

4.1.2 Airfoil Flow Control 65

4.2 Experimental Facility and Measurements Conducted at US Naval Academy ... 69

4.3 Computational model 74

4.3.1 Grid independence study 76

4.3.2 Boundary conditions influence study 79

4.4 Separated flow predictions 83

4.4.1 Pressure profiles 84

4.4.2 Total pressure losses 87

4.4.3 Velocity profiles 90

4.4.4 Prediction of Transition 95

4.4.5 Effects of free stream turbulence on separation 100

4.5 Flow Control using Steady VGJs 114

4.5.1 Re = 25,0000 ... 114
4.5.1 Re = 50,000 ... 120
4.5.2 Re = 100,000 ... 124
4.6 Flow Control Using Pulsed VGJs ... 130
4.6.1 Pressure and velocity distributions ... 130
4.6.2 Velocity Contours at Jet Exit ... 140
4.6.3 Effect of Re and Blowing Characteristics ... 144
4.6.4 Flow visualization utilizing the *Q*-Criterion ... 145

V. CONCLUDING REMARKS ... 149
5.1 Film cooling ... 149
5.2 Flow control ... 150

BIBLIOGRAPHY ... 154

NOMENCLATURE

Symbols

B	blowing ratio
$C_p = 2(P_T - P)/\rho U_e^2$	pressure coefficient
C_x	axial chord length, m
D	diameter, m
DC	duty cycle, ratio of the time when the flow is on to the cycle time
e	internal energy per unit mass
$F = fL_{j\text{-}te}/U_{ave}$	dimensionless frequency
f	frequency, Hz
k	coefficient of thermal conductivity, W/(m·K)
k	kinetic energy of turbulence, m^2/s^2
L	length of film cooling tube, m
L_ϕ	blade spacing (pitch), m
LE	leading edge
$L_{j\text{-}te}$	distance from VGJs to trailing edge, m
L_s	suction surface length, m
P	pressure, Pa
P_S	upstream static pressure, Pa
P_T	upstream stagnation pressure, Pa
P_{Te}	downstream stagnation pressure, Pa
$Re = U_e L_s / \nu$	exit Reynolds number
$Re_\theta = U_\infty \theta / \nu$	momentum thickness Reynolds number
$Re_{\theta t}$	transition momentum thickness Reynolds number
s	streamwise coordinate, distance from leading edge, m
S_{ij}	mean strain tensor
$St = fD/U_\infty$	Strouhal number
T	local fluid temperature, K
t	time, s
TE	trailing edge
TI	turbulence intensity, %
tke	turbulence kinetic energy, m^2/s^2
U	fluid streamwise velocity magnitude, m/s
u'	RMS of the fluctuating component of the streamwise velocity
U_∞	freestream velocity m/s
U_{ave}	average freestream velocity between VGJs and trailing edge m/s
U_e	nominal exit freestream velocity, based on inviscid solution, m/s
$\mathbf{V}$	Velocity vector
x	streamwise distance, m
y	vertical distance, m
$y^+ = y(\tau_w/\rho_w)^{1/2}/\nu_w$	non-dimensional wall distance, m
z	distance in the spanwise direction, m
α_1	inlet flow angle
α_2	exit flow angle
γ	intermittency

$\eta = (T_{aw}-T_\infty)/(T_{jet}-T_\infty)$	adiabatic film cooling effectiveness
ε	turbulence dissipation rate
θ	momentum thickness
μ	dynamic viscosity, kg/(m·s)
μ_T	eddy viscosity
ρ	density, kg/m^3
ϕ	coordinate along blade spacing, normal to axial chord, m
$\psi = (P_T-P_{Te})/(P_T-P_S)$	total pressure loss coefficient
ν	kinematic viscosity, m^2/s

Subscripts

aw	adiabatic wall
c	coolant flow characteristics
fh	film hole
jet	film cooling jet characteristics
∞	mainstream
p	pressure minimum (suction peak) location
pt	distance from suction peak to transition start
s	separation location
t	transition start

Abbreviations

CFH	Cylindrical Film Hole geometry
HPT	High Pressure Turbine
LDIFF	Film hole geometry with Laterally Diffused exit
LES	Large Eddy Simulation
LPT	Low Pressure Turbine
RKE	Realizable k - ε turbulence model of Shih et al., (1994)
SKE	Standard k - ε turbulence model of Launder and Spalding (1974)
SKW	Standard k - ω turbulence model of Wilcox (1998)
SKW-sst	Shear Stress Transport k - ω turbulence model of Menter (2006)
Trans-sst	Transition-sst turbulence model of Menter et al., (2006)
URANS	Unsteady Reynolds Averaged Navier-Stokes
V2F	$\overline{v^2} - f$ turbulence model of Durbin, (1995)
VGJ	Vortex Generator Jets

LIST OF TABLES

Table Page

3.1: Pulsed jet film cooling cases simulated………………………………………... 19

3.2: Spatially averaged film cooling effectiveness ($\overline{\eta}$) for all cases examined…….. 58

4.1: Grid characteristics for grid independence study…………………………..... 76

4.2: Grids characteristics for the flow control study………………………………... 77

4.3: Specifications of computational grid 6………………………………………... 77

4.4: Tested inlet boundary conditions at Re=100,000…………………...……..... 82

4.5: Velocity profile measurement stations……………………………………..... 90

4.6: CFD results for separation and transition locations (Trans-sst Model)…..……. 97

4.7: Experimental Results for separation and transition locations………………….. 97

4.8: Pulsed VGJs Test Matrix (NA = not available)……………………………….….. 130

4.9: Main Parameters of all Pulsed VGJs Cases Examined (NA = Not Available)... 144

LIST OF FIGURES

Figure Page

1.1: Components of the jet engine ……………………………………………… 2

1.2: The air flow through the jet engine …………………………………………… 3

3.1: A schematic of the experimental test setup for Coulthard et al., (2006) CFH geometry, including extent of the computational domain (dashed lines) and boundary conditions……... 21

3.2: A schematic of the LDIFF film hole shape of Hyams and Leylek (2000)……………………………………………………………………... 22

3.3: Centerline plot of adiabatic effectiveness with different turbulence models, compared to experimental data (CFH geometry, B=0.5, steady blowing)…….. 24

3.4: Centerline adiabatic film cooling effectiveness, B - 0.5, data from various experimental and computational studies compared to present work. (CFH geometry)…………………………………………………………………. 26

3.5: Centerline adiabatic film cooling effectiveness, steady state, B = 1.5 compared to DNS and experimental data (CFH geometry)…………………… 28

3.6: Centerline plot of time averaged adiabatic film cooling effectiveness for B = 0.5, St=0.0119 and St=0.19, compared to experimental results (CFH geometry)………………………………………………………………… 28

3.7: Centerline-(a) and spanwise averaged-(b) plot of adiabatic film cooling effectiveness for B = 0.5 steady state and different Strouhal numbers………... 30

3.8: Effectiveness footprints on the test wall downstream of the film hole, B = 0.5, (a) steady state; (b) St = 0.0119; (c) St = 0.19; (d) St = 0.38 (CFH geometry)…………………………………………………………………. 34

3.9: CFH geometry, B=0.5: velocity magnitude contours and vectors (m/s), (a) steady blowing; (c) no blowing and dimensionless temperature sideview, (b) steady state; (d) no blowing…………………………………………………. 36

3.10: LDIFF geometry: velocity magnitude contours and vectors B=1.25 steady blowing - (a), no blowing - (c); dimensionless temperature sideview B=1.25 steady state - (b), no blowing - (d) (Notice: equal size velocity vectors are shown in order to indicate the flow stream)…………………………………… 39

3.11: B = 0.5, St = 0.0119 (a) velocity magnitude contours(m/s) and vectors; (b) dimensionless temperature sideview; (c) dimensionless temperature contours at the jet-top……………………………………………………………………. 41

3.12: B = 0.5, St = 0.19 (a) velocity magnitude contours (m/s) and vectors; (b) dimensionless temperature sideview; (c) dimensionless temperature contours at the jet-top………………………………………….…………… 43

3.13: B = 0.5, St = 0.38 (a) velocity magnitude contours(m/s) and vectors; (b) dimensionless temperature sideview; (c) dimensionless temperature contours at the jet-top……………………………………………………….. 45

3.14: Centerline - (a) and spanwise averaged (b) plot of adiabatic film cooling effectiveness for B = 1.5 steady blowing and different Strouhal numbers (CFH geometry)……………………..………………………………….… 47

3.15: Effectiveness footprints on the test wall downstream of the film hole, B = 1.5 (a) steady blowing; (b) St = 0.38……………………...…………………… 48

3.16: Dimensionless temperature sideview, B = 1.5 (a) steady blowing; (b) St = 0.0119; (c) St = 0.38; (d) St = 1…………….…………………………… 52

3.17: Film hole geometry effect on the time averaged, adiabatic film cooling effectiveness. (LDIFF geometry): a - centerline, b - spanwise averaged……… 53

3.18: Effectiveness footprints on the downstream wall, B = 1.25, LDIFF geometry a) - steady state, b) - St = 0.0119, c) - St = 0.0119…………………………... 56

3.19: Film cooling characteristics, averaged over x/D = 10 by z/D = 3 area, for all film cooling cases examined…………………………………………………… 57

4.1: Schematic of a linear cascade of 7 airfoils (Volino (2008)) with boundary conditions and computational domain used in baseline study (without VGJs), shown in dashed lines……………………………………………………….. 70

4.2: Airfoil with VGJ holes and cross section of the jet geometry………………… 72

4.3: Grid Independence Study for the Flow Control cases (Re = 50,000, B=2, Steady Jets, dt = 0.0001 s)…………………………………………………... 78

4.4: Time step size effect study for the Flow Control cases (Re = 50,000, B=2, Steady Jets, grid 6)……………………………………………………………... 79

4.5: Three dimensional computational grid 6 a) in the jet vicinity, b) near leading edge of the airfoil, c) near trailing edge of the airfoil………………………….. 80

4.6: C_p profiles, *Re*=25,000…………………………………………………… 85

4.7: C_p profiles, *Re*=100,000……………………………………………………... 86

4.8: C_p profiles, *Re*=300,000……………………………………………………... 86

4.9: Pressure loss coefficients at 0.63 C_x downstream of the cascade, Re=25,000… 88

4.10: Pressure loss coefficients at 0.63 C_x downstream of the cascade, *Re*=100,000. 89

4.11: Pressure loss coefficients at 0.63 C_x downstream of the cascade, *Re*=300,000. 90

4.12: Mean velocity profiles, Re = 25,000………………………………………… 91

4.13: Comparison of Trans-sst and experimental u'/U_e profiles, Re= 25,000……… 92

4.14: Mean velocity profiles, *Re* = 100,000……………………………………… 93

4.15: Comparison of Trans-sst and experimental u'/U_e profiles, Re= 100,000…….. 94

4.16: Mean velocity profiles, *Re* =300,000……………………………………… 95

4.17: Comparison of Trans-sst and experimental u'/U_e profiles, Re= 300,000…….. 96

4.18: Contours of u'/U_e, and velocity vectors (for Transition model) showing the location of: 1) suction peak, 2) separation and 3) transition for a) *Re* = 25,000, b) Re = 100,000, and c) Re = 300,000……………………………………… 98

4.19: Comparison between CFD data (Trans-sst Model) and correlation for the start of transition……………………………………………………….. 99

4.20: Flow field on suction side of airfoil showing turbulent kinetic energy (contours) and mean velocity (vectors): a) *Re*=25,000, b) *Re*=100,000, c) *Re*=300,000 (HFSTI)………………………………………………….. 101

4.21: C_p profiles comparing simulations to experiment: a) *Re*=25,000, b) *Re*=100,000, c) *Re*=300,000 (HFSTI)………………………………… 104

4.22: Comparison of computed and measured mean velocity profiles, *Re*=25,000 (HFSTI)……………………………………………………………... 105

4.23: Comparison of computed with Trans-sst model and measured u'/U_e profiles, *Re*=25,000 (HFSTI)………………………………………………… 106

4.24: Comparison of computed and measured mean velocity profiles, *Re*=100,000 (HFSTI)……………………………………………………………... 108

4.25: Comparison of computed with Trans-sst model and measured u'/U_e profiles, *Re*=100,000 (HFSTI)……………………………………………….. 109

4.26: Comparison of computed and measured mean velocity profiles, *Re*=300,000 (HFSTI)……………………………………………………………... 110

4.27: Comparison of computed with Trans-sst model and measured u′/U_e profiles, *Re*=300,000 (HFSTI)………………………………………………………….. 111

4.28: Total pressure loss coefficient at 0.63 C_x downstream of cascade comparing simulations to experiment: a) *Re*=25,000, b) *Re*=100,000, c) *Re*=300,000 (HFSTI)……………………………………………………………..……. 113

4.29: Pressure coefficient on the airfoil for steady blown VGJs at Re = 25,000…… 115

4.30: Velocity profiles at six measurements stations on the airfoil's suction side for steady blown VGJs at Re = 25,000…………………………………………….. 117

4.31: RMS of the fluctuating component of the streamwise velocity at six measurements stations on the airfoil's suction side for steady blown VGJs at Re = 25,000, B=3……………………………………………………………. 118

4.32: Instantaneous isosurfaces of Vx=0.01 m/s for steady blown VGJs at Re = 25,000…………………………………………………………………….. 119

4.33: Instantaneous X-vorticity for steady blown VGJs at Re = 25,000…………… 120

4.34: Subgrid turbulence kinetic energy (TKE) at the spanwise oriented planes of 6 measurement stations for steady blown VGJs at Re = 25,000………………… 121

4.35: Pressure coefficient on the airfoil for steady blown VGJs at Re = 50,000…… 122

4.36: Velocity profiles at six measurements stations on the airfoil's suction side for steady blown VGJs at Re = 50,000…………………………………………….. 123

4.37: RMS of the fluctuating component of the streamwise velocity at six measurements stations on the airfoil's suction side for steady blown VGJs at Re = 50,000…………………………………………………………………….. 124

4.38: Pressure coefficient on the airfoil for steady blown VGJs at Re = 100,000….. 125

4.39: Velocity profiles at six measurements stations on the airfoil's suction side for steady blown VGJs at Re = 100,000…………………………………………… 126

4.40: RMS of the fluctuating component of the streamwise velocity at six measurements stations on the airfoil's suction side for steady blown VGJs at Re=100,000…………………………………………………………………….. 127

4.41: C_p for case (1) Re = 25,000, B = 1.0, f = 3 Hz (F = 0.14), DC = 10%............. 131

4.42: C_p for case (2) Re = 50,000, B = 0.5, f = 3 Hz (F = 0.07), DC = 10%............. 132

4.43: C_p for case (3) Re=100,000, B=0.25, f=3 Hz (F=0.035), DC=10%................. 132

4.44: C_p for case (4) Re = 25,000, B = 0.1, f = 12 Hz (F = 0.56), DC = 10%........... 134

4.45: C_p for case (5) Re = 50,000, B = 0.5, f = 12 Hz (F = 0.28), DC = 10%........... 134

4.46: C_p for case (6) Re = 50,000, B = 0.5, f = 24 Hz (F = 0.56), DC = 10%........... 135

4.47: C_p for case (7) Re = 50,000, B = 0.5, f = 12 Hz (F = 0.28), DC = 50%........... 135

4.48: Contours of streamwise velocity and velocity vectors for Case (6), Re=50,000, B=0.5, f=24 Hz (F=0.56), DC=10%... 136

4.49: U/Ue at the 6 stations for Case (6), Re=50,000, f=24 Hz, (F=0.56), DC=10% 137

4.50: u'/Ue at the 6 stations for Case (6), Re=50,000, f=24 Hz, (F=0.56), DC=10% 138

4.51: Isosurface of mean Vx = 0,01 m/s for Case (6), Re=50,000, f=24 Hz, (F=0.56), DC=10%.. 139

4.52: Velocity contours (m/s) at the jet exit for Case (2), Re=50,000, f=3Hz, (F=0.07), DC=10%.. 141

4.53: Velocity contours (m/s) at the jet exit for Case (5), Re=50,000, f=12 Hz, (F=0.28), DC=10%.. 142

4.54: Velocity contours (m/s) at the jet exit for Case (6), Re=50,000, B=0.5, f=24 Hz, (F=0.56), DC=10%... 142

4.55: Velocity contours (m/s) at the jet exit for Case (7), Re=50,000, B=0.5, f=12Hz, (F=0.28), DC=50%... 143

4.56: Comparison of measured and computed VGJ exit velocity with inlet velocity for B=1, f=12Hz, DC=50% case with no crossflow…………………………… 143

4.57: Iso-surfaces of the Q-criterion colored by Vx (m/s) at different times in the cycle for: a) Case (2), Re=50,000, B=0.5, f=3Hz (F=0.07), DC=50%; b) Case (6), Re=50,000, B=0.5,f=24Hz (F=0.56), DC=10%.. 147

CHAPTER I

INTRODUCTION

1.1 Pulsed Jets Film Cooling

Increased combustor exit temperatures result in improved gas turbine efficiency and reduced fuel consumption. In order to protect the surface, cool air from compressor stage ducted into the internal chambers of the turbine blades and discharged through small holes in the blade walls. The air covers the external surface of the blade with thin, cool insulating film. This cool film helps to protect surface materials from being damaged, even under elevated inlet temperature conditions. This technique, called film cooling, is used in modern high pressure gas turbines for improved efficiency. About 20-25% of compressor air is used for cooling high performance turbine engines (Ekkad et al., (2006)). Higher engine efficiency may be obtained by minimizing coolant mass flow with the same or higher film cooling effectiveness. Experimental studies (Ekkad et al., (2006)), found in the literature, showed that coolant flow pulsation might help to improve film cooling, while reducing the actual coolant flow rate. However, the effect of jet pulsation on the film cooling characteristics hasn't been studied extensively. Therefore it is important to investigate pulse frequency, blowing ratio and film hole geometry effects on film cooling, in order to identify under which conditions jet pulsation helps to increase film cooling effectiveness compared to the steady blowing and explain the flow physics behind that.

1.2 Flow Separation Control over LPT airfoil Using Pulsed VGJs

Modern gas turbines have high reliability, efficiency and power-to-weight ratio. They are used for airplane propulsion and for continuous electrical power generation.

In a typical jet engine for airplane propulsion (Fig. 1.1) the air enters the fan after which it is split into two parts and some of the flow bypasses the core of the engine and is ejected as a low speed, high volume jet (Fig. 1.2, blue arrows). The second portion of the flow passes through the core of the engine (compressors, combustion chambers and turbines) and is ejected as a high speed low volume jet (Fig. 1.2. red lines). The Low Pressure Turbine (LPT) powers the bypass flow, which produces around 80% of the thrust, when the core flow only contributes about 20% (Howell, 1999).

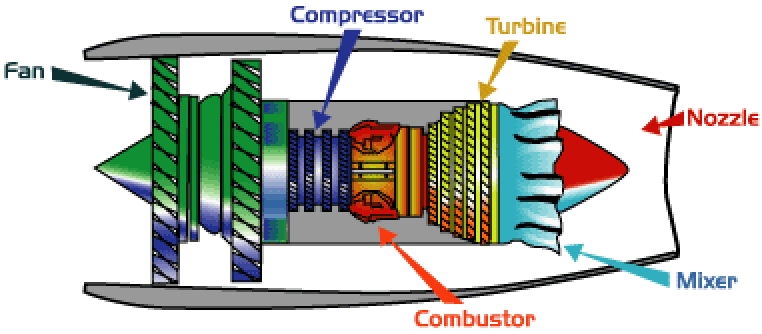

Figure 1.1: Components of the jet engine
(http://www.ueet.nasa.gov/StudentSite/engines.html)

The fan generates most of the thrust and requires several low pressure turbine stages to drive it, whereas a single stage High Pressure Turbine (HPT) might be enough to drive several stages High Pressure (HP) compressor.

The efficiency of the LPT significantly affects the overall engine fuel consumption. Typically, a 1% increase in LPT efficiency gives rise to 0.7% increase in engine overall efficiency. From the development of the first turbines to the present time LPT efficiencies increased from 80% to above 93% (Howell, 1999). It is increasingly hard to obtain a raise in LPT efficiency nowadays. Therefore, manufacturers are looking for other ways to make their products more competitive. The cost of the engine, its weight, its fuel consumption, maintenance and servicing costs create the total cost of ownership. The engine's weight, in fact, affects the production costs and fuel consumption. Because of the reduction of the number of components, the maintenance costs are smaller for the lighter engines.

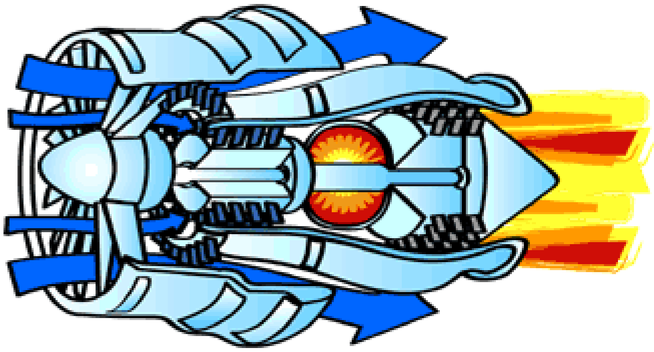

Figure 1.2 The air flow through the jet engine
(http://www.ueet.nasa.gov/StudentSite/engines.html)

Since the LPT is the heaviest single engine's component, it is of a prime interest to reduce its weight by reducing the number of blades. This requires each blade to be highly loaded, which creates strong adverse pressure gradients on the suction side of the airfoils. The result of this is flow separation.

Flow separation on the suction surface of the LPT airfoils often occurs when turbine engines operate at low Reynolds numbers, as in the case of aircraft engines at high altitude cruise conditions. Low Reynolds numbers can cause the boundary layer to remain laminar and easily separate. This laminar separation results in an engine efficiency drop and an increase in fuel consumption (Mayle (1999), Howell (1999) and Singh (2005)).

Simulation and prediction of transitional flow over LPT airfoils under a wide variety of Reynolds numbers, freestream turbulence parameters and with flow separation is essential for improvement in aircraft engine design. This will help to identify cases, where flow control can be implemented in order to increase engine efficiency. It is also important to conduct airfoil flow control studies in order to determine under which conditions flow separation can be significantly reduced or eliminated.

CHAPTER II

NUMERICAL METHODS AND TURBULENCE MODELS

Computational analysis in the present work was performed using commercial CFD code ANSYS Fluent version 6.3.26. For modeling laminar-turbulent transition newly implemented in ANSYS Fluent 12 Trans-sst turbulence model of Menter et al., (2006) was used. ANSYS Fluent is a general purpose finite volume CFD code, which description and equations solved could be found in ANSYS Fluent Documentation (2009).

2.1 Equations solved

A summary of the equations solved in the present study is presented below.

The equation for conservation of mass or continuity equation can be written for incompressible flow (considered in the present work) as follows:

$$\boldsymbol{\nabla} \cdot \mathbf{V} = 0, \tag{2.1}$$

where $\mathbf{V}$ is the velocity vector.

Conservation of momentum for incompressible flow with constant viscosity is described as follows:

$$\rho\frac{D\mathbf{V}}{Dt} = \rho\boldsymbol{g} - \boldsymbol{\nabla}p + \mu\boldsymbol{\nabla}^2\mathbf{V}, \tag{2.2}$$

where p is the static pressure, μ is the molecular viscosity, and $\rho\boldsymbol{g}$ is the gravitational body force.

The energy equation for the incompressible flow with constant coefficient of thermal conductivity has the following form:

$$\rho\frac{D\mathrm{e}}{Dt} = \frac{\partial Q}{\partial t} + k\nabla^2 T + \Phi, \tag{2.3}$$

where e is an internal energy per unit mass, k is the thermal conductivity, Q is external heat addition per unit volume, T is the temperature and Φ is the dissipation function. In Cartesian coordinate system Φ becomes:

$$\Phi = \mu\left[2\left(\frac{\partial u}{\partial x}\right)^2 + 2\left(\frac{\partial v}{\partial y}\right)^2 + 2\left(\frac{\partial w}{\partial z}\right)^2 + \left(\frac{\partial v}{\partial x}+\frac{\partial u}{\partial y}\right)^2 + \left(\frac{\partial w}{\partial y}+\frac{\partial v}{\partial z}\right)^2 + \left(\frac{\partial u}{\partial z}+\frac{\partial w}{\partial x}\right)^2 - \frac{2}{3}\left(\frac{\partial u}{\partial x}+\frac{\partial v}{\partial y}+\frac{\partial w}{\partial z}\right)^2\right] \tag{2.4}$$

2.2 Turbulence Modeling

The standard $k-\varepsilon$ model, the realizable $k-\varepsilon$, the standard $k-\omega$ and the $\overline{v^2}-f$ model were compared for simulating different cases of film cooling for flat plates. The $k-\omega$ - sst model of Menter (1994), the $\overline{v^2}-f$ model of Durbin (1995), and new Transition-sst (4 eq.) model of Menter (2006), were compared for separated flow predictions on the highly loaded LPT airfoil. The unsteady Reynolds-averaged Navier-Stokes (URANS) equations were used as the transport equations for the mean flow. Large

Eddy Simulation (LES) with dynamic kinetic energy subgrid-scale model of Kim and Menon (1997) was utilized in the flow control study.

The governing equations and description of each model are presented in sections 2.2.1 – 2.2.7 below.

2.2.1 The standard $k-\varepsilon$ model (SKE)

The standard $k-\varepsilon$ model is based on Launder and Spalding (1974). In this model assumptions of the fully turbulent flow and negligible effects of molecular viscosity are used.

In this model the turbulence kinetic energy, *k*, and its rate of dissipation, *ε*, are obtained from the following transport equations:

$$\rho\frac{Dk}{Dt}=\frac{\partial}{\partial x_j}\left[\left(\mu+\frac{\mu_T}{\mathrm{Pr}_k}\right)\frac{\partial k}{\partial x_j}\right]+\left(2\mu_T S_{ij}-\frac{2}{3}\rho k\delta_{ij}\right)\frac{\partial u_i}{\partial x_j}-\rho\varepsilon \qquad (2.5)$$

and

$$\rho\frac{D\varepsilon}{Dt}=\frac{\partial}{\partial x_j}\left[\left(\mu+\frac{\mu_T}{\mathrm{Pr}_\varepsilon}\right)\frac{\partial \varepsilon}{\partial x_j}\right]+C_{\varepsilon 1}\frac{\varepsilon}{k}\left(2\mu_T S_{ij}-\frac{2}{3}\rho k\delta_{ij}\right)\frac{\partial u_i}{\partial x_j}-C_{\varepsilon 2}\rho\frac{\varepsilon^2}{k}, \qquad (2.6)$$

where S_{ij} is a mean strain vector, μ_T is a turbulent viscosity, $C_{1\varepsilon}$ and $C_{2\varepsilon}$ are constants, $\mathrm{Pr_k}$ and $\mathrm{Pr_\varepsilon}$ are the turbulent Prandtl numbers for *k* and *ε*, respectively, δ_{ij} is the Kronecker delta function (δ_{ij} = 1 if $i=j$ and δ_{ij} = 0 if $i \neq j$).

2.2.2 The standard $k-\omega$ model (SKW)

The standard $k-\omega$ model is a two equation model that solves for the transport of ω, the specific dissipation rate of the turbulent kinetic energy, instead of ε. It is based on the work of Wilcox (1998).

In this model the turbulence kinetic energy, k, and the specific dissipation rate, ω, are obtained from the following transport equations:

$$\rho\frac{\partial k}{\partial t}+\rho\frac{\partial u_i k}{\partial x_i} = \frac{\partial}{\partial x_j}\left[\Gamma_k\frac{\partial k}{\partial x_j}\right]+G_k-Y_k \tag{2.7}$$

and

$$\rho\frac{\partial \omega}{\partial t}+\rho\frac{\partial u_i \omega}{\partial x_i} = \frac{\partial}{\partial x_j}\left[\Gamma_\omega\frac{\partial \omega}{\partial x_j}\right]+G_\omega-Y_\omega \tag{2.8}$$

In these equations, G_k represents the generation of turbulence kinetic energy due to the mean velocity gradients. G_ω is the generation of ω. Γ_k and Γ_ω represent the effective diffusivity of k and ω, respectively. Y_k and Y_ω represent the dissipation of k and ω due to turbulence.

2.2.3 The realizable $k-\varepsilon$ model (RKE)

A new $k-\varepsilon$ eddy viscosity model, proposed by Shih et al., (1994) consists of a new model dissipation rate equation and a new realizable eddy viscosity formulation. The equation for the model dissipation rate is based on the dynamic equation of the mean-square vorticity fluctuation at large turbulent Reynolds number. In this model eddy viscosity formulation is based on the realizability constraints (under certain conditions (Shih et al., (1994)), normal Reynolds stresses may become negative, which is unphysical (unrealizable)).

The transport equation for k in this model is the same as in the standard $k-\varepsilon$ model (eq. 2.5), except for the model constants. The form of the ε equation is different and is as follows:

$$\rho\frac{\partial\varepsilon}{\partial t}+\rho\frac{\partial u_i\varepsilon}{\partial x_j} = \frac{\partial}{\partial x_j}\left[\left(\mu+\frac{\mu_t}{\mathrm{Pr}_\varepsilon}\right)\frac{\partial\varepsilon}{\partial x_j}\right]+\rho C_1 S_\varepsilon-\rho C_2\frac{\varepsilon^2}{k+\sqrt{\nu\varepsilon}} \tag{2.9}$$

where

$$C_1 = max\left[0.43,\frac{\eta}{\eta+5}\right],\quad \eta = S\frac{k}{\varepsilon},\quad S=\sqrt{2S_{ij}S_{ij}}$$

2.2.4 The shear-stress transport $k-\omega$ model (SKW-sst)

This model, developed by Menter (1994) is similar to the standard $k-\omega$ of Wilcox (1998), but has an ability to account for the transport of the principal shear stress in adverse pressure gradient boundary layers. The model is based on Bradshaw's (1967) assumption that the principal shear stress is proportional to the turbulent kinetic energy, which is introduced into the definition of the eddy-viscosity. These features make the Shear Stress Transport $k-\omega$ model (SKW-sst) more accurate and reliable for a wider class of flows (e.g., adverse pressure gradient flows, airfoils, transonic shock waves) than the standard $k-\omega$ model (ANSYS Fluent Documentation (2009)).

The SKW-sst model has a similar form of transport equations to the standard k - ω model:

$$\rho\frac{\partial k}{\partial t}+\rho\frac{\partial u_i k}{\partial x_i} = \frac{\partial}{\partial x_i}\left[\Gamma_k\frac{\partial k}{\partial x_j}\right]+\tilde{G}_k-Y_k \tag{2.10}$$

and

$$\rho\frac{\partial\omega}{\partial t}+\rho\frac{\partial u_i\omega}{\partial x_i} = \frac{\partial}{\partial x_i}\left[\Gamma_\omega\frac{\partial\omega}{\partial x_j}\right]+\tilde{G}_\omega-Y_\omega+D_\omega \tag{2.11}$$

In these equations $\tilde{G}_k$represents the generation of turbulence kinetic energy due to mean velocity gradients. $\tilde{G}_\omega$ represents the generation of ω. Γ_k and Γ_ω represent the effective diffusivity of k and ω respectively. Y_k and Y_ω represent the dissipation of k and

ω respectively due to turbulence. D_ω represents the cross-diffusion term. Details of SKW-sst model are given by Menter (1994) and will not be repeated here.

2.2.5 The v^2-f model (V2F)

According to Launder (1974), the normal stress $\overline{v^2}$, perpendicular to the local streamline plays the most important role to the eddy viscosity. Motivated by this idea, Durbin (1995) devised a “four-equation” model, known as the $k-\varepsilon-v^2$ model, or $\overline{v^2}-f$ model (V2F). It eliminates the need to patch models in order to predict wall phenomena like heat transfer or flow separation. It makes use of the standard $k-\varepsilon$ model, but extends it by incorporating the anisotropy of near-wall turbulence and non-local pressure strain effects, while retaining a linear eddy viscosity assumption.

The turbulence kinetic energy, k, its rate of dissipation, ε, the velocity variance scale, $\overline{v^2}$, and the elliptic relaxation function, f, are obtained from the following transport equations (Durbin (1995)):

$$\rho\frac{\partial k}{\partial t}+\rho\frac{\partial u_i k}{\partial x_i} = \frac{\partial}{\partial x_j}\left[\left(\mu+\frac{\mu_t}{\mathrm{Pr}_k}\right)\frac{\partial k}{\partial x_j}\right]+P-\rho\varepsilon \tag{2.12}$$

$$\rho\frac{\partial \rho}{\partial t}+\rho\frac{\partial u_i \varepsilon}{\partial x_i} = \frac{\partial}{\partial x_j}\left[\left(\mu+\frac{\mu_t}{\mathrm{Pr}_\varepsilon}\right)\frac{\partial \varepsilon}{\partial x_j}\right]+\frac{C'_{\varepsilon 1}P-C_{\varepsilon 2}\rho\varepsilon}{T} \tag{2.13}$$

$$\rho\frac{\partial \overline{v^2}}{\partial t}+\rho\frac{\partial u_i \overline{v^2}}{\partial x_i} = \frac{\partial}{\partial x_j}\left[\left(\mu+\frac{\mu_t}{\mathrm{Pr}_k}\right)\frac{\partial \overline{v^2}}{\partial x_j}\right]+\rho k f-6\rho\overline{v^2}\ \frac{\varepsilon}{k} \tag{2.14}$$

$$f-L^2\ \frac{\partial^2 f}{\partial x_j^2}=(C_1-1)\frac{\frac{2}{3}-\frac{\overline{v^2}}{k}}{T}+C_2\frac{P}{\rho k}+\frac{5\frac{\overline{v^2}}{k}}{T} \tag{2.15}$$

where

$$P \;=\; 2\mu_t S^2, S^2 \;\equiv\; \mathrm{S}_{ij}\mathrm{S}_{ij}\,, \mathrm{S}_{ij} = {}^1\!/_2\left(\frac{\partial u_i}{\partial x_j} + \frac{\partial u_j}{\partial x_i}\right) \tag{2.16}$$

The turbulent time scale T and length scale L are defined by

$$T' = max\left[\frac{k}{\varepsilon}, 6\sqrt{\frac{\nu}{\varepsilon}}\right] \tag{2.17}$$

$$T = min\left[T', \frac{\alpha}{\sqrt{3}}\frac{k^{3/2}}{\overline{v^2}\,\mathrm{C}_\mu\,\sqrt{2\mathrm{S}^2}}\right] \tag{2.18}$$

$$L' = min\left[\frac{k^{3/2}}{\varepsilon}, \frac{1}{\sqrt{3}}\frac{k^{3/2}}{\overline{v^2}\,\mathrm{C}_\mu\,\sqrt{2\mathrm{S}^2}}\right] \tag{2.19}$$

$$L = C_L max\left[L', C_\eta\left(\frac{\nu^3}{\varepsilon}\right)^{1/4}\right] \tag{2.20}$$

In the above equations, α, C_1, C_2, $C'_{\varepsilon 1}$, $C_{\varepsilon 2}$, C_η, C_μ, and C_L are constants. $\mathrm{Pr_k}$ and Pr_ε are the turbulent Prandtl numbers for k and ε, respectively and ν is the kinematic viscosity (μ/ρ).

2.2.6 The Transition-sst (4 equations) model (Trans-sst)

A new correlation-based transition model (Trans-sst) was proposed by Menter et al., (2006). This model is based on two transport equations. The intermittency transport equation is used to trigger the transition onset. The transport equation for the transition momentum thickness Reynolds number ($Re_{\theta t}$) is used to capture non-local effects of freestream turbulence intensity and pressure gradient at the boundary layer edge. Outside the boundary layer the transport variable was forced to follow the value of $Re_{\theta t}$ given by correlations. Those two equations were coupled with the shear stress transport turbulence model (SST). This model was implemented in the version 12 of ANSYS Fluent code.

The transport equation for the intermittency γ is defined in Menter et al., (2006) as:

$$\frac{\partial}{\partial t}(\rho\gamma) + \frac{\partial}{\partial x_j}\left(\rho U_j \gamma\right) = P_{\gamma 1} - E_{\gamma 1} + P_{\ \gamma 2} - E_{\gamma 2} + \frac{\partial}{\partial x_j}\left[\left(\mu + \frac{\mu_t}{\mathrm{Pr}_\gamma}\right)\frac{\partial \gamma}{\partial x_j}\right] \tag{2.21}$$

The transition sources are defined as follows:

$$P_{\gamma 1} = 2F_{length}\rho S[\gamma F_{onset}]^{\ c_{\gamma 3}}, \qquad E_{\gamma 1} = P_{\gamma 1}\gamma \tag{2.22}$$

where S is the strain rate magnitude. F_{length} is an empirical correlation that controls the length of the transition region. The destruction/relaminarization sources are defined as follows:

$$P_{\gamma 2} = \left(2c_{\gamma 1}\right)\rho\Omega\gamma F_{turb}, \qquad E_{\gamma 2} = c_{\gamma 2}P_{\gamma 2}\gamma, \tag{2.23}$$

where Ω is the vorticity magnitude. The transition onset is controlled by the following functions:

$$F_{onset1} = \frac{Re_v}{2.193Re_{\theta c}},$$

$$F_{onset2} = min(max(F_{onset1}, {F^4}_{onset1}), 2.0), \tag{2.24}$$

$$F_{onset3} = max\left(1 - \left(\frac{R_T}{2.5}\right)^3, 0\right),$$

$$F_{onset} = max(F_{onset2} - F_{onset3}, 0),$$

$$F_{turb} = e^{-\left(\frac{R_T}{4}\right)^4}, \tag{2.25}$$

where

$$Re_V = \frac{\rho y^2 S}{\mu},$$

$$Re_T = \frac{\rho k}{\mu\omega} \tag{2.26}$$

$Re_{\theta c}$ is the critical Reynolds number where the intermittency first starts to increase in the boundary layer. This occurs upstream of the transition Reynolds number $\widetilde{Re_{\theta t}}$ and the difference between the two must be obtained from an empirical correlation. Both F_{length} and $Re_{\theta c}$ correlations are functions of $\widetilde{Re_{\theta t}}$.

The constants for the intermittency equation are:

$$c_{\gamma 1} = 0.03;\ c_{\gamma 2} = 50;\ c_{\gamma 3} = 0.5;\ \sigma_{\gamma} = 1.0.$$

The transport equation for the transition momentum thickness Reynolds number $\widetilde{Re_{\theta t}}$ in Menter et al. (2006) is:

$$\frac{\partial}{\partial t}\left(\rho \widetilde{Re_{\theta t}}\right) + \frac{\partial}{\partial x_j}\left(\rho U_j \widetilde{Re_{\theta t}}\right) = P_{\theta t} + \frac{\partial}{\partial x_j}\left[\sigma_{\theta t}(\mu + \mu_t)\frac{\partial \widetilde{Re_{\theta t}}}{\partial x_j}\right] \tag{2.27}$$

The source term is defined as follows:

$$P_{\theta t} = c_{\theta t}\frac{\rho}{t}\left(Re_{\theta t} - \widetilde{Re_{\theta t}}\right)(1.0 - F_{\theta t}),$$

$$t = \frac{500\mu}{\rho U^2} \tag{2.28}$$

$$F_{\theta t} = min\left(max\left(F_{wake} e^{\left(-\frac{y}{\delta}\right)^4}, 1.0 - \left(\frac{\gamma - \frac{1}{50}}{1.0 - \frac{1}{50}}\right)^2\right), 1.0\right) \tag{2.29}$$

$$\theta_{BL} = \frac{\mu \widetilde{Re_{\theta t}}}{\rho U}$$

$$\delta_{BL} = \frac{15}{2}\theta_{BL}$$

$$\delta = \frac{50\Omega y}{U}\delta_{BL} \tag{2.30}$$

$$Re_{\omega} = \frac{\rho \omega y^2}{\mu}$$

$$F_{wake} = e^{-\left(\frac{Re_{\omega}}{1E+5}\right)^{2}} \qquad (2.31)$$

The model constants for the $\widetilde{Re_{\theta t}}$ equation are: $c_{\theta t} = 0.03, \sigma_{\theta t} = 2.0$

The Transition-sst model in ANSYS Fluent 12 contains empirical correlations for the transition onset, length of the transition zone and the point where model is activated to match both of them. These correlations are proprietary.

The Transition-sst model interacts with the SKW-sst turbulence model through modification of original production and destruction terms in the transport equation of k according to changes in effective intermittency. The production term in the ω-equation is not modified.

Additional details of this model are given in Menter et al., (2006).

2.2.7 Large Eddy Simulation (LES)

In LES, large eddies are resolved directly, while small eddies are modeled. The rationale behind LES are as follows: a) momentum, mass, energy, and other passive scalars are transported mostly by large eddies; b) large eddies are dictated by the geometries and boundary conditions of the flow involved; c) small eddies are more isotropic, and are consequently more universal, and d) the chance of finding a universal turbulence model is much higher for small eddies (ANSYS Fluent Documentation (2009)).

The governing equations employed for LES are obtained by filtering the time-dependent Navier-Stokes equations. The filtering process effectively filters out the eddies whose scales are smaller than the filter width or grid spacing used in the computations. The resulting equations thus govern the dynamics of large eddies.

Following Leonard (1974), flow variables in LES are decomposed into large and subgrid (filtered) scales as follows:

$$\phi(\mathbf{x}) = \bar{\phi}(\mathbf{x}) + \phi'(\mathbf{x}) \tag{2.32}$$

A filtered variable (denoted by an overbar) is defined by:

$$\bar{\phi}(\mathbf{x}) = \int_{\mathcal{D}} \phi(\mathbf{x}')\, \mathrm{G}(\mathbf{x}, \mathbf{x}') d\mathbf{x} \tag{2.33}$$

where $\mathcal{D}$ is the fluid domain, and G is the filter function that determines the scale of the resolved eddies.

In ANSYS Fluent, the finite-volume discretization itself implicitly provides the filtering operation:

$$\bar{\phi}(\mathbf{x}) = \frac{1}{\mathrm{V}} \int_{\mathrm{V}} \phi(\mathbf{x}')\, d\mathbf{x}',\ \mathbf{x}' \in \mathrm{V} \tag{2.34}$$

where V is the volume of computational cell. The filter function, $\mathrm{G}(\mathbf{x}, \mathbf{x}')$, implied here is then:

$$\mathrm{G}(\mathbf{x}, \mathbf{x}') = \begin{cases} \frac{1}{\mathrm{V}}, & \mathbf{x}' \in \mathrm{V} \\ 0, & \mathbf{x}' \text{ otherwise} \end{cases} \tag{2.35}$$

Navier-Stokes equations after filtering:

$$\frac{\partial \bar{u}_i}{\partial x_i} = 0 \tag{2.36}$$

and

$$\frac{\partial \bar{u}_i}{\partial t} + \frac{\partial \bar{u}_i \bar{u}_j}{\partial x_j} = \nu \frac{\partial^2 \bar{u}_i}{\partial x_k \partial x_k} - \frac{\partial \bar{p}}{\partial x_i} - \frac{\partial \tau_{ij}}{\partial x_j}, \tag{2.37}$$

where and τ_{ij} is the subgrid –scale stress defined by

$$\tau_{ij} \equiv \left(\overline{\bar{u}_i \bar{u}_j} - \bar{u}_i \bar{u}_j\right) + \left(\overline{u'_i \bar{u}_j} + \overline{\bar{u}_i u'_j}\right) + \overline{\left(u'_i u'_j\right)} \tag{2.38}$$

The subgrid-scale stresses resulting from the filtering operation are unknown, and require modeling. The subgrid-scale turbulence models in ANSYS Fluent employ the Boussinesq hypothesis as in the RANS models, computing subgrid-scale turbulent stresses from:

$$\tau_{ij} - \frac{1}{3}\tau_{kk}\delta_{ij} = -2\mu_t\bar{S}_{ij}$$

where μ_t is the subgrid-scale turbulent viscosity. The isotropic part of the subgrid-scale stresses τ_{kk} is not modeled, but added to the filtered static pressure term. $\bar{S}_{ij}$ is the rate-of-strain tensor for the resolved scale defined by:

$$\bar{S}_{ij} \equiv \frac{1}{2}\left(\frac{\partial \bar{u}_i}{\partial x_j} + \frac{\partial \bar{u}_j}{\partial x_i}\right)$$

The subgrid-scale model used in the present study with LES is dynamic kinetic energy model proposed by Kim and Menon (1997). In this model a separate transport equation is solved for subgrid-scale kinetic energy. The model constants are determined dynamically. The details of the implementation of this model in Fluent and it's validation are given by Kim (2004).

Greater details on the turbulence model's constants are published elsewhere and will not be discussed here, since none of the turbulence models was modified in the present work.

CHAPTER III

PART 1: PULSED JETS FILM COOLING

3.1 Literature Review

Much research has been done in film cooling in order to achieve better cooling of gas turbine blades and thus increase performance of turbine engines by allowing higher inlet temperatures. However, there are very few studies published, which consider effect of jet pulsation on the film cooling characteristics.

Ekkad et al., (2006) experimentally investigated the effect of jet pulsation and duty cycle on film cooling from a single jet located on the circular leading edge of a blunt body. Film cooling characteristics were examined for duty cycles from 0.1 to 1, at nominal pulse blowing ratios from 0.5 to 2 and pulse frequencies of 5 Hz and 10 Hz. This study reported that higher film cooling effectiveness was obtained at the reduced blowing ratios and the effect of varying the pulsing frequency was negligible. The conclusion of this work was that pulsed jets resulted in relatively better film cooling effectiveness compared to continuously blown jets.

Coulthard et al. (2006) conducted an experimental study of a row of film cooling jets in cross flow on a flat plate. Jets were inclined 35 deg to the surface in streamwise direction. Various blowing ratios (B) (from 0.25 to 1.5), duty cycles (DC) (from 0.25 to

0.75) and Strouhal numbers (St) (from 0.0119 to 0.1905) were considered. The authors reported that the highest film cooling effectiveness was achieved at blowing ratio 0.5 with steady blowing. With increasing blowing ratio, effectiveness decreased due to jet lift-off. In their work the authors observed that higher pulsation frequencies resulted in lower effectiveness with the exception of the highest frequency tested, where the trend was reversed. Overall conclusion was that pulsing does not provide benefits to the film cooling applications for the studied geometry and flow characteristics. Comparing the results of the two experiments (Ekkad et al., (2006) and Coulthard et al. (2006)) is rather difficult since the two cases had different geometry (both jet and plenum), and free stream pressure gradient among others.

Muldoon and Acharya (2007) were the first to conduct a computational Direct Numerical Simulation (DNS) study of pulsed jet film cooling. The geometry in their work consisted of a cylindrical jet, inclined at 35 deg in the streamwise direction, in a crossflow. Jets were pulsed with various duty cycles (from 0.25 to 1), blowing ratios (from 0.375 to 1.5) and Strouhal numbers (0.08 and 0.32). The coolant delivery tube was modeled in base-line DNS calculations in order to obtain jet-exit conditions. A conclusion of their study was that pulsing, with higher frequency, DC = 50% and peak B = 1.5, helped to improve film cooling effectiveness (due to reduced jet lift-off) compared to the steady B = 1.5 case.

There was no study found in open literature, which considers jet pulsation effect on shaped film hole design performance.

Results on pulsed jets effect on the film cooling, found in the literature, are mixed. Comprehensive pulsed jets film cooling study is needed in order to answer the question: when and where jet's pulsation can help to improve film cooling, while reducing the coolant flow rate?

3.2 Computational model and boundary conditions

Fourteen different cases were simulated in this study, ten cases for CFH (cylindrical film hole) geometry of Coulthard et al., (2006) and four cases for LDIFF (film hole with laterally diffused exit) geometry of Hyams and Leylek (2000). Details of all cases are presented in Table 3.1.

Table 3.1: Pulsed jet cases simulated

Geometry	**CFH**		**LDIFF**
Blowing ratio	*B = 0.5*	*B = 1.5*	*B = 1.25*
Turbulence model	*SKE, SKW, RKE, V2F*	*RKE*	*SKE*
Strouhal number	Steady State, St = 0.0119, 0.19, 0.38 and 1		Steady State, St = 0.0119, 0.19 and 0.38
Density ratio	1.0		1.6

Due to high flow unsteadiness even for steady blowing, unsteady calculations were performed. For pulsed and steady cases convergence was established when: 1) residuals reduced to a value 10^{-5} except for energy residual for which convergence criterion was set to 10^{-8}, 2) no change was observed in any field results for steady cases and cycle-to-cycle convergence was achieved for pulsed cases, 3) the mass and energy imbalance was less than 0.01 %.

Approximately 800 time steps with time step size = 0.01 s were necessary to reach a fully converged state for steady blowing cases. For the pulsed cases 10-15 cycles were needed to achieve cycle-to-cycle convergence with 20 time steps per cycle, 20-50 iterations per time step. Time step size was adjusted with pulse frequency with the same number of time steps per cycle.

3.2.1 Cylindrical film hole geometry

The CFH geometry matches the experiment of Coulthard et al., (2006). The schematic of the experimental test setup is presented in Fig. 3.1. The extent of the computational domain, which is used in the present work, is shown by the dashed lines. It is 0.8D upstream, 18D downstream of the jet Leading Edge (LE) and 5.25D above the test surface. Jets are inclined at 35 deg angle in a streamwise direction and spaced 3D apart center to center. Film hole length to diameter ratio L/D=4. The origin of the Cartesian coordinate system is placed at the Trailing Edge (TE) of the film hole on the top surface of the test plate and its x, y and z axes aligned with the streamwise, vertical and lateral directions. Computational domain includes the whole supply plenum because the flow in the film hole is complex and highly depends on the plenum geometry (Walters and Leylek (1997, 2000)). Incompressible fluid flow was considered.

Experimental velocity profile of Coulthard et al., (2006) was applied at x/D=0.8 upstream of the film hole LE in combination with the profiles for turbulence kinetic energy and turbulence dissipation rate, it represents fully turbulent boundary layer at this location. Symmetry boundary conditions were modeled at z/D = 1.5 and -1.5 from the jet centerline. Symmetry rather than periodic boundary conditions were used because: 1) the results from Coulthard et al., (2006) showed symmetry, 2) most of the CFD data is presented for time-averaged quantities where the differences between the two boundary conditions (symmetry and periodic) are negligible. Symmetry was also applied at the top of the computational domain. Temperature of the crossflow air was set to 293 K.

Crossflow inlet parameters were maintained the same for all cases. Inlet plenum geometry of Coulthard et al. (2006) was used with coolant injection through round holes (D = 0.019 m) at the bottom of the plenum. The plenum inlet velocity was modified in order to change the blowing ratio. The coolant temperature of 300 K, used in calculations, corresponds to a density ratio of 1. Reynolds number, based on freestream velocity and film hole diameter is 10,400. All the walls were defined as no-slip and adiabatic. In pulsed cases the blowing ratio was calculated as an average blowing ratio during the open-jet period. At the outlet a constant pressure boundary condition were applied with zero gauge pressure.

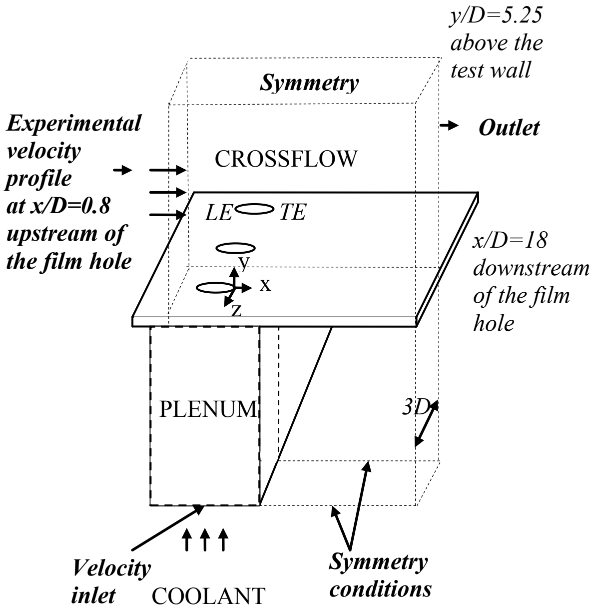

Figure 3.1: A schematic of the experimental test setup for Coulthard et al., (2006) CFH geometry, including extent of the computational domain (dashed lines) and boundary conditions.

Computations were performed using version 6.3.26 of the finite-volume code ANSYS Fluent. GAMBIT 2.3.16 software by ANSYS was used to generate computational grid.

3.2.2 Film hole with laterally diffused exit

The geometry, chosen for this study, matches the one of Hyams and Leylek (2000). The row of the film cooling jets inclined at 35 deg to the crossflow was investigated. Fig. 3.2 shows the film hole geometry, proposed by Hyams and Leylek, which consists of cylindrical film hole, diffused in the lateral direction by 12 deg angle, starting at 2.1 D length from the entrance to the jet, D = 0.0111 m. Film hole length-to-diameter ratio is 4D. The extent of the computational domain is 25D in a streamwise direction, 10D above the test wall and 1.5D in a lateral direction. The origin of the Cartesian coordinate system is placed at the Trailing Edge (TE) of the film hole on the top surface of the test wall. The computational setup and the extent of the computational domain were modeled the same as in Hyams and Leylek (2000) in order to compare results for steady blowing conditions. For this geometry incompressible fluid flow was considered as well.

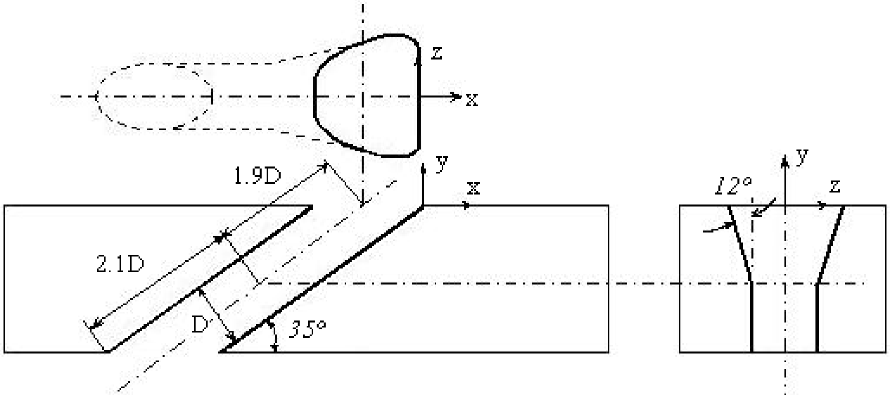

Figure 3.2: A schematic of the LDIFF film hole shape of Hyams and Leylek (2000)

Plenum with dimensions 6D width, 2D height and 1.5D in spanwise direction was included in the calculation. Uniform velocity of 0.541 m/s was set at the plenum inlet in order to match Re_{fh} = 18,700 for B = 1.25. A turbulence intensity of 0.1% was applied at the plenum inlet and 1% at the crossflow inlet, the length scale was taken to be one-tenth of the inlet extent in both cases. Following Hyams and Leylek the crossflow inlet temperature was set at 300 K and the coolant temperature - at 187.5 K, which creates a density ratio of 1.6. The blowing ratio for the pulsed cases was defined as an average blowing ratio during the open-jet period. The SKE turbulence model was used for solving Reynolds Averaged Navier-Stokes (RANS) equations. Enhanced wall treatment (when the SKE model is employed in the fully turbulent region and the one-equation model of Wolfstein is used in the viscosity-affected near-wall region, (2005)) was applied for the computation domain, which requires the first grid cell to be located at the dimensionless wall distance (y^+) of 1. All equations were discretized up to the second order. It should be noted that there were no experimental data for the LDIFF geometry with pulsed jet found in the open literature. Therefore, obtained CFD results were compared with earlier CFD ones (Hyams and Leylek (2000)) which were obtained at B=1.25. The present work was extended to the pulsed jet with St = 0.0119, 0.19 and 0.38. Furthermore the same turbulence model (SKE) used by Hyams and Leylek was also applied for the LDIFF geometry.

3.3 Results and discussion

3.3.1 Code validation

In this section the results obtained with different turbulence models are presented in order to validate the CFD model used to study pulsed jets film cooling physics. Figure 3.3 shows results for centerline film cooling effectiveness for the CFH geometry plotted versus x/D. Results were compared with the experimental data from Coulthard et al., (2006). Four different turbulence models were tested: V2F, RKE, SKW, and SKE. The inlet velocity profile used for the cross flow was obtained from the measured one (Coulthard et al., (2006)) at x/D = 0.8 upstream of the jet. The SKE and RKE models show the best overall performance.

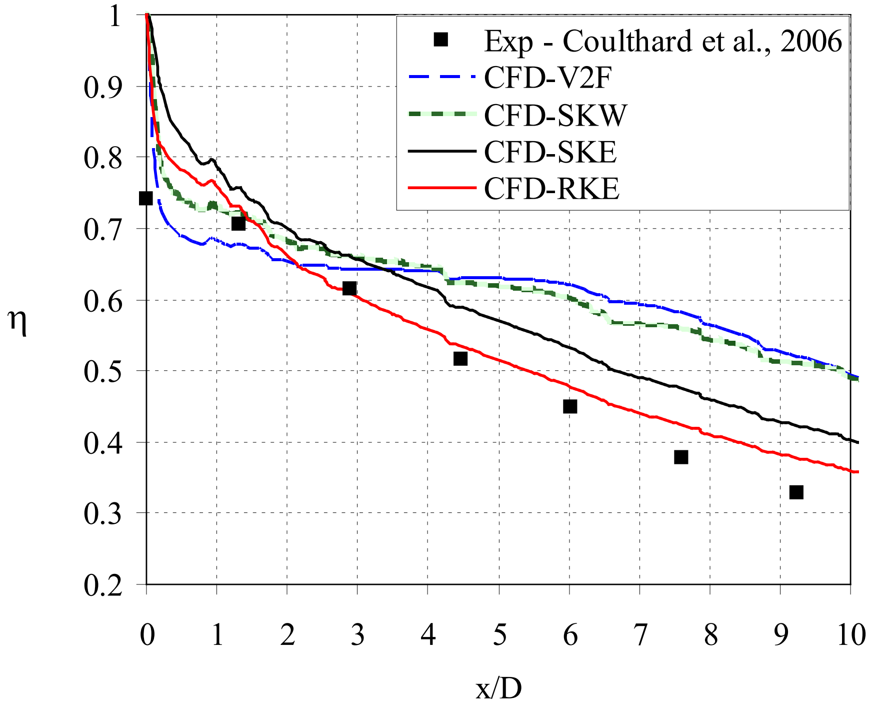

Figure 3.3: Centerline plot of adiabatic film cooling effectiveness with different turbulence models, compared to experimental data (CFH geometry, B=0.5, steady blowing)

The SKW and V2F models are in a better agreement with the experimental data downstream of the jet-exit up to x/D = 1.5 than the SKE and RKE models. Downstream of x/D = 1.5 SKW and V2F models significantly overpredict the film cooling effectiveness compared to the SKE and RKE models. Based on this results the RKE turbulence model was selected for further investigation for CFH geometry. Another reason for choosing RKE is that it resolves the problem which appears in the SKE turbulence model - when, under certain conditions (Shih et al., (1994)), normal Reynolds stresses may become negative, which is unphysical (unrealizable).

For the purpose of code validation present CFD results from RKE model are compared against other CFD and experimental data on Fig. 3.4. Figure 3.4 shows the centerline film cooling effectiveness plotted versus x/D, B = 0.5 from different CFD and experimental studies. The following was observed: a) the variations in the film cooling effectiveness among different experimental studies (Sinha et al., (1991), Mayhew (1999) and Coulthard et al., (2006)) are due to the differences in density ratio, injection-pipe length/diameter ratio, pitch-to-diameter ratio, cross flow inlet profile, and plenum geometry, b) the CFD data from the present work (RKE turbulence model) is in a reasonable agreement with the experimental data from Coulthard et al., (2006). This is due to the fact that in this study the experimental setup (geometry, inlet flow conditions, etc.) was matched and the chosen RKE turbulence model performed well, c) The other CFD data, from Walters, Leylek (2000), shows the sensitivity of the CFD results to the geometry used as well as the turbulence model applied.

The effect of changing the blowing ratio (B) from 0.5 to 1.5 under steady state conditions was also examined in the present work. Coolant flow at the jet-exit is highly complex and depends on the blowing ratio. For B = 0.5 and CFH geometry, 61 % of the mass flow were coming through the downstream half of jet exit plane. On the other hand, for B = 1.5, with the same geometry, about 49 % of the mass flow were coming through the downstream half of the jet exit plane. The reasons behind that are the decrease in the effect of the cross flow on the jet as coolant velocity increases and jet “lift-off” in the case of high blowing ratio. These data are consistent with the results of Andreopoulos and Rodi (1984).

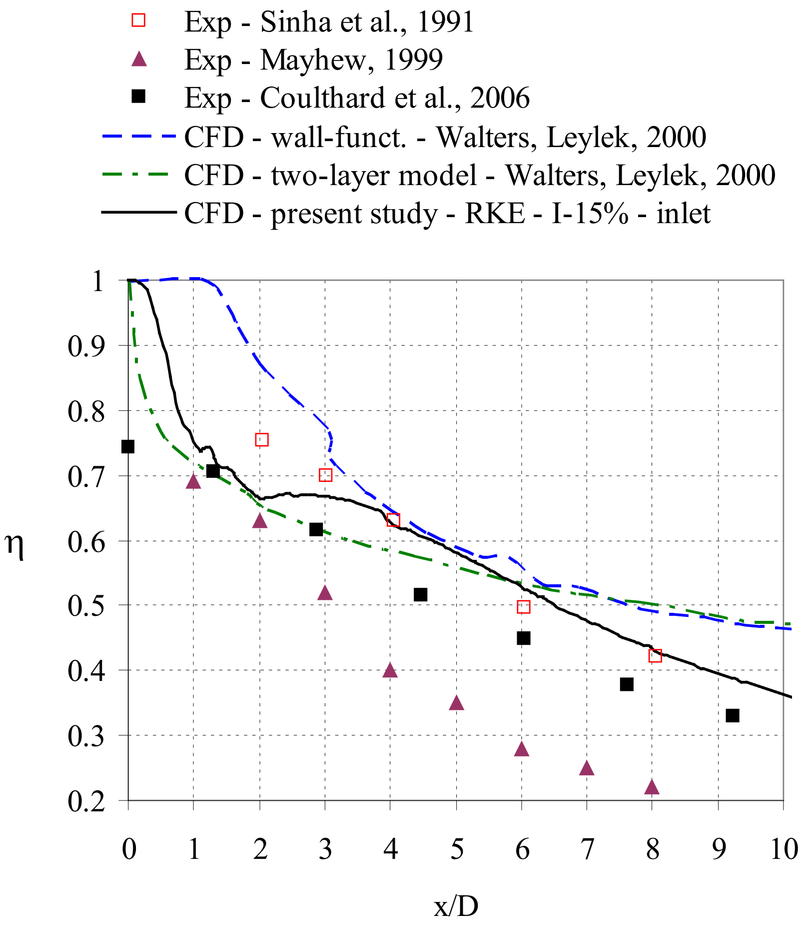

Figure 3.4: Centerline adiabatic film cooling effectiveness, B - 0.5, data from various experimental and computational studies compared to present work. (CFH geometry)

Figure 3.5 shows comparison of the present CFD results (for centerline effectiveness) from the RKE model with DNS data from Muldoon and Acharya (2007) and the experimental data of Coulthard et al., (2006), for steady state, B=1.5 case. Present CFD model agrees very well with the experiment for x/D > 2. The DNS data agrees better with the experimental data for x/D < 2. This is because the complicated turbulent structures downstream of the jet exit are directly resolved in DNS

For the code validation purposes current pulsed jet CFD results for the centerline film cooling effectiveness are compared with experimental data of Coulthard et al., (2006) on Figure 3.6. Lines represent CFD results. Solid line is for St = 0.0119, and dashed line is for St = 0.19. Experimental results are represented by filled symbols. Square symbol is for St = 0.0119, and round symbol is for St = 0.19

The CFD model shows overall good agreement with the data. As can be seen from this section, the present CFD code with RKE turbulence model was validated by comparing its results with experimental results and CFD data of other researchers, including DNS, for both steady film cooling flow and unsteady pulsed jets. This provided a confidence in this model such that it can be used to examine how the pulsed jet performance is affected by varying: 1) pulsation frequency, 2) blowing ratio and 3) jet geometry. Each parameter will be discussed separately in the following sections. Section 3.3.2 is devoted to the effect of pulsation frequency. Effect of blowing ratio is discussed in section 3.3.3. In section 3.3.4 effect of jet geometry is investigated. Spatially averaged film cooling effectiveness is used in section 3.3.5 for the purpose of comparison among all cases studied.

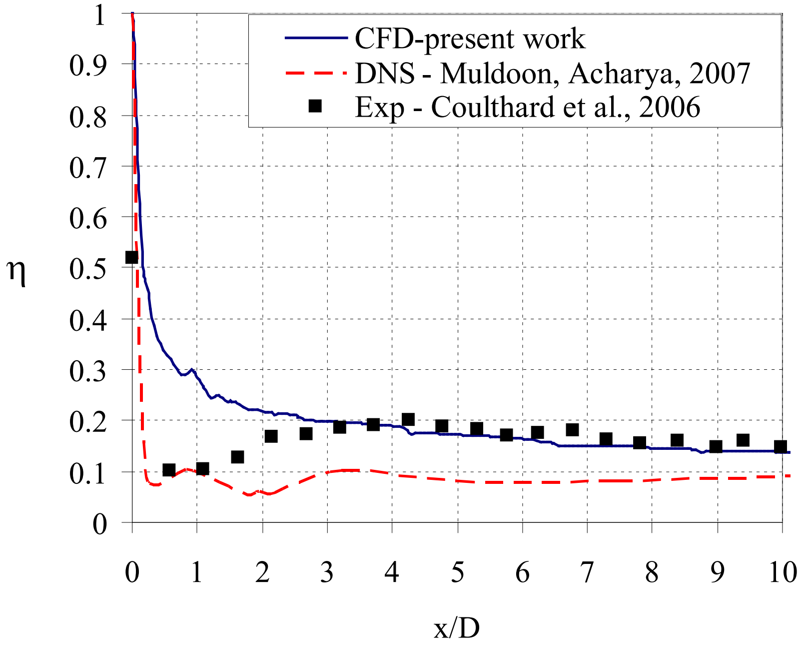

Figure 3.5: Centerline adiabatic film cooling effectiveness, steady state, B = 1.5 compared to DNS and experimental data (CFH geometry)

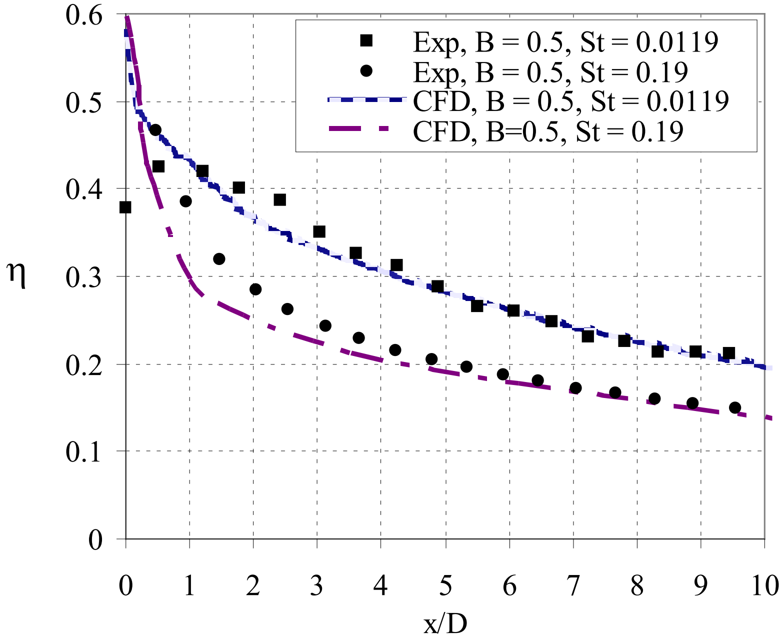

Figure 3.6: Centerline plot of time averaged adiabatic film cooling effectiveness for B = 0.5, St=0.0119 and St=0.19, compared to experimental results (CFH geometry)

3.3.2 Effect of Pulsation Frequency

The effect of pulsation frequency was examined for the CFH geometry at St=0.0119, 0.19, 0.38 and 1.0, and for LDIFF geometry (will be discussed later in section 3.3.4) geometry at St=0.0119, 0.19, and 0.38.

Figure 3.7a shows the centerline (time averaged) film cooling effectiveness for the CFH geometry with B =0.5, steady state, St=0.0119, 0.19, 0.38 and 1.0. The centerline film cooling effectiveness, plotted versus x/D, showed that the effectiveness in the case of pulsation was always below the steady state one. However, the effect of frequency varied according to the downstream location from the jet exit. Immediately near the jet trailing edge the effectiveness increased as the frequency increased. Downstream from x/D = 3 location the values of effectiveness for both St=0.0119 and 0.38 are close to each other, while lower effectiveness values are observed for St= 0.19. For St=1.0 the effectiveness is the closest to the one from the steady blowing case for all x/D values compared to the other St.

Figure 3.7b shows the spanwise averaged film cooling effectiveness plotted versus x/D for the CFH geometry with B =0.5, steady state, St = 0.0119, 0.19, 0.38 and 1.0. Similar results are obtained to those discussed in Figure 3.7a except the magnitude of variations is much smaller.

In order to examine these results further effectiveness footprints on the downstream wall are plotted for B = 0.5 in Figure 3.8. Figure 3.8a shows results from the steady blowing case, 3.8b - from the St = 0.0119 case, 3.8c – from the St = 0.19case and 3.8d – from the St = 0.38 case.

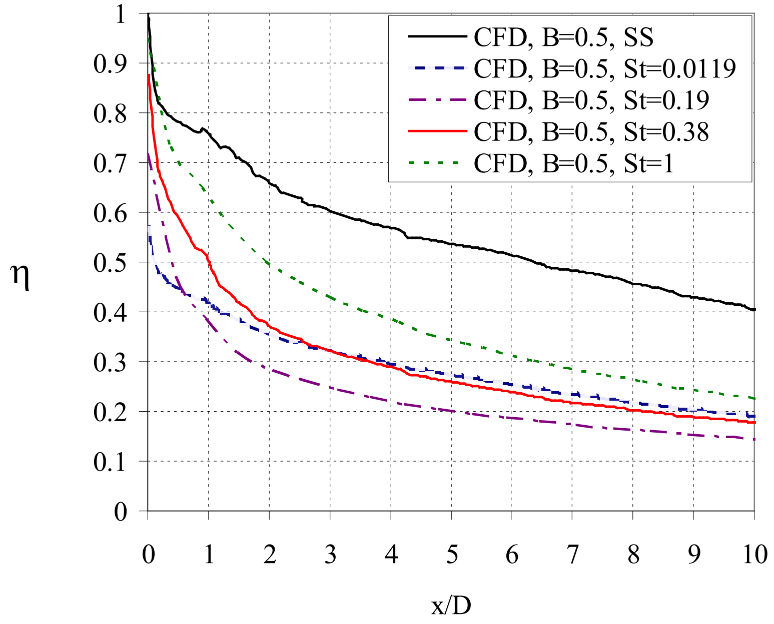

a)

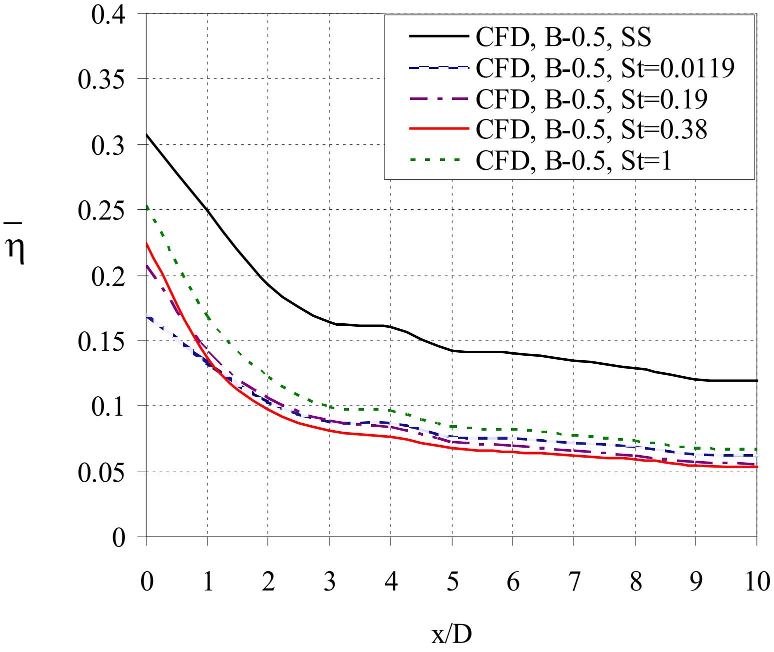

b)

Figure 3.7: Centerline-(a) and spanwise averaged-(b) plot of adiabatic film cooling effectiveness for B = 0.5 steady state and different Strouhal numbers

The footprints on Fig. 3.8 are shown at different times in the cycle with duty cycle of 50%. Time t/T=0 corresponds to the beginning of blowing, t/T = ¼ - to the middle of blowing, t/T = ½ - to the end of blowing and t/T = ¾ -to the middle of no blowing.

Figure 3.8a shows the steady state results with high effectiveness downstream of the jet. Figure 3.8b shows the results of St= 0.0119 case where we see high effectives, similar to the steady state one, only on a small window of the cycle (near t/T = 1/4 and t/T=1/2 - only downstream of the jet) indicating a quasi-steady behavior, otherwise (i.e. at other times of the cycle) the jet film cooling effectiveness is very poor. As the frequency increased (Figure 3.8c) the footprints of the film cooling effectiveness took a more complicated shape showing considerable variation in the span-wise direction at different times of the cycle with a net effect of lower effectiveness throughout the cycle and the lowest (time averaged values) at St = 0.19 (as shown earlier in Figure 3.7a). Figures 3.8d is for the higher frequency (St=0.38) and shows a quasi-steady behavior. The film cooling effectiveness in St = 0.38 case has almost a constant value throughout the cycle. This, of course, results in a higher time averaged film cooling effectiveness as shown earlier but the values are still below the values from the steady blowing case. Similar observations were noted for St = 1.0 (effectiveness footprints are not shown) to what discussed at St = 0.38.

In order to understand the behavior described above, movies were generated for the side views of temperature contours (corresponds directly to the film cooling effectiveness for an adiabatic wall) and of the velocity magnitude contours and vectors for different Strouhal numbers. Frames were than extracted from the movies at four different times in the cycle: beginning of blowing (t/T=0); middle of blowing (t/T = ¼) end of blowing (t/T = ½) and middle of no blowing (t/T = ¾).This was done for the CFH geometry for the following cases: B = 0.5 (St=0.0119, St=0.19 and St=0.38) and B = 1.5 (St=0.0119, St=0.38 and St=1). Side views of temperature contours and of the velocity magnitude contours and vectors are also shown for the CFH geometry for steady blowing and “no jet flow” cases with B = 0.5 and B = 1.5 for the reference. These results are discussed in this section and section 3.3.3.

Figure 3.9a shows velocity contours and vectors for the steady blowing B=0.5 case for CFH geometry. It can be seen that because of the plenum geometry a non-uniform flow entered the injection pipe with a recirculation near the forward bottom side of the pipe. This, in turn, resulted in highly non-uniform flow at the jet outlet (maximum local velocity is 5 m/s, which is 25 % higher than the nominal blowing velocity for the B=0.5 case).

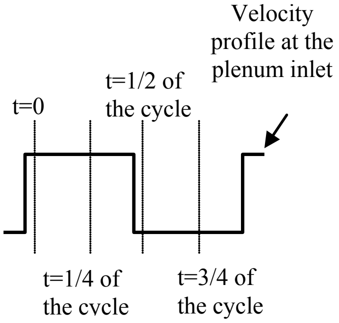

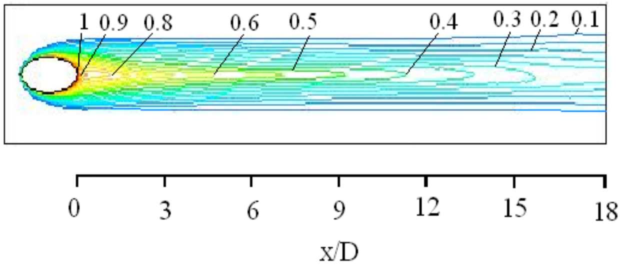

Figure 3.8a: Effectiveness footprints on the test wall downstream of the film hole, B = 0.5, steady blowing, (CFH geometry)

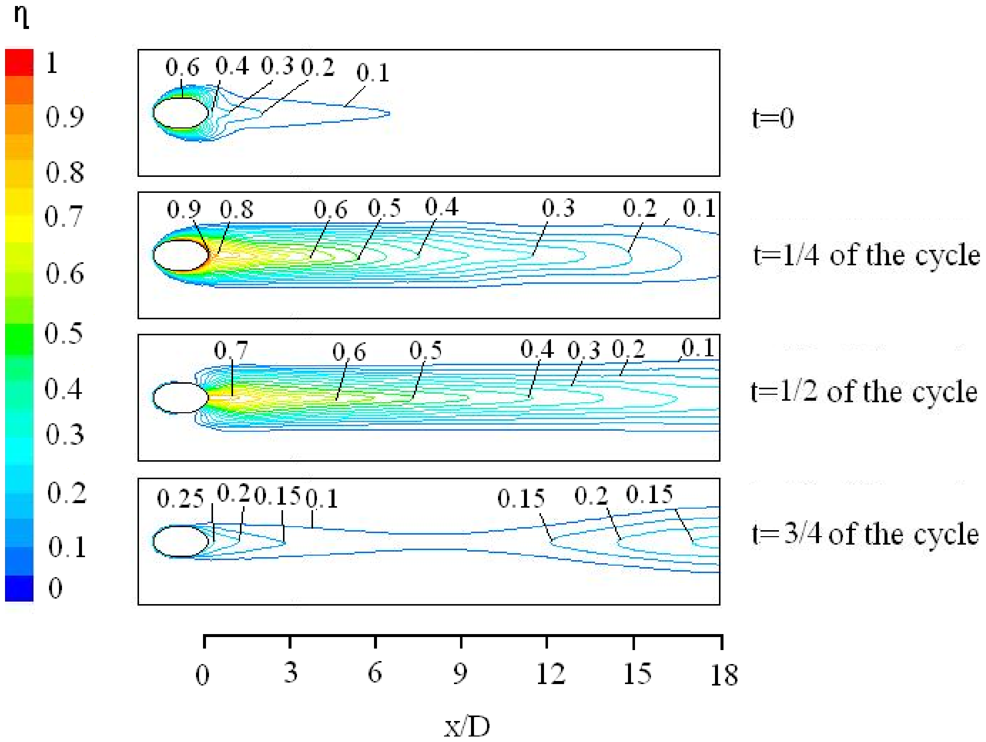

Figure 3.8b: Effectiveness footprints on the test wall downstream of the film hole, B = 0.5, steady blowing, St = 0.0119, (CFH geometry)

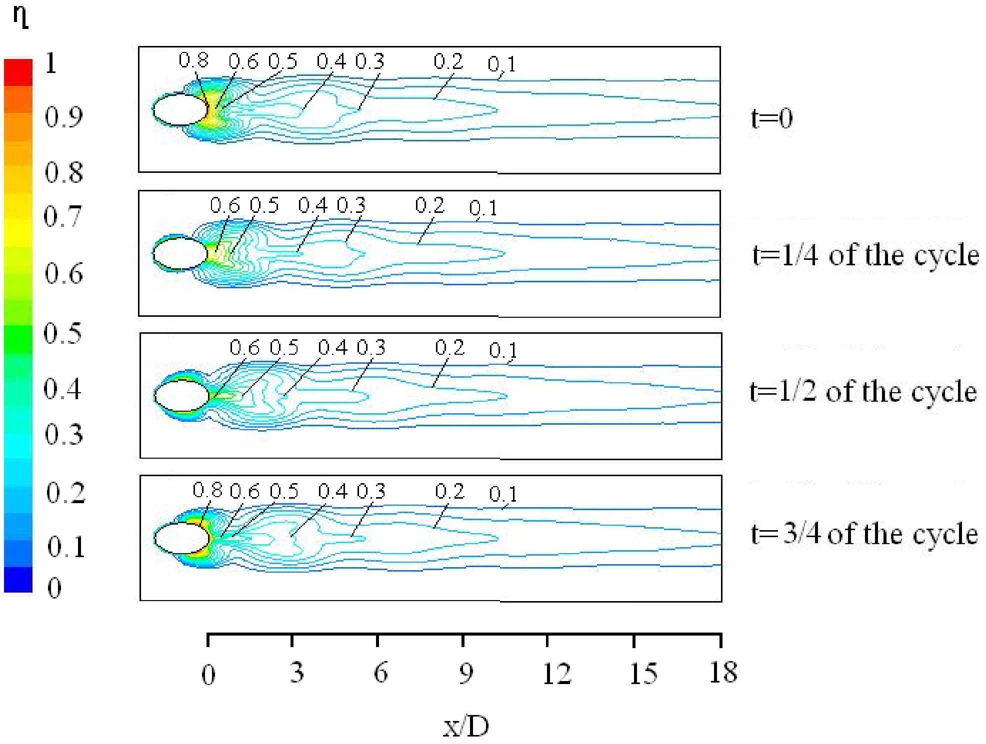

Figure 3.8c: Effectiveness footprints on the test wall downstream of the film hole, B = 0.5, steady blowing, St = 0.19, (CFH geometry)

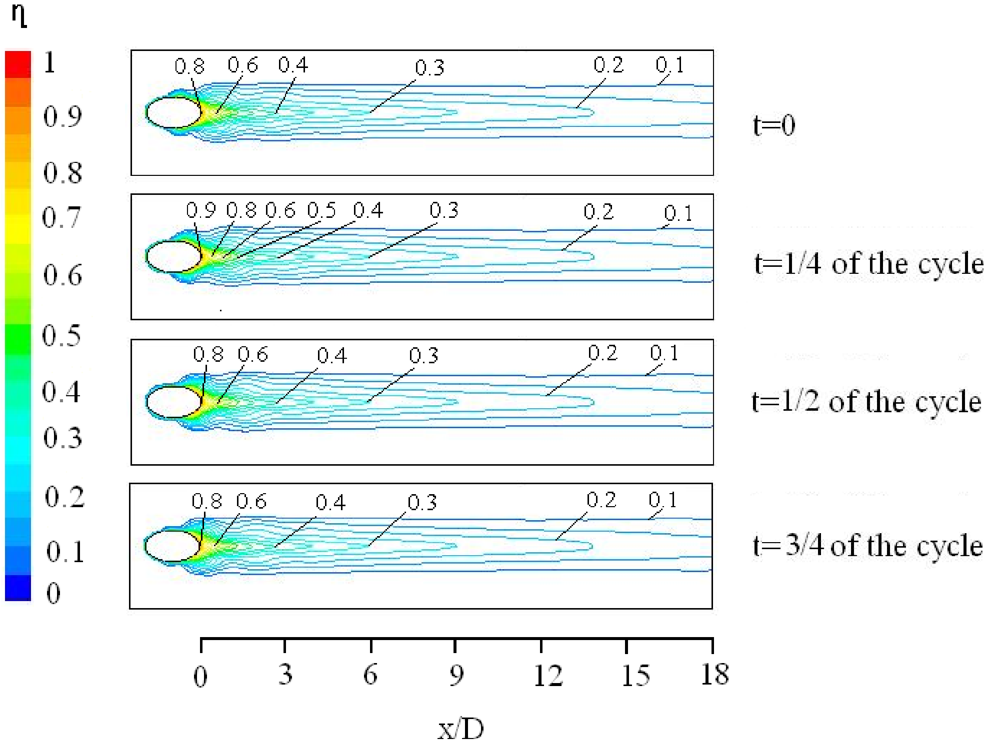

Figure 3.8d: Effectiveness footprints on the test wall downstream of the film hole, B = 0.5, St = 0.38 (CFH geometry)

Figure 3.9b shows the dimensionless temperature contours, for the same case, where the cold fluid fills the whole injection pipe and covers the test wall downstream of the film hole providing the best cooling effectiveness that can be achieved under these conditions. The flow from the plenum inlet was then shut off and the CFD case was run until it reached final steady state conditions. Figure 3.9c shows the velocity contours and vectors in the injection pipe. Velocity of about 3 m/s, in the cross flow direction, is observed at the jet exit plane. Recirculation zone, similar to the cavity-driven flow, is observed in the injection pipe. Figure 3.9d shows the temperature contours for the same case where the hot fluid penetrates into the injection pipe almost up to the plenum exit plane. This observation is significant, as will be seen below in this section in the discussion of the pulsed jet.

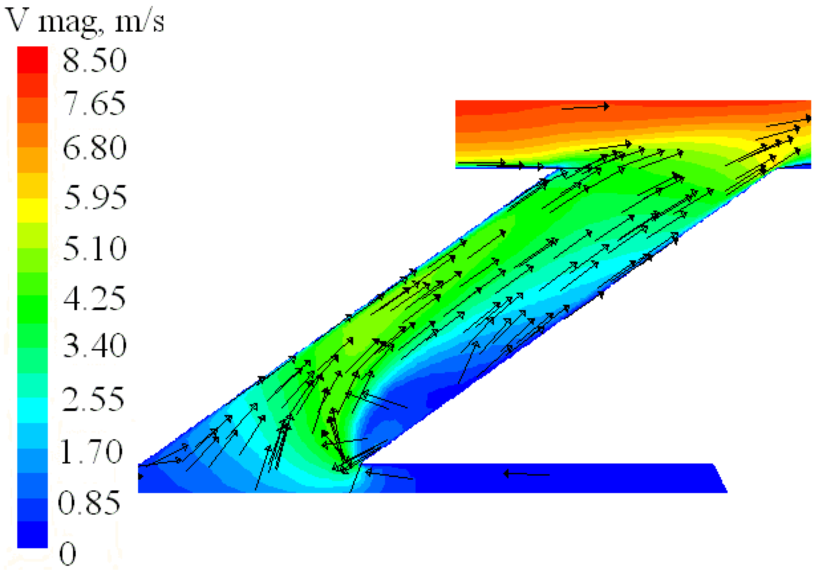

Figure 3.9a: Velocity magnitude contours and vectors, CFH geometry, B=0.5, steady blowing

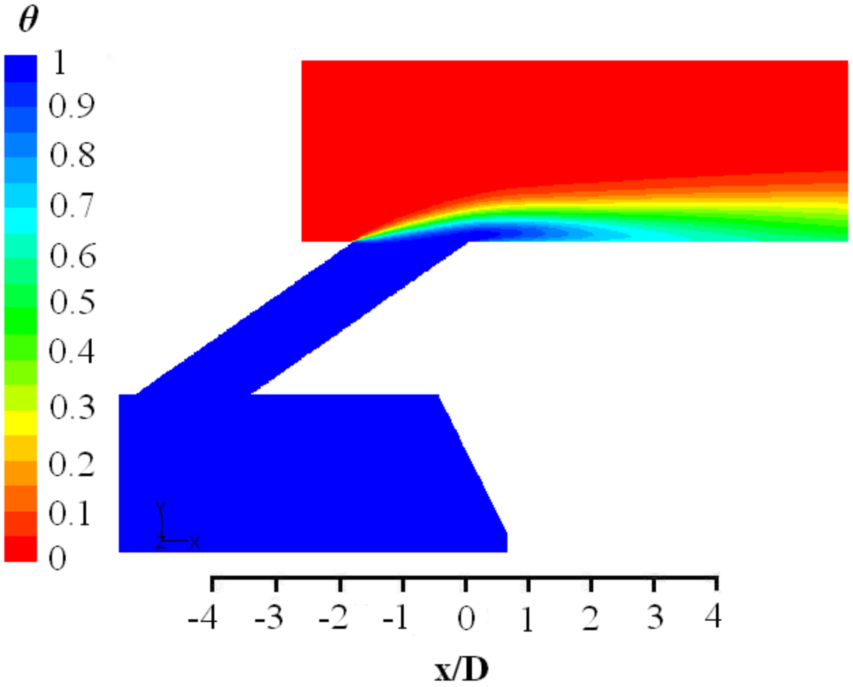

Figure 3.9b: Dimensionless temperature side view, CFH geometry, B=0.5, steady blowing

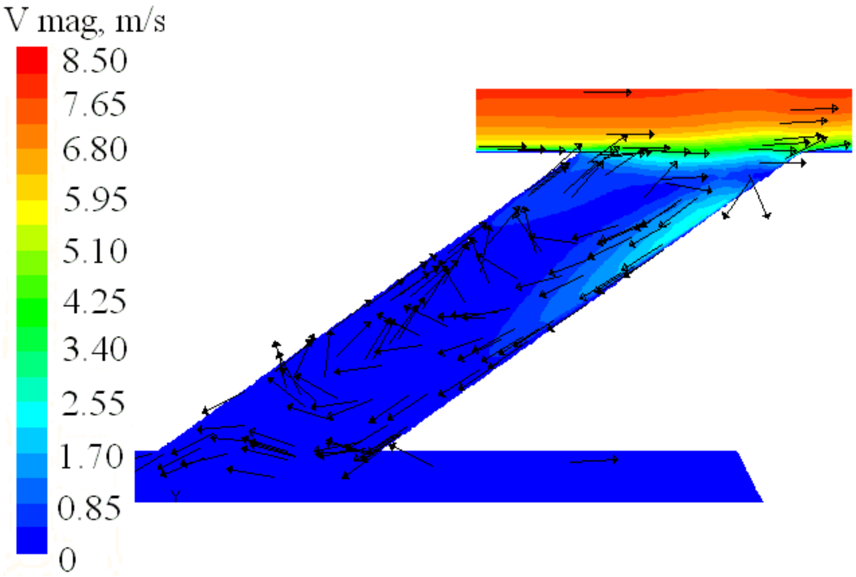

Figure 3.9c: Velocity magnitude contours and vectors, CFH geometry, B=0.5, no blowing

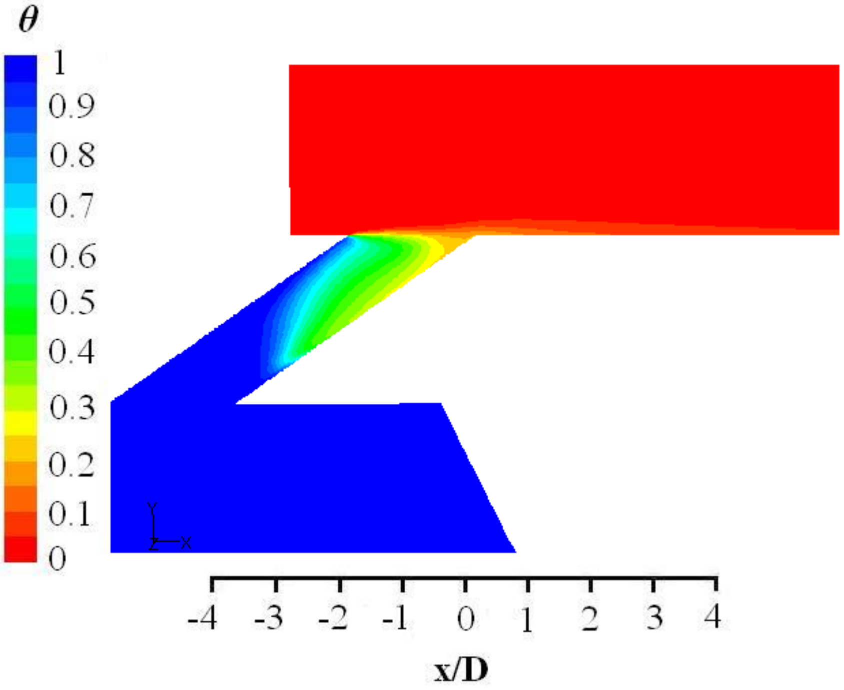

Figure 3.9d: Dimensionless temperature side view, CFH geometry, B=0.5, no blowing

Since part of this investigation is changing the geometry from CFH to LDIFF similar data (to Fig. 3.9a and b) was obtained for the LDIFF geometry (will be discussed in details in section 3.3.4). Figure 3.10a shows the velocity contours and vectors for the steady state case, LDIFF geometry. It can be seen that because of the plenum geometry a non-uniform flow enters the injection pipe with a recirculation near the forward bottom side of the pipe. This, in turn, results in highly non-uniform flow at the jet outlet. A maximum local velocity is 13 m/s, which is 30 % higher than the nominal blowing velocity for the B=1.25 case. Figure 3.10b shows the dimensionless temperature contours, from the steady blowing case, where the cold fluid is filling the whole injection pipe and covers the test wall downstream of the jet providing the best film cooling effectiveness that can be achieved under those conditions. The flow from the plenum inlet was then shut off and the CFD case was run until it reached final steady state conditions. Figure 3.10c shows the velocity contours and vectors in the injection pipe. Velocity of about 7.2 m/s (in the cross flow direction) at the jet exit plane and a recirculation zone similar to the cavity-driven flow were observed.

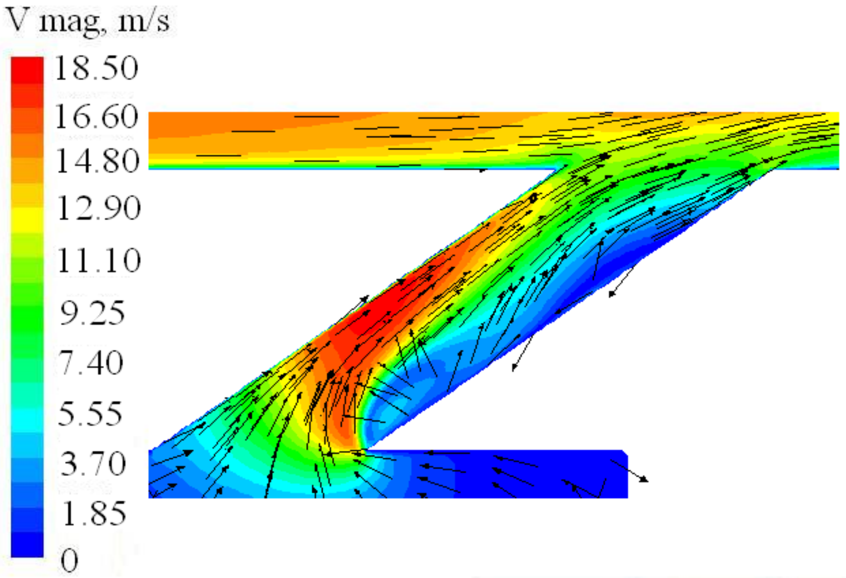

Figure 3.10a: Velocity magnitude contours and vectors, LDIFF geometry, B=1.25, steady blowing

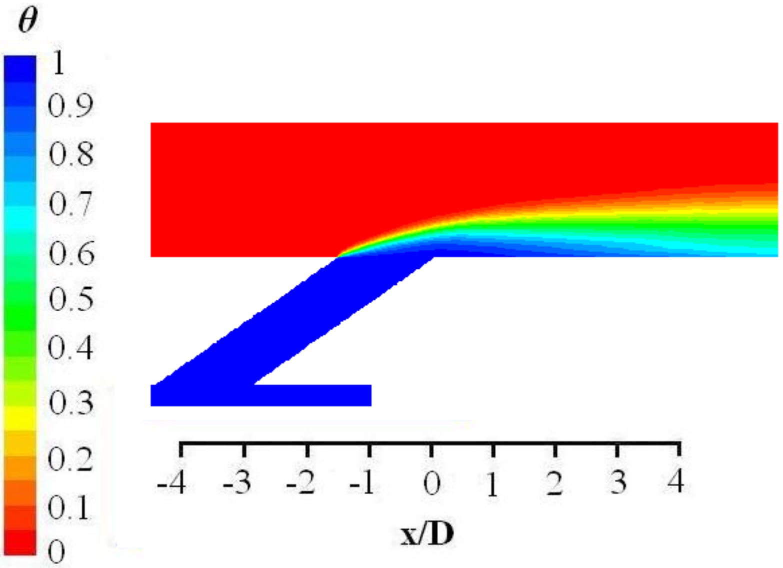

Figure 3.10b: Dimensionless temperature side view, LDIFF geometry, B=1.25, steady blowing

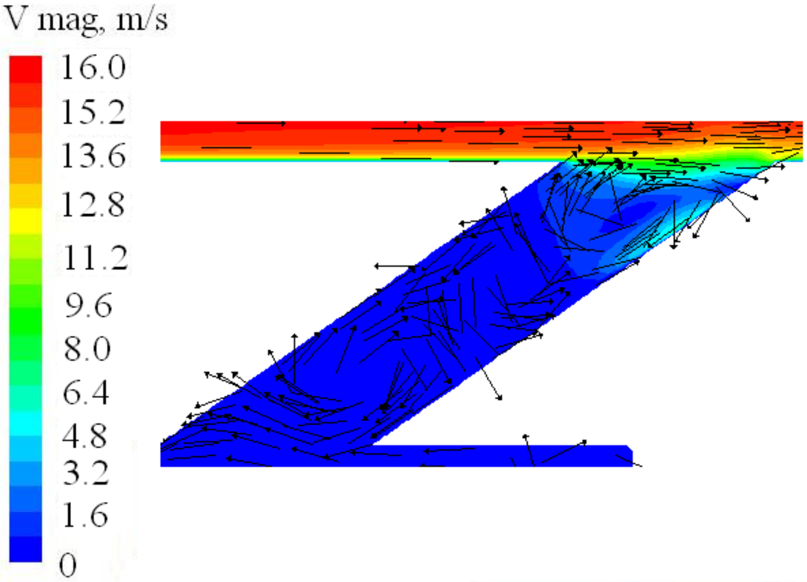

Figure 3.10c: Velocity magnitude contours and vectors, LDIFF geometry, B=1.25, no blowing

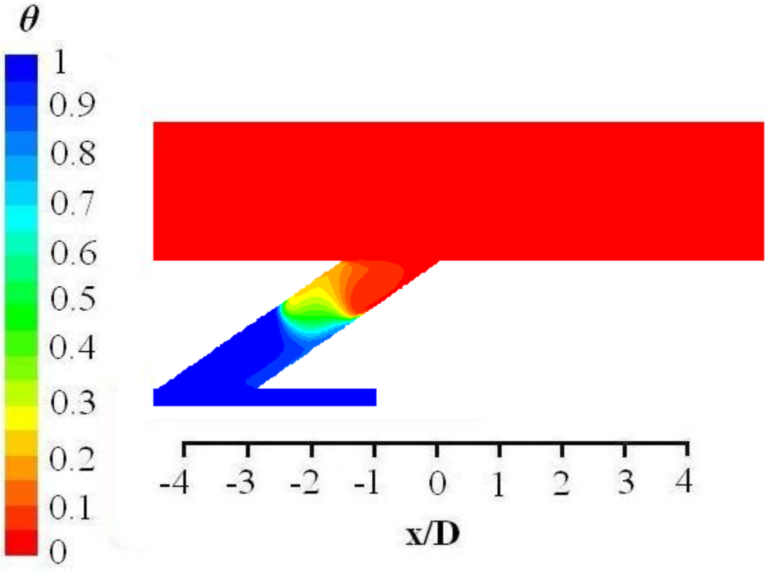

Figure 3.10d: Dimensionless temperature side view, LDIFF geometry, B=1.25, no blowing

Figure 3.10d shows the temperature contours where the hot fluid penetrates into the injection pipe almost up to middle of the pipe. This observation is significant, as will be seen below in section 3.3.4 in the discussion of the pulsed jet for the LDIFF geometry.

Figure 3.11a shows the velocity contours and vectors in the injection pipe for St=0.0119 and at four different times of the cycle (t/T=0, ¼, ½, ¾). The dimensionless temperature contours for this case are shown in Figure 3.11b (side-view), Figure 3.11c (top view of the jet) and they are not with the same scale. At t/T=0 a bubble of hot fluid was seen in the temperature-contour side-view which was the remainder from the previous cycle. Notice this was observed only at the lowest Strouhal number studied. The outcome was the low dimensionless temperature at the jet exit plane as shown in Figure 3.11c. At t/T = ¼ the jet reached a full blown level and appeared very similar to the steady state condition (Figures 3.9a and b) and accordingly the best film cooling effectiveness occurred. At t/T = ½ the flow started to retard in the injection pipe, allowing more flow from the cross stream to get into the pipe. The cooling effectiveness of the jet decreased as shown at the jet-exit plane (Figure 3.11c). Finally at t/T = ¾ the flow penetrated further into the injection pipe allowing a hot bubble to enlarge and reach to more than half of the injection pipe. Accordingly very low film cooling effectiveness was obtained.

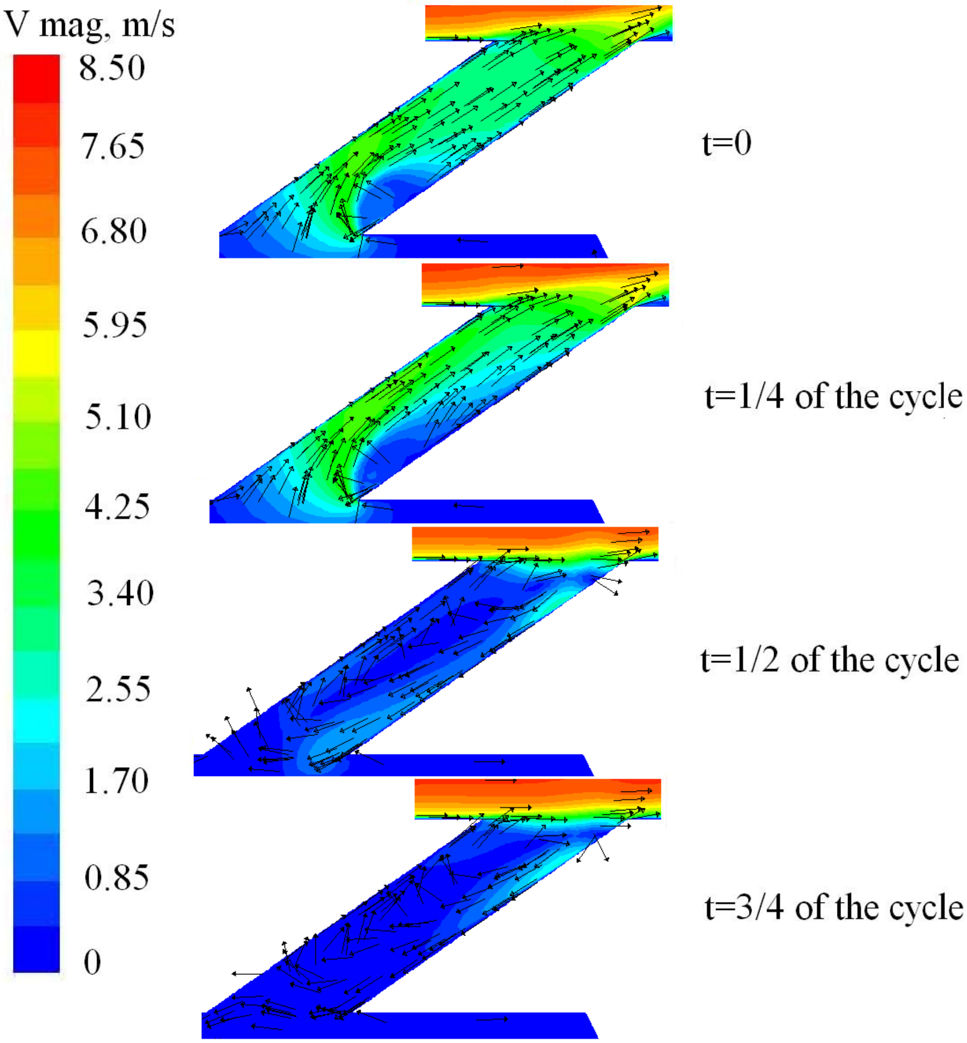

Figure 3.11a: Velocity magnitude contours and vectors, CFH geometry, B = 0.5, St = 0.0119.

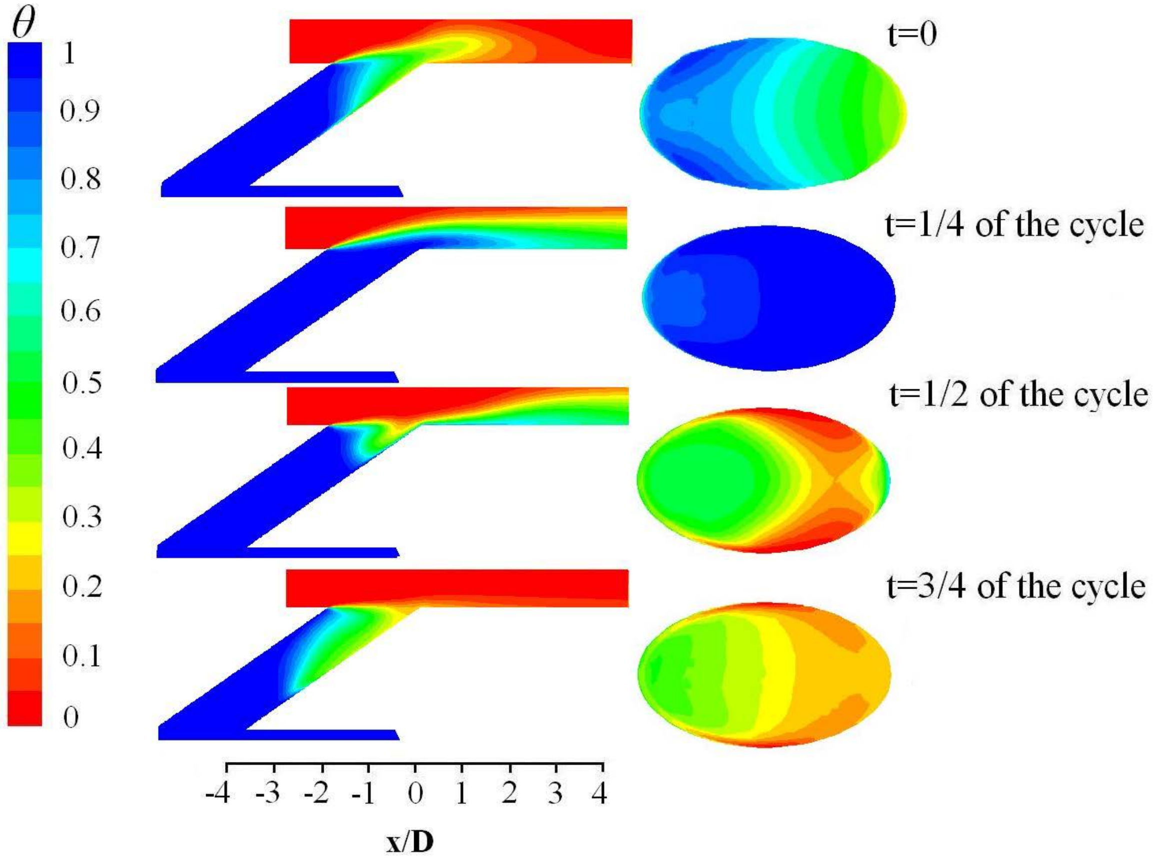

(b) (c)

Figure 3.11b and c: Dimensionless temperature side view - (b) and dimensionless temperature contours at the jet-top – (c), CFH geometry, B = 0.5, St = 0.0119.

Figure 3.12a shows the velocity contours and vectors in the injection pipe for St= 0.19 and at four different times of the cycle (t/T=0, ¼, ½, ¾). The dimensionless temperature contours for this case are shown in Figure 3.12b (side-view) and Figure 3.12c (top view of the jet) and they are not with the same scale. At t/T=0 a smaller (than the previous case with St=0.0119) recirculation zone was seen from the velocity vectors and the temperature-contour side view as a result of the higher frequency (lower cycle time). Thus there was not enough time to form a larger size recirculation zone that would fill the injection pipe (as shown earlier at St=0.0119). At t/T = ¼ the jet does not reach a full blown state (due to lesser cycle time) and thus smaller values of the film cooling effectiveness at the jet exit plane were obtained (compare Fig. 3.12c with Fig. 3.11c at t/T=1/4). At t/T = ½ the flow started to retard in the injection pipe but would not allow more flow from the cross stream to get into the pipe (again due to lesser cycle time). The cooling effectiveness of the jet decreased as shown at the jet-exit plane (Figure 3.12c). Finally at t/T = ¾ the flow penetrated further into the injection pipe allowing a hot bubble to exist in the injection pipe. Accordingly lower film cooling effectiveness was obtained.

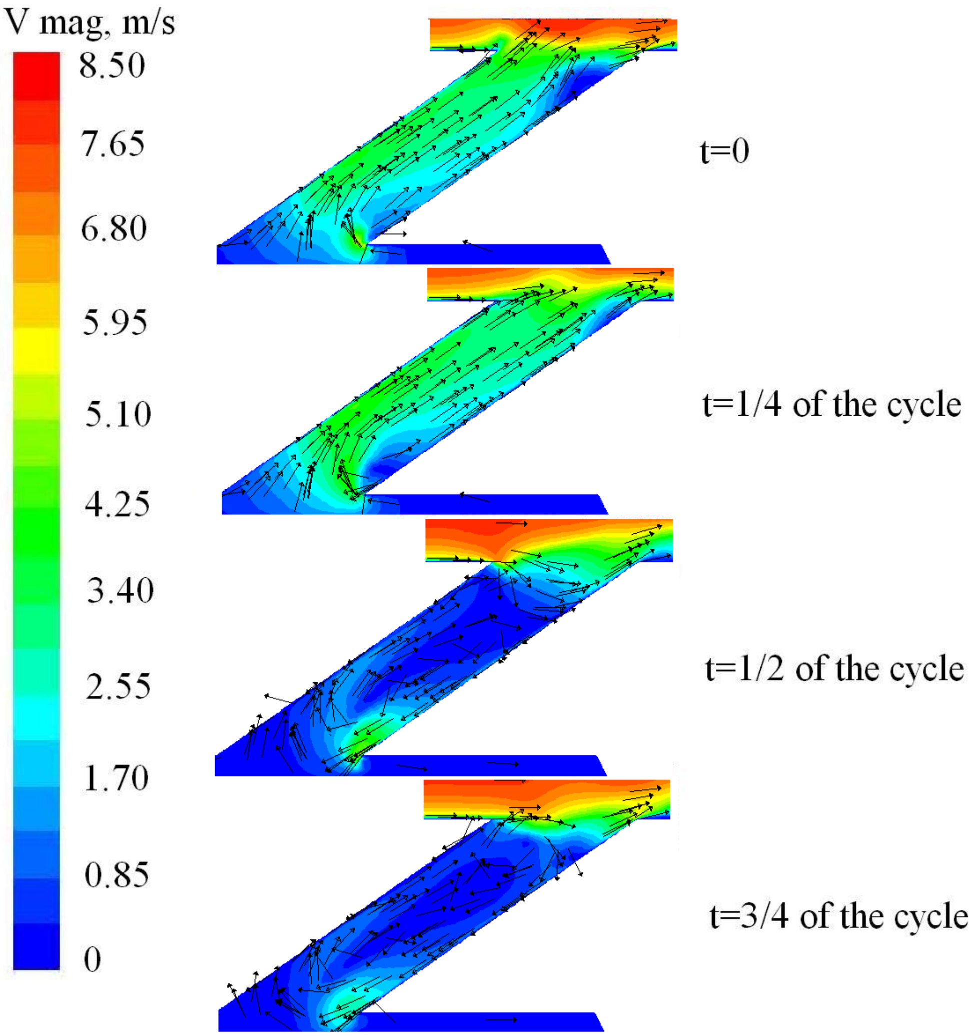

Figure 3.12a: Velocity magnitude contours and vectors, CFH geometry, B = 0.5, St = 0.19

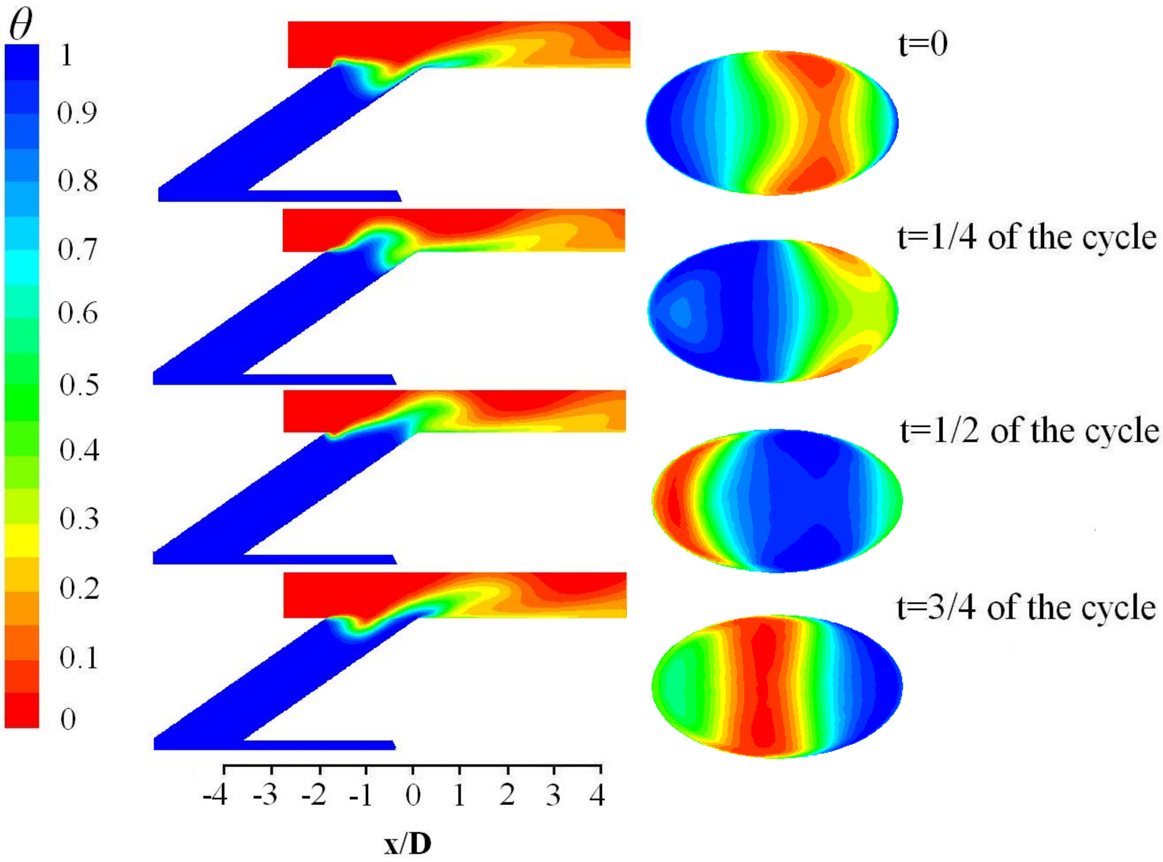

(b) (c)

Figure 3.12b and c: Dimensionless temperature side view - (b) and dimensionless temperature contours at the jet-top – (c), CFH geometry, B = 0.5, St = 0. 19.

Figure 3.13a shows the velocity contours and vectors in the injection pipe for St=0.38 and at four different times of the cycle (t/T=0, ¼, ½, ¾). The dimensionless temperature contours for this case are shown in Figure 3.13b (side-view) and Figure 3.13c (top view of the jet) and they are not with the same scale. At t/T=0 no recirculation zone is seen from the velocity vectors and the temperature-contour side-view as a result of the high frequency (low cycle time) and thus there is not enough time to form that recirculation region inside the injection pipe (as shown earlier at St=0.0119). At t/T = ¼ the jet does not reach a full blown state (due to lesser cycle time) and thus smaller values of the film cooling effectiveness at the jet exit plane were obtained (compare Fig. 3.13c with

Fig. 3.12c at t/T=1/4). At t/T = ½ the flow started to penetrate in the injection pipe but would allow even less flow from the cross stream to get into the pipe (compare Fig. 3.13b, c with Fig. 3.12b, c at t/T=½). This was, again, due to lesser cycle time. The cooling effectiveness of the jet stayed almost the same as shown at the jet-exit plane (Figure 3.13c). Finally at t/T = ¾ there was no much flow penetration into the injection pipe. Therefore, highest film cooling effectiveness was obtained at this time of the cycle compared to other Strouhal number cases.

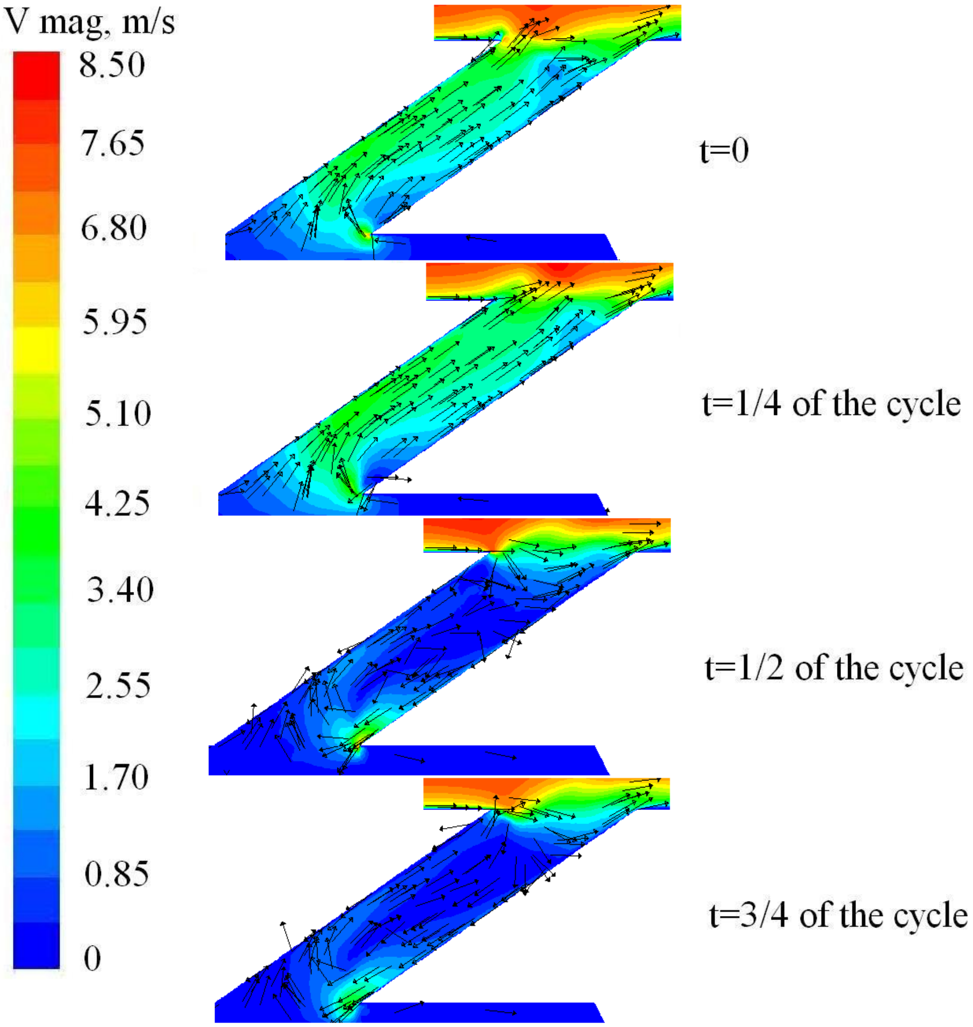

Figure 3.13a: Velocity magnitude contours and vectors, CFH geometry, B = 0.5, St = 0.38

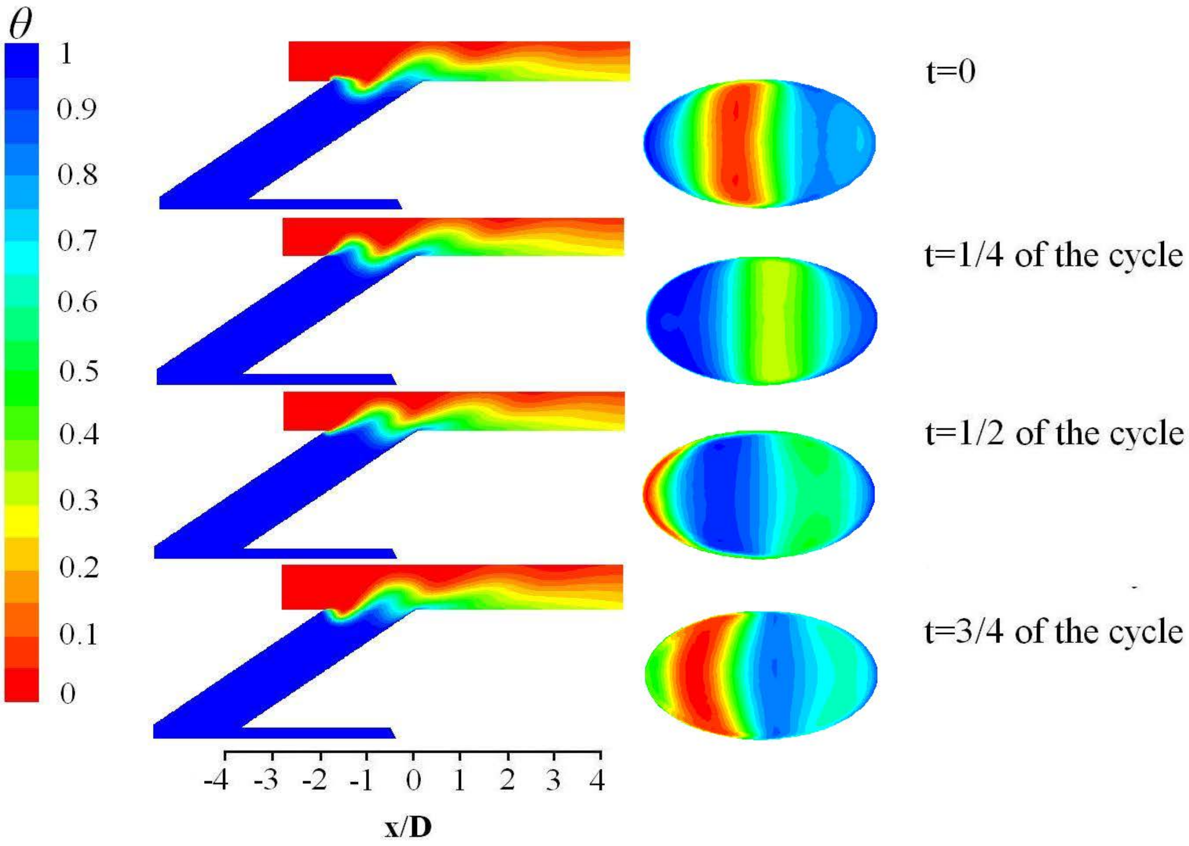

(b) (c)

Figure 3.13b and c: Dimensionless temperature side view - (b) and dimensionless temperature contours at the jet-top – (c), CFH geometry, B = 0.5, St = 0. 38.

From the observations of this section for the different frequencies examined two opposing factors were noticed: a) low frequency (high cycle time) allows more time (during blowing) for jet flow to reach full blown conditions and thus to achieve high film cooling effectiveness, b) this high cycle time, however, provides more time during jet shut-off and thus more time for the cross flow to penetrate and be ingested into the injection pipe. This results in the low values of effectiveness during shut-off and the beginning of the blowing time. The net effect of the above two factors is what was shown earlier in Figure 3.7. It should be noted that those observations are geometry dependent as they apply only to CFH geometry. For the LDIFF geometry, which will be discussed later in section 3.3.4, the effect of pulsation frequency was almost negligible.

3.3.3 Effect of Jet Blowing Ratio

Two different blowing ratios were examined as was described earlier, for the CFH geometry with steady blowing and pulsed jets with St=0.0119, 0.19, 0.38 and 1.0. Figure 3.14a shows the centerline (time averaged) film cooling effectiveness for the CFH geometry with B =1.5 (to be compared with Fig. 3.7a for B=0.5). Figure 3.14b shows the span-wise averaged (time averaged) effectiveness under similar conditions. Since the effect of pulsation was very small in the spanwise compared to the centerline effectiveness our focus will be on results shown in Fig. 3.14a. First, as expected, for steady state as the blowing ratio changed from 0.5 to 1.5 the film cooling effectiveness became much lower everywhere due to the jet lift-off at the higher B values. The pulsation had different effects in the two cases. At B=0.5 (as discussed earlier in section 3.3.2) lower effectiveness was obtained everywhere in cases with jet pulsation, compared to the steady blowing case. For B=1.5 pulsation results were highly dependent on the frequency. For low frequency (St=0.0119) the effectiveness values were below the values from the steady blowing case at all x/D locations. For higher frequency (St=0.38) the effectiveness values were higher than the steady blowing case values at all x/D locations. As for St=0.19 and 1.0 the results were in between the results of the St=0.0119 and St=0.38. In order to understand this behavior better, Figures 3.15 and 3.16 are shown.

Fig. 3.15 shows the effectiveness footprints on the wall downstream of the film hole for the B = 1.5 case, for: 3.15a - steady blowing, and 3.15b - St = 0.38. The footprints are shown at different times in the pulsation cycle with 50% duty cycle, at t/T=0 (the beginning of blowing), t/T = ¼ (middle of blowing), t/T = ½ (end of blowing), and, finally, at t/T = ¾ (middle of no blowing).

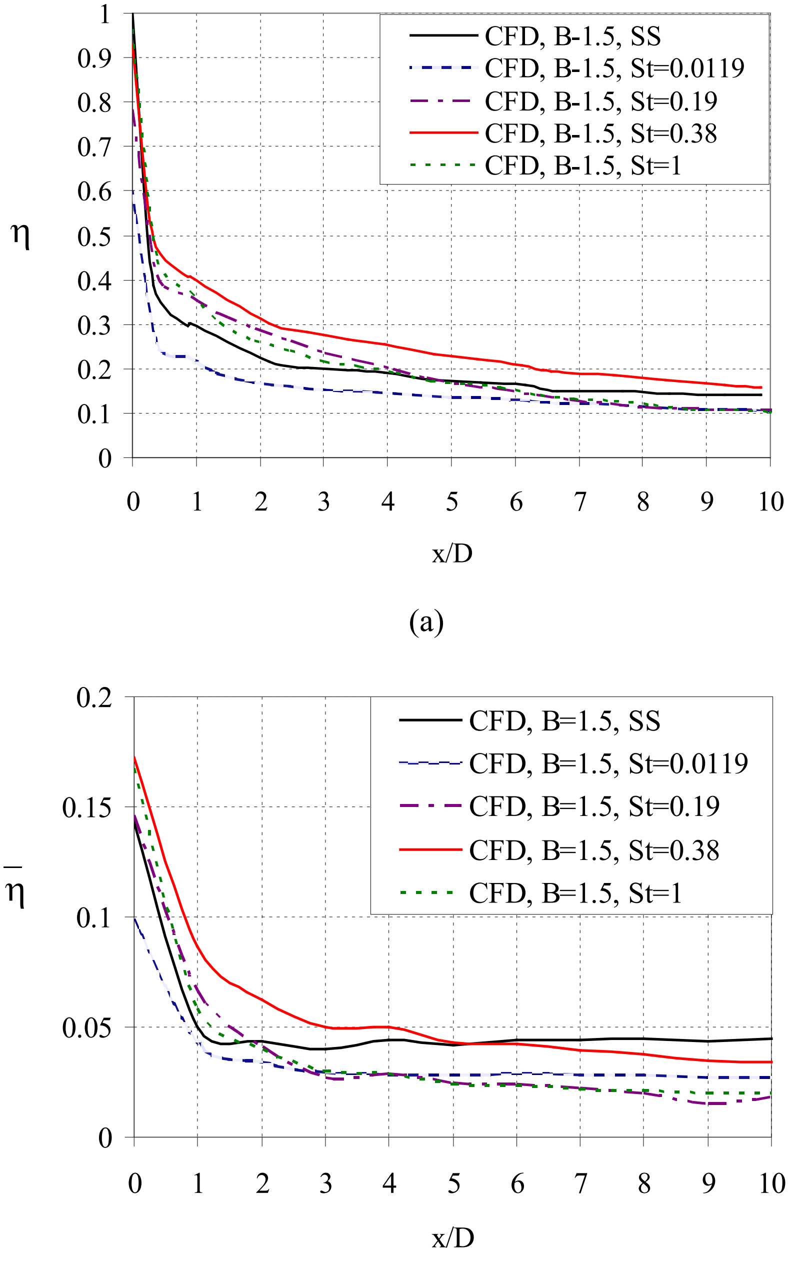

(a)

…..

(b)

Figure 3.14: Centerline - (a) and spanwise averaged (b) plot of adiabatic film cooling effectiveness for B = 1.5 steady blowing and different Strouhal numbers (CFH geometry)

Figure 3.15a shows the steady blowing case with low effectiveness downstream of the jet. Figure 3.15b shows the results of the St = 0.38 case where the effectiveness values are higher than the ones from the steady blowing case at all times of the cycle. This, of course, results in a higher time averaged film cooling effectiveness (at all x/D locations) as shown in Fig. 13a, which values are larger than the effectiveness values from the steady blowing case.

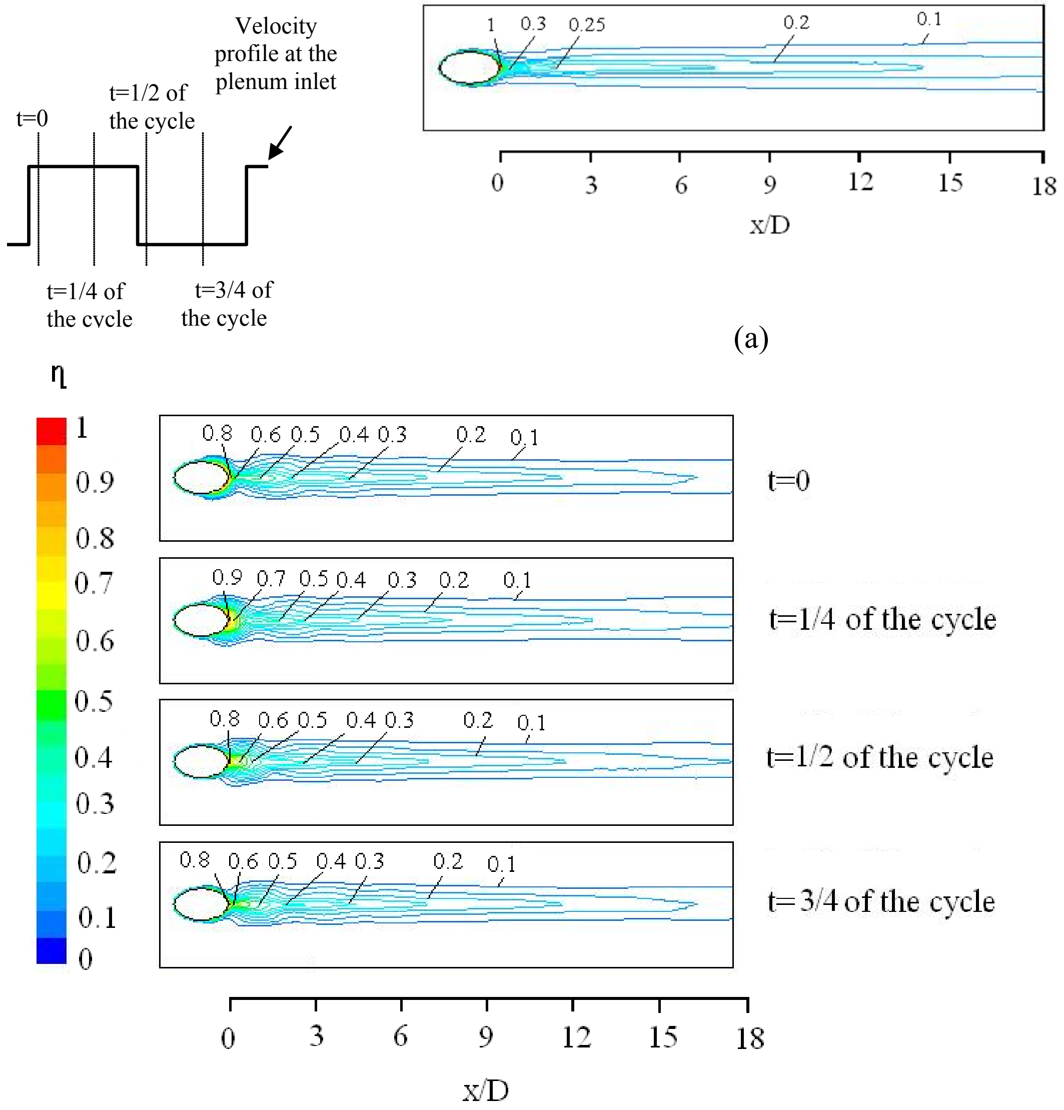

Figure 3.15: Effectiveness footprints on the test wall downstream of the film hole, B = 1.5 (a) steady blowing; (b) St = 0.38.

Figure 3.16a shows the dimensionless temperature contours (sideview), for the steady high blowing ratio case (B=1.5). The dimensionless temperature contours (sideview) at four different times of the cycle (t/T=0, ¼, ½, ¾) are shown for St=0.0119 (Fig. 3.16b), St=0.38 (Fig. 3.16c) and St=1.0 (Fig. 3.16d) cases. Figure 3.16a shows the jet lift-off that results in a low film cooling effectiveness.

Figure 3.16b (St=0.0119) shows how the high cycle time (low frequency) results in two mechanisms: 1) jet lift-off exists (while jet is open) and 2) cross flow is ingested into the injection pipe (while jet is closed). Both factors affect the effectiveness negatively and result in lower values at all x/D locations (compared to the steady blowing case).

Figure 3.16c (St=0.38) shows how the jet breaks up due to both the jet left-off and pulsation which provides a continuous supply of coolant on the top surface and thus higher effectiveness at all x/D value (compared to steady state).

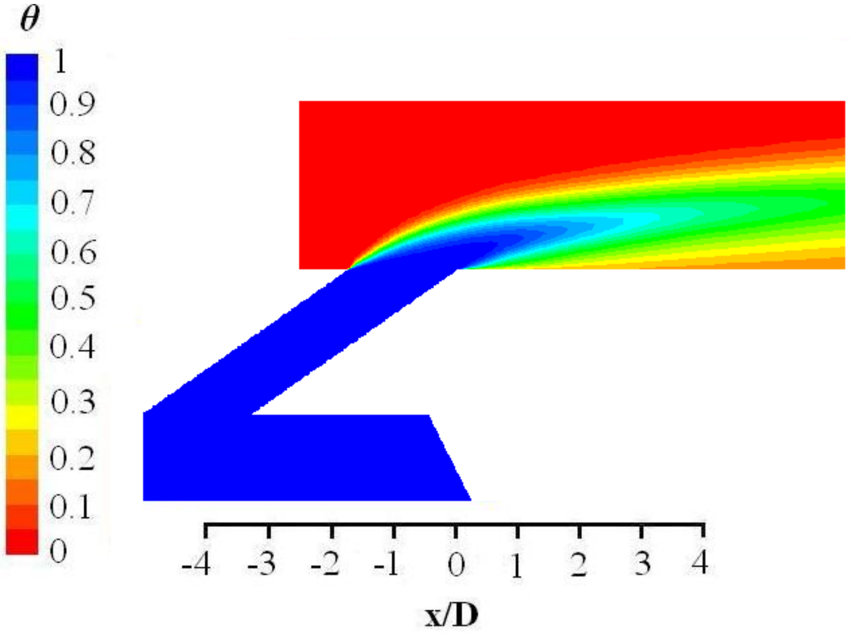

Figure 3.16a: Dimensionless temperature side view, CFH geometry, B=1.5, steady blowing

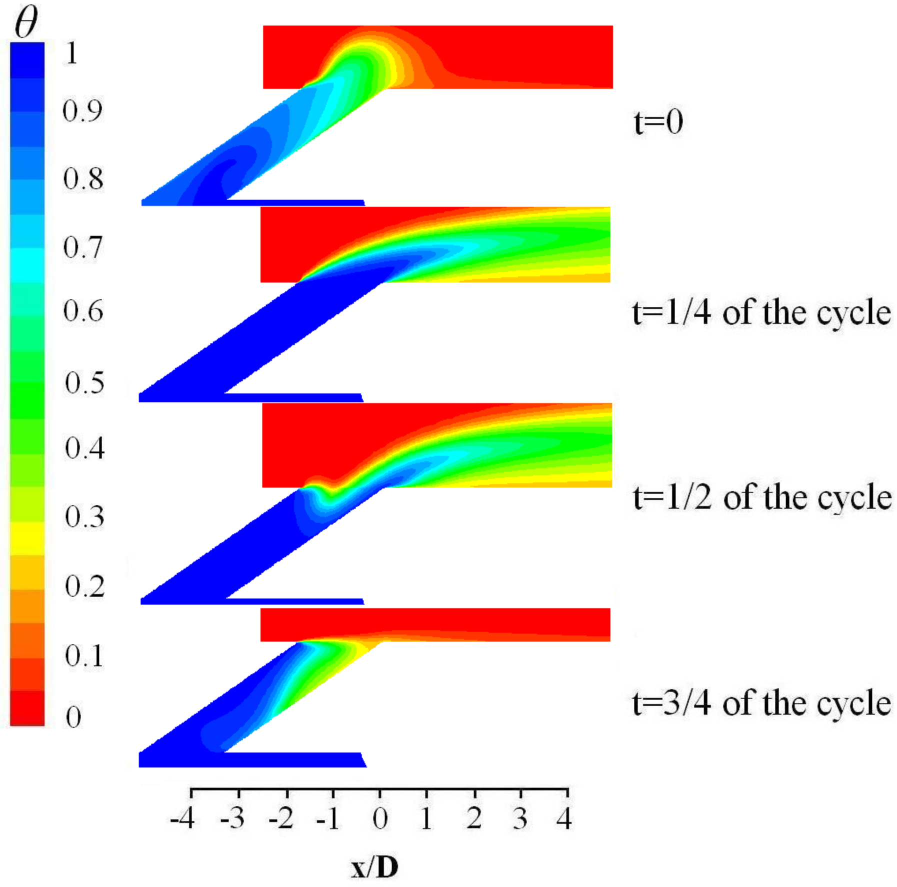

Figure 3.16b: Dimensionless temperature side view, CFH geometry, B=1.5, St = 0.0119

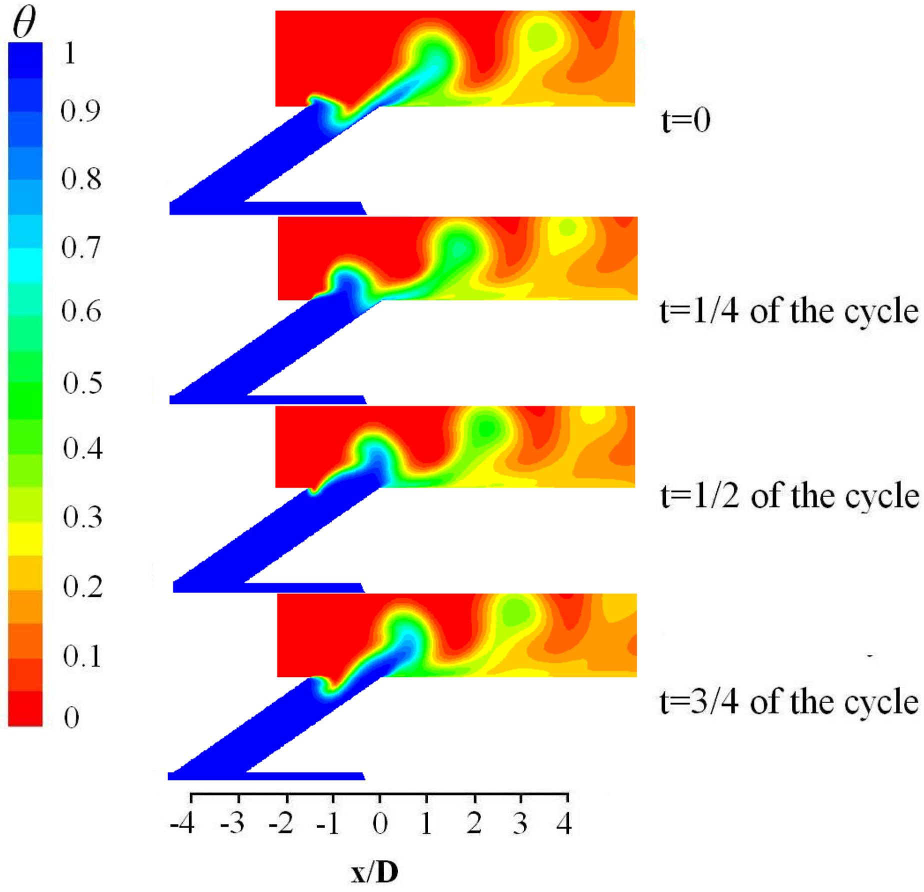

Figure 3.16c: Dimensionless temperature side view, CFH geometry, B=1.5, St = 0.38

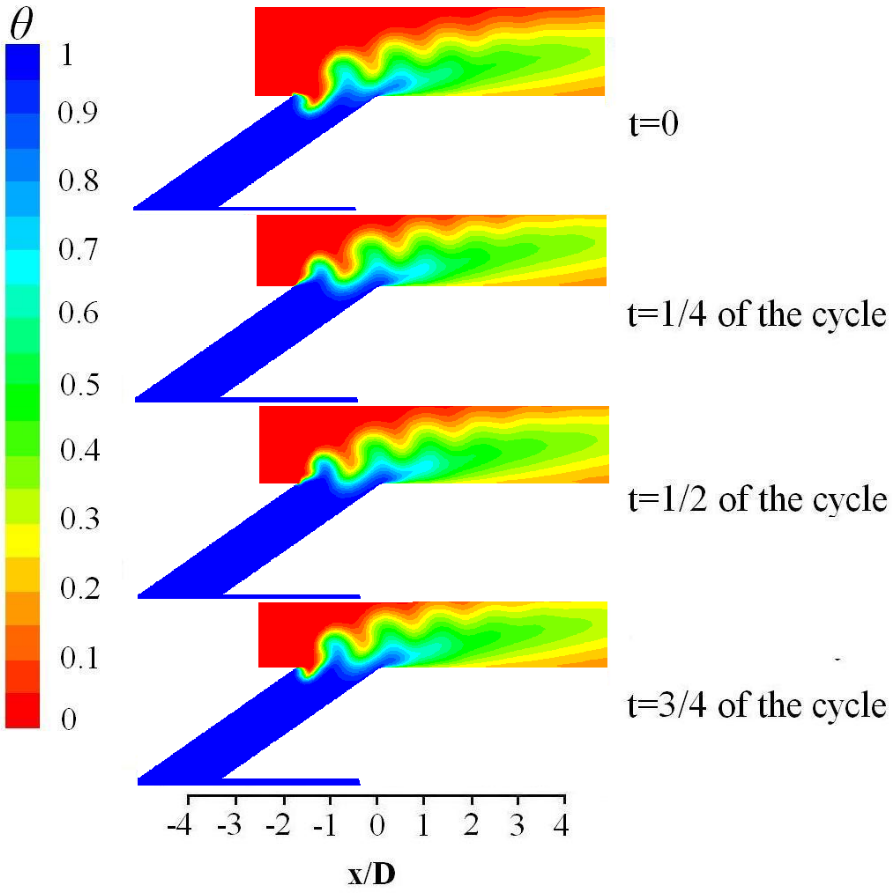

Figure 3.16d: Dimensionless temperature side view, CFH geometry, B=1.5, St = 1

Figure 3.16d (St=1.0) shows that the jet lift-off exists throughout the duration of the cycle and only the upper part of the jet (which interacts with the cross stream) is affected by the pulsation. This, in turn, results in lower centerline effectiveness compared to the case with St=0.38 but slightly higher than in the steady blowing case.

3.3.4 Effect of Jet geometry

Two different geometries (CFH and LDIFF) were examined, as was described earlier. Figure 3.17a shows the centerline (time averaged) film cooling effectiveness for the LDIFF geometry with B =1.25, steady state, St = 0.0119, 0.19 and 0.38.

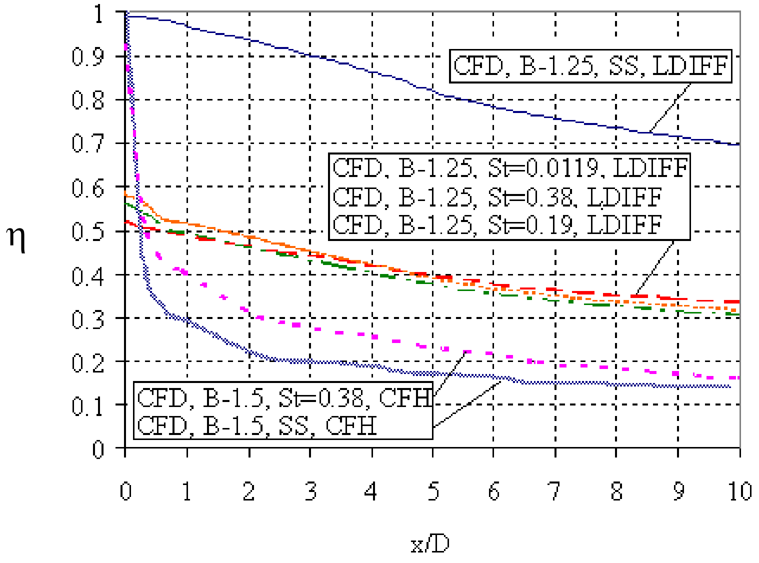

(a)

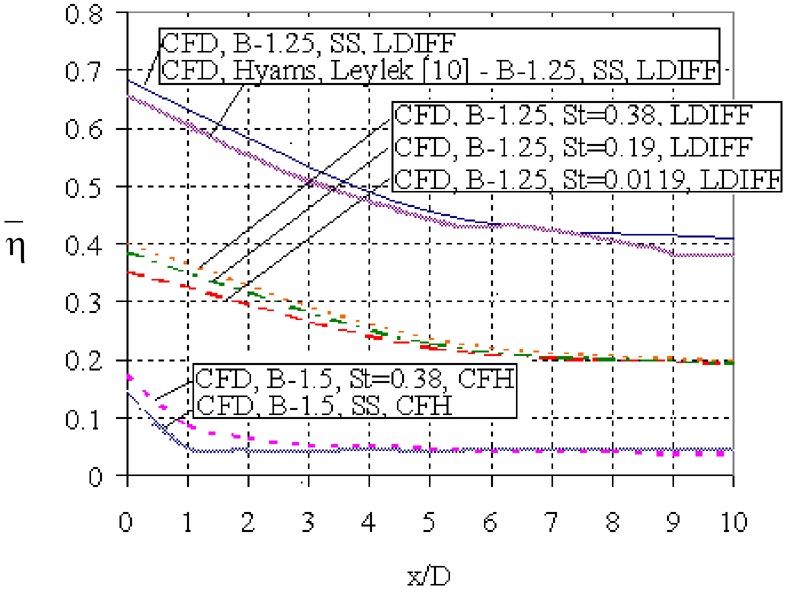

(b)

Figure 3.17: Time averaged, adiabatic film cooling effectiveness:
a - centerline, b - spanwise averaged
(LDIFF geometry, B=1.25 compared to CFH geometry, B=1.5)

Also the results for CFH geometry with B = 1.5, steady state and St = 0.38 are shown on the same plot. Figure 3.17b shows similar results to Figure 3.17a but for the spanwise averaged (and time averaged) film cooling effectiveness. The data shows that the two geometries were affected differently by jet pulsation.

CFH geometry showed higher film cooling effectiveness (both the center line and spanwise averaged) under steady blowing conditions for B=0.5 compared to the pulsed jet conditions. For B=1.5 this was not true. Two important observations were noticed for this geometry: 1) for B = 0.5, the effect of the pulsation did lower the film cooling effectiveness everywhere with the worst performance for St=0.19 and the best for St=1.0 (which still is lower than the steady blowing case values), 2) for B = 1.5 and St= 0.0119 the pulsation resulted in lower (than the steady blowing case value) effectiveness at all x/D locations, 3) for B= 1.5 and St=0.38 the pulsation resulted in higher (than the steady blowing case value) effectiveness at all x/D locations; other frequencies tested showed results which were in between the above two. On the other hand, the LDIFF geometry showed resulted in higher film cooling effectiveness values (both the center line and spanwise averaged) under steady blowing conditions compared to the CFH geometry. Upon employing a pulsed jet for the LDIFF geometry two important results were noticed: 1) the effect of the pulsation caused the film cooling effectiveness to decrease everywhere, 2) the effect of changing the pulsation frequency (from St=0.0119 to 0.38) was almost negligible.

Figure 3.18 shows the effectiveness footprints on the wall downstream of the film hole for LDIFF geometry with B = 1.25. Figure 3.18a shows steady blowing case results; Fig. 3.18b is for St = 0.0119 and Fig. 3.18c is for St = 0.38 case. The results are shown at four different times in the cycle (t/T = 0, ¼, ½ and ¾).

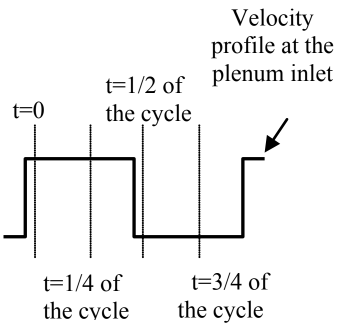

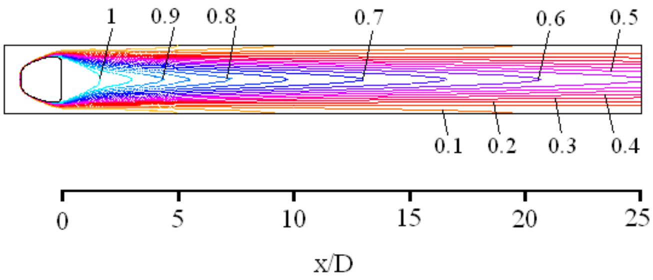

Figure 3.18a: Effectiveness footprints on the test wall downstream of the film hole, B = 1.25, LDIFF geometry, steady blowing.

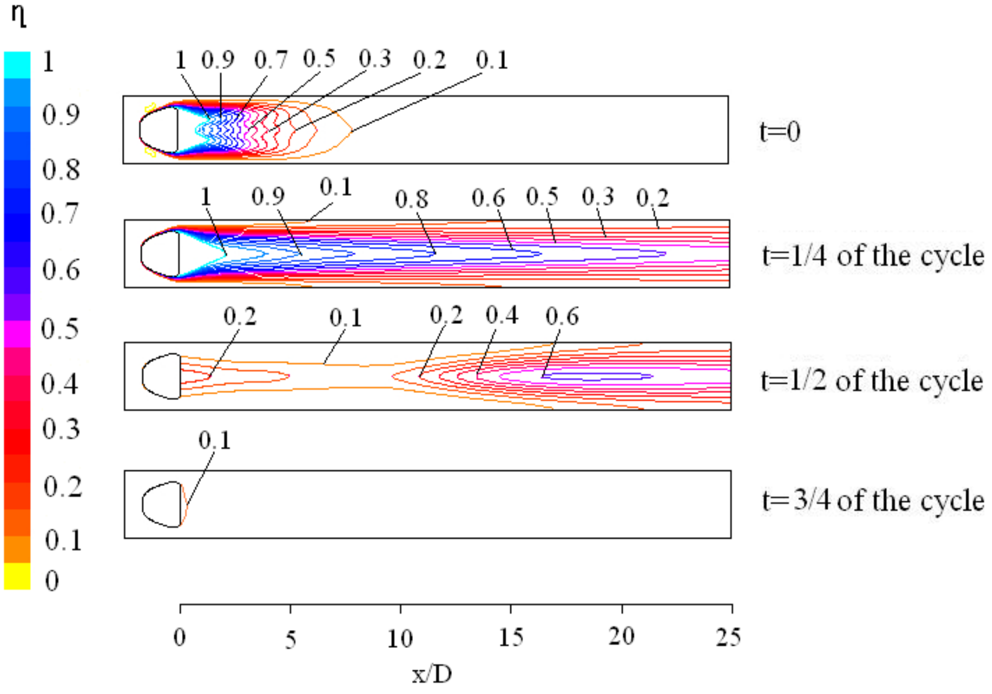

Figure 3.18b: Effectiveness footprints on the test wall downstream of the film hole, B = 1.25, LDIFF geometry, St = 0.0119.

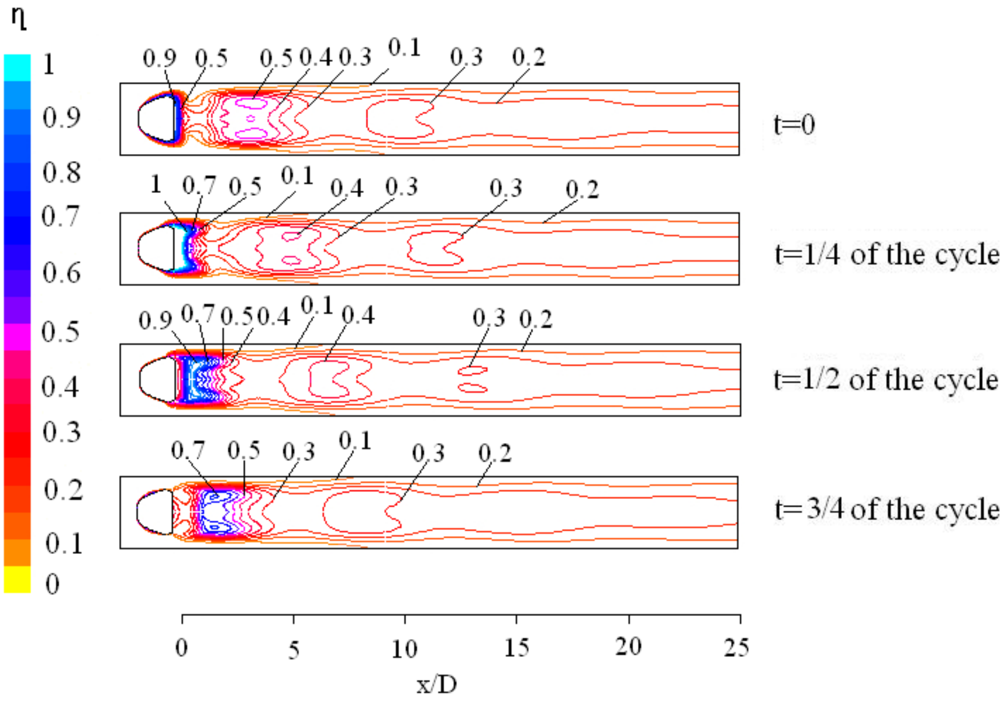

(c)

Figure 3.18c: Effectiveness footprints on the test wall downstream of the film hole, B = 1.25, LDIFF geometry, St = 0.0119

The effectiveness footprints show lower values everywhere and at all times, for the two frequencies (corresponding to St=0.0119 and St=0.38), compared to the steady blowing case results.

3.3.5 Spatially Averaged Film Cooling Effectiveness

The film cooling effectiveness examined in sections 3.3.1 – 3.3.4 varied spatially and temporally. Spatially averaged effectiveness was used to compare "overall" performance of all cases examined. An area downstream the jet that covers from the jet "trailing edge", x/D = 0 to x/D =10 and also covers a ½ pitch on both sides of the jet in the spanwise direction was chosen. It is clear that the area choice might alter the results of this section. The film cooling effectiveness was averaged over this area spatially and then temporally. Figure 3.19 shows this spatially averaged effectiveness plotted versus the coolant mass flow rate (kg/s) for all cases examined.

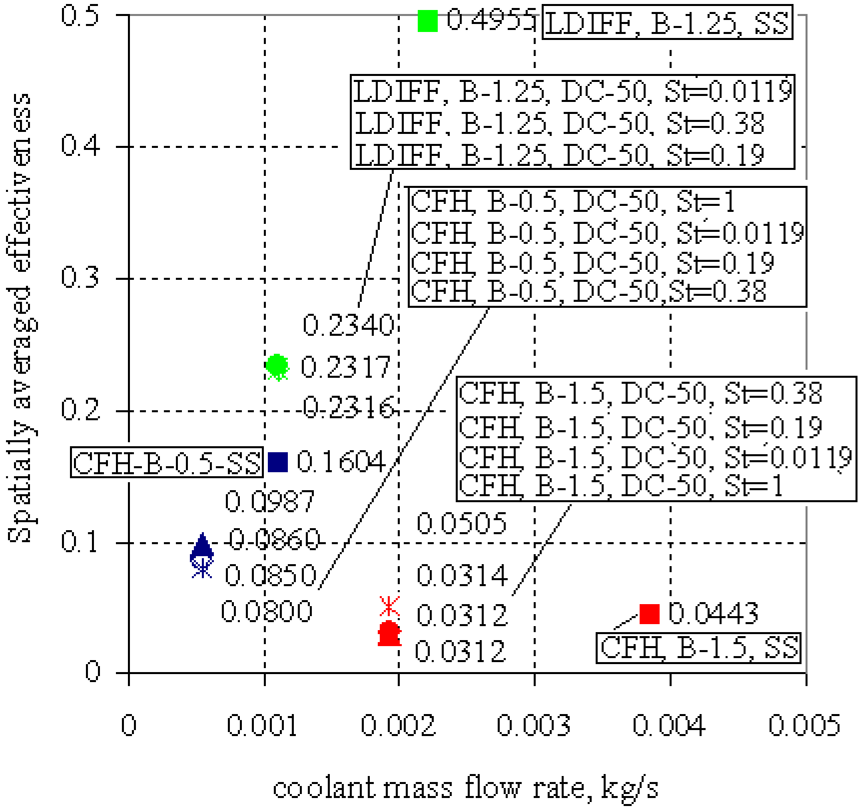

Figure 3.19: Film cooling effectiveness, averaged over x/D = 10 by z/D = 3 area, for all film cooling cases examined

The results are summarized in Table 3.2. As noted earlier the Duty Cycle in the present study was kept constant at 50%. Table 3.2 shows that when using the defined spatially averaged effectiveness and 50% of the coolant an overall reduction in the film cooling effectiveness was: 52.73% for the LDIFF geometry (B=1.25), 38.12% for the CFH geometry (B=0.5) and an overall enhancement of 14.77% for the CFH geometry (B=1.5).

Those results indicate that jet pulsation is effective for the cases with detached jets (e.g. CFH geometry and B = 1.5) under steady blowing conditions.

Table 3.2: Spatially averaged film cooling effectiveness ($\overline{\eta}$) for all film cooling cases examined

Geometry	Blowing ratio	$\overline{\eta}$ for steady state	$\overline{\eta}$ (highest value) for Pulsed Jet	$\overline{\eta}$ % change (Pulsed/steady state-1)*100
LDIFF	1.25	0.495	0.234	-52.73
CFH	0.5	0.16	0.099	-38.12
CFH	1.5	0.044	0.0505	14.77

Pulsed jets performance significantly depends on pulsation frequency, blowing ratio and geometry. Another important factor is the pulsed jet attenuation due to the plenum geometry. While a square flow wave was applied at the plenum inlet, the flow that comes out of the jet depends on: plenum geometry, jet geometry, pulsation frequency and blowing ratio among others.

Pulsation helps to lower the amount of cool air from compressor, which is desirable for film cooling applications. However, for the conditions in which steady blowing performs well pulsation considerably decreases the film cooling effectiveness. For the cases, where steady blowing gives poor results due to the detached jet, (higher blowing ratios), pulsation helps to increase time and distance averaged effectiveness (provides reduction in jet "lift-off") when coolant amount decreases. Although pulsation doesn't bring overall benefit to film cooling, there are cases where pulsed jets help to increase effectiveness over steady state case. Therefore, present results might be used to evaluate the effect of pulse frequency on film cooling effectiveness in the real life gas turbine applications, where jets pulse naturally due to the pressure fluctuations in the engine.

In the present study 10 CFD cases for CFH geometry and 4 cases for LDIFF geometry were investigated computationally in an attempt to understand the flow and heat transfer mechanisms that govern the effectiveness of film cooling of flat plates. Those cases included different blowing ratios, 0.5, 1.25 and 1.5, and both steady flow and pulsed jets. In the jet pulsation cases the Duty Cycle was kept the same throughout at 50% while the Strouhal number was changed from 0.0119 to 1.0. Those Strouhal numbers are based on the free stream velocity and jet diameter. Present CFD code with RKE turbulence model was validated by comparing its results with experimental and CFD data, including DNS, for both steady film cooling flow and unsteady pulsed jets. This provided a great confidence in the model and thus allowed its use for an investigation of how the pulsed jet was affected by varying: 1) pulsation frequency, 2) blowing ratio and 3) jet geometry.

The effect of pulsation frequency was examined for CFH geometry, B=0.5 and 1.5, St = 0.0119, 0.19, 0.38 and 1.0. As for the LDIFF geometry, B=1.25, St = 0.0119, 0.19, and 0.38 were considered. Since the effect of pulsation was very small in the span-wise compared to the centerline effectiveness (as observed experimentally, Coulthard et al., (2006)) the focus of this study was on results for the centerline effectiveness. For the CFH geometry (B=0.5) the pulsed jet showed lower film cooling effectiveness than the steady state for all cases examined. However, the effect of frequency varied according to the downstream location from the jet exit. Immediately near the jet trailing edge the effectiveness increased as the frequency increased. Downstream of the x/D = 3 location the effectiveness values for both St=0.0119 and 0.38 almost agreed while lower effectiveness values were obtained for St= 0.19. For St=1.0, the effectiveness was above the other frequencies (for all x/D values) but still below the steady state ones. As for the LDIFF geometry (B=1.25) the effect of frequency was negligible and the pulsed jet resulted in the lower film cooling effectiveness than the steady blowing one.

From the above different frequencies examined and for the CFH geometry, two opposing factors were noticed: a) low frequency (high cycle time) allows more time (during blowing) for jet flow to reach full blown conditions and thus film cooling effectiveness to be close to the one from the steady blowing case, b) this high cycle time, however, provides more time during jet shut-off and thus more time for the cross flow to penetrate and to be ingested into the injection pipe. This will create low effectiveness during shut-off and the beginning of the blowing time. It should be noted that those observations are geometry dependent as they apply only to CFH geometry. For LDIFF the effect of frequency pulsation is almost negligible.

Two different blowing ratios (0.5 and 1.5) were examined for the CFH geometry. The pulsation had different effects in the two cases. At B=0.5 lower effectiveness was obtained everywhere for pulsed cases compared to steady ones. For B=1.5 pulsation results were highly dependent on the frequency. For low frequency (St=0.0119) the effectiveness was below the steady state one for all x/D values. For higher frequency (St=0.38) the effectiveness was higher than the steady state values for all downstream x/D locations. As for St=0.19 and 1.0 the results were in between the above two frequencies. At St=0.0119 (high cycle time) two mechanisms took place: 1) jet lift-off occurred (while jet was open) and 2) cross stream flow was ingested into the injection pipe (while jet was closed). Both factors affect the effectiveness negatively and result in lower values at all downstream x/D locations (compared to the steady blowing ones). At

St=0.38 the jet broke up due to both the jet lift-off and pulsation which provided a continuous supply of coolant on the top surface and thus higher effectiveness at all x/D value (compared to the steady blowing case). For St=1.0 the jet lift-off exists throughout the duration of the cycle and only the upper part of the jet (which interacts with the cross stream) is affected by the pulsation. This in turn resulted in lower centerline effectiveness compared to the case with St=0.38 but slightly higher than the steady state one.

A spatially averaged effectiveness ($\overline{\eta}$) was used to compare "overall" performance of all cases examined. This was done by choosing an area downstream the jet that covered from the jet "trailing edge", x/D = 0 to x/D =10 and also covered a ½ pitch on both sides of the jet in the spanwise direction. The area choice, of course, might alter the results of this section. Then the film cooling effectiveness was averaged over this area spatially and then temporally. Using the defined $\overline{\eta}$ with 50% of the coolant (Duty Cycle) an overall reduction in the film cooling effectiveness was found to be: 52.73% for the LDIFF geometry (B=1.25), 38.12% for the CFH geometry with low blowing ratio (B=0.5) and an overall enhancement of 14.77% for the CFH geometry with high blowing ratio (B=1.5). These results clearly indicate that jet pulsation is effective for the cases with lower values of the spatially averaged film cooling effectiveness under steady blowing conditions due to the detached jet.

CHAPTER IV

PART 2: FLOW CONTROL OVER LPT AIRFOIL USING PULSED VGJs

4.1 Literature Review

Review of the studies of the Low Pressure Turbine (LPT) airfoil flow will be followed by the flow control literature review in this section. The material is organized in a way that the experimental studies are discussed first, followed by the review of computational work.

4.1.1 Flow Separation and Transition on LPT Airfoils

A great number of experimental and numerical investigations had been carried out in order to better understand the mechanisms of flow separation and transition on Low Pressure Turbine (LPT) airfoils.

Previous experimental work shows that the strong acceleration on the leading section of the airfoil keeps the boundary layer thin and laminar, even in the presence of elevated freestream turbulence. Some recent examples of those experimental studies are: Volino (2002a, b), Mahallati et al., (2007a, b), Zoric et al., (2007), and Zhang and Hodson (2007). Downstream of the suction peak the adverse pressure gradient can cause boundary layer separation, which may be followed by transition to turbulence and flow reattachment (Volino, 2002, a, b)).

A reduction in the production costs as well as the weight of an engine can be achieved by increasing the loading on LPT airfoils, thereby allowing a reduction in the number of LPT blades. Therefore, very highly loaded airfoils are of great interest. Volino (2008) experimentally studied the flow over a very highly loaded LPT airfoil, designed at the Air Force Research Laboratory (AFRL) and designated L1A. The L1A is available on a limited basis to US researchers from Clark (2007). Volino (2008) reported that for the low Reynolds numbers examined (*Re* = 25,000 – 125,000, based on exit velocity and suction side length) the flow separated and never reattached, even after transition to turbulence. For the higher Re (*Re* = 200,000 - 300,000) a very thin separation bubble was observed and the flow quickly reattached after transition occurred. Volino (2008) concluded that L1A differs from many previously studied LPT airfoils, where transition forced separated flow to reattach even at low *Re*. The L1A was considered to be a good airfoil for future flow control work, combining very high loading (17% higher than the Pack B airfoil) with a need for separation control.

Along with experimental work significant computational effort has been devoted to better understanding of separation and transition mechanisms in the LPT.

Singh (2005) studied the flow physics in a LPT cascade under low Re number conditions using Large Eddy Simulation (LES). Calculations were carried out for *Re* = 10,000 and 25,000 (based on inlet velocity and axial chord). The flow for both Reynolds numbers separated and never reattached.

Gross and Fasel (2008) used coarse grid direct numerical simulations (DNS), implicit large eddy simulations (ILES) and unsteady Reynolds averaged Navier-Stokes (URANS) models to predict Pack B airfoil flows. The DNS and ILES results agreed when the computational grid was sufficiently fine, and some of the URANS models agreed as well. Agreement with experimental data was good in some instances, but significant differences were observed in others. This was attributed to possible differences between the inlet flow conditions in the experiment and computations.

DNS and LES calculation require high resolution grids, which results in high computational time, therefore these methods are very computationally expensive. This makes modification of Reynolds Averaged Navier-Stokes (RANS) methods for the purpose of better prediction of separation and transition processes very attractive. Many studies have been done in the area of developing and testing transition models capable of accurate prediction of flow physics in turbomachinery. Some of the latest examples include Howell (1999) who used the Prescribed Unsteady Intermittency Model (PUIM) to study wake - surface flow interactions on a high lift LPT airfoil. This approach employs a set of correlations for transition onset and for spot production rate. Suzen et al., (2003) applied a transition model based on an intermittency transport equation to predictions of LPT experiments on the Pack B airfoil. A different approach was proposed by Menter et al., (2006) based on two transport equations. The intermittency transport equation was used to trigger the transition onset. The transport equation for the transition momentum thickness Reynolds number ($Re_{\theta t}$) was used to capture non-local effect of freestream turbulence intensity and pressure gradient at the boundary layer edge. These two equations were coupled with a shear stress transport turbulence model (SST). This model was validated against experimental data for various turbomachinery and aerodynamic applications (Langtry et al., (2006) and Menter et al., (2006)).

In the present work a computational study of a very highly loaded low pressure turbine airfoil, designated L1A was conducted under low and high freestream turbulence conditions. The results are presented in section 4.4. The flow over L1A airfoil was extensively investigated utilizing different: 1) grid structures, 2) inlet velocity conditions, 3) turbulence models, and 4) Reynolds numbers.

4.1.2 Airfoil Flow Control

One of the ways to improve engine performance is to design airfoils with pressure gradients more resistant to separation, as described by Praisner and Clark (2007). Forward loading, for example, makes airfoils more separation resistant by extending the adverse pressure gradient on the aft portion of the suction side over a longer distance. This reduces the local pressure gradient at all locations, making separation less likely. If separation does occur, forward loading provides a longer distance along the airfoil surface for reattachment. Forward loading has some disadvantages, however. As noted by Zhang et al., (2007), the longer region of turbulent flow on a forward loaded airfoil can lead to increased pressure losses. Forward loading also creates longer regions of strong pressure gradient on the endwalls, which can produce stronger secondary flows and losses. If flow control is incorporated in the design of an advanced airfoil, as discussed by Bons et al., (2005) it might be possible to produce an aft loaded airfoil that is resistant to separation and has low pressure loss characteristics over a range of Reynolds numbers.

Separation control with passive devices such as boundary layer trips has shown to be effective by Volino (2003), Bohl and Volino (2006), Zhang et al., (2007) and others. Passive devices have the distinct advantage of simplicity, but they also introduce parasitic losses. Devices which are large enough to control separation at the lowest Reynolds numbers in an engine's operating range would tend to produce higher than necessary losses at higher Reynolds numbers. Active devices could potentially provide better control over the entire operating range of interest and be reduced in strength or turned off to avoid unnecessary losses when they are not needed.

The literature contains many examples of active separation control. A few which could be applied in turbomachinery are discussed in Volino (2003). Plasma devices, as used by Huang et al., (2003), could be viable, and are under active study. Vortex generator jets (VGJs), as introduced by Johnston and Nishi (1990), are another alternative, and will be the subject of the present study. Blowing from small, compound angled holes is used to create streamwise vortices. The vortices bring high momentum fluid into the near wall region, which can help to control separation. The most effective VGJs enter the boundary layer at a relatively shallow pitch angle (typically 30 to 45 degrees) relative to the wall and a high skew angle (45 to 90 degrees) relative to the main flow. Additionally, the jets promote transition, and turbulent mixing, which also helps to mitigate separation. Bons et al., (2002) noted that in the case of pulsed VGJs, the turbulence effect was more significant than the action of the vortices. Bons et al., (2002), Volino (2003), McQuilling and Jacob (2004), Eldredge and Bons (2004), and Volino and Bohl (2005), all used VGJs on the highly loaded Pack B LPT airfoil. In these studies separation was essentially eliminated, even at the lowest Reynolds number considered, (*Re*=25,000 based on suction surface length and nominal exit velocity). Pulsed jets were found to be more effective than steady jets. The initial disturbance created by each pulse caused the boundary layer to attach. The turbulence was followed by a calmed period (Gostelow et al., (1997) and Schulte and Hodson (1998)) during which the boundary layer was very resistant to separation, much like a turbulent boundary layer, but very laminar-like in terms of its fluctuation levels and low losses. When the time between pulses was long enough, the boundary layer did eventually relax to a separated state. However, due to the control which persisted during the calmed period, the VGJs were effective even with low jet pulsing frequencies, duty cycles and mass flow rates. Since the boundary layer was attached and undisturbed for much of the jet pulsing cycle, pressure losses were low.

Similar results with pulsed VGJs were found on the L1M airfoil by Bons et al., (2008). The L1M is more highly loaded than the Pack B, but more resistant to separation because of forward loading. A large separation bubble followed by boundary layer reattachment was observed at low Reynolds numbers, and pulsed VGJs reduced the size of the bubble.

Along with experimental investigations, numerical simulations of the flow over LPT blades, utilizing steady and pulsed vortex generator jets (VGJs) were performed by a number of researchers. This type of the flow is challenging for CFD because of its transitional nature in combination with highly three dimensional flow around the jets.

Garg (2002) used NASA Glenn-HT code with SKW-sst model of Menter (1994) to compute the flow over Pack B blade with and without use of VGJs. This work resulted in correct predictions of the separation location in the baseline case (without VGJs) as well as showed that separation vanishes in the flow control case as in experiment. However, the separated region and the wake were not well predicted, which is common for RANS.

Rizzetta and Visbal (2005) used Implicit Large Eddy Simulation (ILES) to investigate the effect of flow control by pulsed VGJs on the flow separation over the Pack B cascade. They reported that for inlet Re = 25,000 and B=2 flow control helped to keep flow attached for an additional 15% of the chord. Although CFD flow field, in their work, considerably differed from experimental, numerical and experimental time-mean velocity profiles were in a reasonable agreement.

L1A airfoil, considered in the present study, is an aft loaded blade with the same flow angles and loading as the L1M. Based on the design calculations of Clark (2007), the L1A has 10% higher loading than the “ultra-high lift” airfoils described by Zhang and Hodson (2005), and 17% higher loading than the Pack B. Because the L1A is aft loaded, it is more prone to separation than the L1M, as documented in Bons et al., (2008), Ibrahim et al., (2008), and Volino et al., (2008). In cases without flow control and with low freestream turbulence, the boundary layer separates when *Re*<150,000 and does not reattach, in spite of transition to turbulence in the shear layer over the separation bubble in all cases. This result contrasts with the results of earlier studies on less aggressive airfoils, which all showed reattachment after transition. The separation bubble on the L1A is about four times thicker than that on the Pack-B airfoil. The larger distance from the shear layer to the wall on the L1A apparently prevents the turbulent mixing in the shear layer from reaching the wall and causing reattachment. The failure of the boundary layer to reattach results in a 20% loss in lift and increases pressure losses by a factor of 7.

At higher Reynolds numbers the separation bubble is small and the boundary layer is attached over most of the airfoil. In cases with high freestream turbulence, results are similar, but the shear layer is somewhat thicker and the separation bubble thinner due to increased mixing induced in the shear layer. This results in reattachment after transition at *Re*=50,000 and 100,000. At the lowest *Re* considered (25,000) the boundary layer still does not reattach.

Fluent commercial code is used in the present study to investigate how the VGJ's performance, both steady and pulsed, is affected by varying pulsation frequency and blowing ratio for exit Re = 25,000; 50,000 and 100,000. The CFD results are compared with the experimental data for the pressure distributions along the airfoil surface, velocity measurements in the suction side boundary layer and pressure losses. The effects of the steady jets are discussed in section 4.5. The results of the pulsed jet flow control are presented in section 4.6.

4.2 Experimental Facility and Measurements Conducted at US Naval Academy

Experiments were conducted by Dr. Ralph Volino at US Naval Academy and described in details in Volino (2008). Experimental setup and boundary conditions are discussed in this section since they were used as a foundation for the computational model development.

A closed loop wind tunnel with a linear cascade in one corner of the loop was considered. A seven blade cascade is located in the wind tunnel's third turn, and it is shown in Fig. 4.1. A generic airfoil shape is shown in the figure. The freestream turbulence entering the cascade was measured with a cross-wire probe positioned just upstream of the center blade. In Low Freestream Turbulence Intensity (LFSTI) cases the streamwise velocity component had turbulence intensity, *TI*, of 0.8% and integral length scale of 6.3 cm. For the High Freestream Turbulence Intensity (HFSTI) cases the grid produced uniform flow with a *TI*, of 6.0% in the streamwise component in a plane perpendicular to the inlet flow and 1.7 C_x upstream of the center blade. The streamwise component was also measured at the inlet plane of the cascade, near the center blade, where it had decayed to 4% (the average value for the *TI* of 5% will be used as a boundary condition in HFSTI cases in CFD). The integral length scale of the freestream turbulence is 1.6 cm in the streamwise direction.

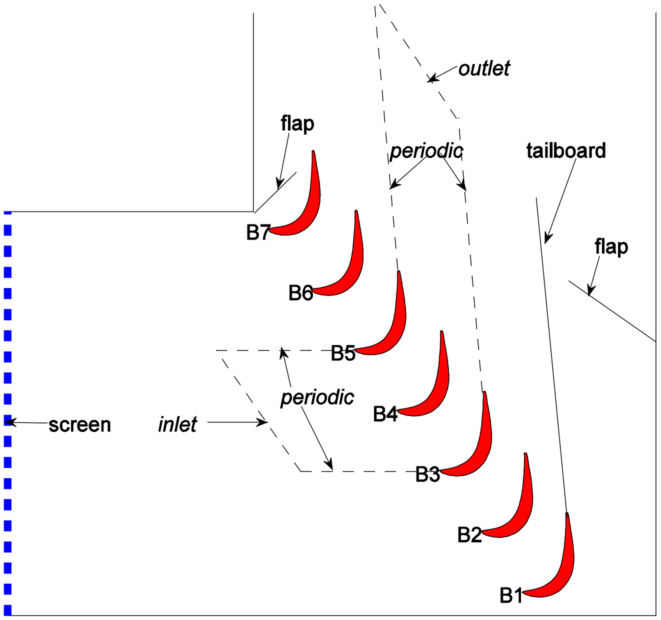

Figure 4.1: Schematic of a linear cascade of 7 airfoils (Volino (2008)) with boundary conditions and computational domain used in baseline study (without VGJs), shown in dashed lines

These values were used in all the calculations as inlet boundary conditions for turbulence. The low freestream turbulence and large length scales tested are not representative of engine conditions, however, they are still of an interest as a limiting case. Also, in zero or favorable pressure gradient boundary layers, high turbulence levels can cause bypass transition, but under adverse pressure gradients, natural transition appears to play a role at all turbulence levels.

A tailboard, shown in Fig. 4.1, was needed to produce the correct exit flow angle from the cascade. Its position was set to produce periodicity (the same flow characteristics for each blade in a cascade) at high Reynolds numbers. A tailboard on the opposite side of the cascade, and inlet guide vanes were found to be unnecessary. To produce the correct approach flow to the end blades (B1 and B7), the amount of flow escaping around the two ends of the cascade was controlled with the flaps shown in Fig. 4.1. The flap positions were set using a wool tuft upstream of each blade to check that the incoming flow approached the stagnation points with the correct angle. The inlet flow angle at the center of the cascade was also checked with a three-hole pressure probe and found to agree with the design angle to within about 2° of uncertainty. At high Reynolds numbers, the approach velocity to the middle four passages was measured to be uniform to within 6% and the difference between any two adjacent passages was within 3%. At low Reynolds numbers, slightly more variation was observed, but the approach velocity to the middle two passages still agreed to within 5%. Good periodicity at high Reynolds numbers was also observed in the exit flow from the cascade. At low Reynolds numbers, when significant separation bubbles were present, the periodicity was not as good due to suppression of the separation bubble thickness on the blades closest to the tailboard. This deviation from periodicity is considered acceptable for the present facility, since its intended purpose is for the study of flow control, which if successful should suppress separation on all blades, thereby restoring periodicity even at low Reynolds numbers.

Experiments for the flow control study were conducted in the same closed loop wind tunnel with a seven-blade linear cascade located in the wind tunnel's third turn, as shown in Fig. 4.1. Each blade in the cascade has a central cavity which extends along the entire span (see Fig. 4.2).

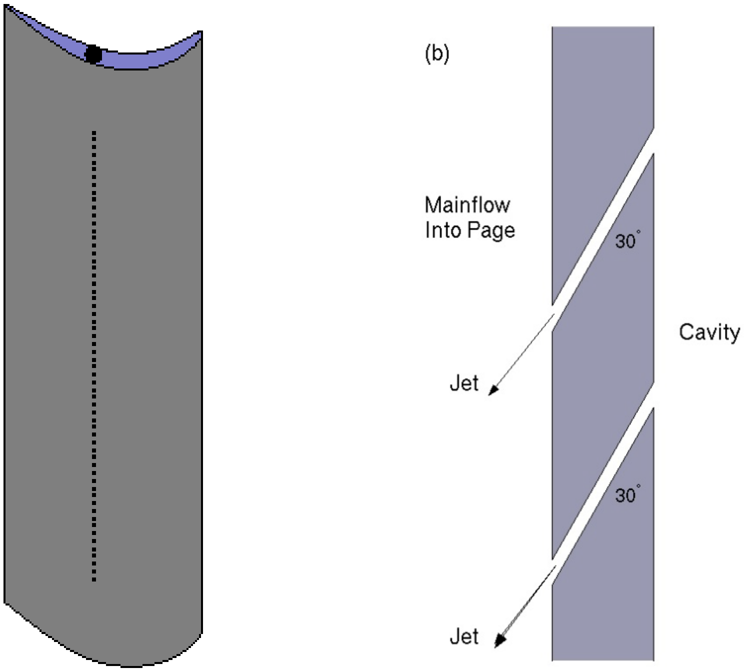

Figure 4.2: Airfoil with VGJ holes and cross section of the jet geometry

The cavity is closed at one end and has a fitting at the opposite end connected to a compressed air line. Air is supplied to the cavities from a common manifold. Manual ball valves are placed in the tubing between the manifold and blades to insure that each blade receives the same air flow. The valves also help to damp high frequency oscillations in the jet velocity when the VGJs are pulsed. The manifold is supplied through two fast response solenoid valves (Parker Hannifin 009-0339-900 with General Valve Iota One pulse driver) operating in parallel. The valves are supplied through a pressure regulator by the building air supply. A single spanwise row of holes was drilled into the suction surface of each blade at the inviscid pressure minimum location, s/L_s=0.5 (x/C_x=0.62), where s is the distance from the leading edge and L_s is the suction surface length. The pressure minimum has been shown in the studies listed in section 4.1.2 to be about the optimal location for flow control devices. The effects of devices located farther upstream are damped by the favorable pressure gradient, and devices located downstream of the separation point can also lose effectiveness. The holes are 0.8 mm in diameter and drilled at 30° to the surface and 90° to the main flow direction. This is the same orientation used in all the VGJ studies listed in section 4.1.2. The hole spacing is 10.6 diameters, and the length to diameter ratio is 12.

The solenoid valves pulse the VGJs, and the pulsing frequency is presented below in dimensionless form as:

$$F=fL_{j\text{-}te}/U_{ave},$$

where $L_{j\text{-}te}$ is the streamwise distance from the VGJ holes to the trailing edge, and U_{ave} is the average freestream velocity over this distance.

For the flow over single airfoil, $F \geq 1$ is typically needed to maintain separation control, but for cascades, Bons et al., (2002) showed that control is possible in some cases with $F = 0.1$. As shown in Volino (2003) and Bons et al., (2002), this is due to the extended calmed region which follows the jet disturbance. In practice, VGJs could be timed to wake passing in an LPT, which has a typical frequency of about $F = 0.3$.

The center blade, designated B4 in Fig. 4.1, contains pressure taps near the spanwise centerline. Pressure surveys are made using a pressure transducer (0-870 Pa range Validyne transducer). Stagnation pressure is measured with a pitot tube upstream of the cascade. The uncertainty in the suction side pressure coefficients is 0.07. Most of this uncertainty is due to bias error. Stochastic error is minimized by averaging pressure transducer readings over a 10 second period.

Total pressure losses are documented using a Kiel probe traversed across three blade spacings, 0.63 C_x downstream of the cascade. A traverse is located in the wind tunnel downstream of the cascade to move the probe. The traverse causes an acceptably low blockage when it is located at least two C_x downstream of the cascade.

Pressure and loss surveys were acquired at nominal Re=25,000, 50,000, 100,000. The Reynolds number is based on the suction surface length and the nominal cascade exit velocity. The corresponding Reynolds numbers based on the cascade inlet velocity and the axial chord length are 10,000, 20,000 and 40,000 respectively.

4.3 Computational model

The CFD predictions were performed with the numerical software tool ANSYS Fluent. Computational model, including grid, boundary conditions and turbulence model was first developed and validated against experimental data for the baseline cases (without VGJs). Then the model was modified in order to predict flow control over an airfoil. Eventually, pulsed jet boundary conditions were applied through User Defined Function (UDF) in ANSYS Fluent. All modifications in the original model were validated against experimental data. The details of the computational model are presented below.

The computational domain, used for the baseline studies without jets, consists of two channels and the airfoil in the middle; it is shown on Fig. 4.1 in dashed lines. The boundary conditions applied along the sides of the domain were periodic. Airfoil surfaces were modeled as walls, where no-slip boundary conditions were applied.

The inlet boundary condition was a prescribed uniform velocity. It is described in more detail below in section 4.3.2. The inlet into the two channels was located at 1.9 C_x upstream of the airfoil leading edge in the flow direction. Zero gage pressure was applied at the outlet. The exit was located at 3.8 C_x downstream of the airfoil trailing edge in the flow direction. Different exit locations were tested to insure that 3.8 C_x was far enough downstream to achieve independent results (as indicated by pressure coefficients, pressure losses downstream of the cascade and velocity profiles on the airfoil) through the passages.

Three different turbulence models were used to study separated flow on the highly loaded LPT airfoil without VGJs. Results were compared to the experimental results of Volino (2008b). These models are: the SKW-sst model of Menter (1994), the V2F model of Durbin (1995), and new Trans-sst model of Menter (2006) The unsteady Reynolds-averaged Navier-Stokes (URANS) equations were used as the transport equations for the mean flow. These models were described earlier in section 2.2.

Unsteady calculations were performed for all cases. Convergence was established when: 1) residuals reduced to a value of 10^{-4}, 2) monitored velocity at the outlet and pressure on the airfoil suction side settled around mean values and 3) the mass imbalance was less than 0.01 %. For cases without jets and with steady blowing jets after convergence was achieved within each time step (Δt = 0.0005 s) with the conditions listed above, time averaged results were obtained for 2000 time steps. For cases with the jet time step size was determined based on the cycle time (time from the beginning of the blowing till the beginning of the next blowing). Each cycle was divided into equal number of time steps (1000) and computation was continued until no variation cycle-to-cycle was reached. Time averaged results for these cases were obtained for 2 cycles.

4.3.1 Grid independence study

A grid independence study for 2D grids was conducted for *Re* = 100,000. The V2F turbulence model was applied. Three different grids were used, as shown in table 4.1. Main difference between grids 1 and 2 was that dimensionless distance from the airfoil walls (y^+) for grid 2 (0.6) was an order of magnitude smaller than for grid 3 (8.0). Difference in size between grids 1 and 2 is not significant since both grids have the same number of points on the airfoils surfaces, but grid 2 has more uniformly distributed nodes. Grid 3 has the same value of y^+ as grid 2, but it is much finer and has more nodes on the airfoils surfaces. Grids 2 and 3 showed maximum difference in C_p on the suction side of an airfoil less than 2%. Grid 2 was chosen for the study with no jets.

Table 4.1: Grid characteristics for grid independence study

Grid #	**Size**	**Max y^+ on the airfoil walls**	**Number of points on airfoil ss**	**Number of points on airfoil ps**
1	91516	8	290	240
2	62469	0.6	290	240
3	312393	0.6	1369	933

A separate grid study was conducted for 3D grids used for flow control predictions with LES. In this case further grid refinement was conducted for two reasons: a) to handle highly 3D jet flow and b) to utilize LES computation.

Three different grids were designed for this study as shown in Table 4.2, while Table 4.3 shows more specifications of grid 6.

To accurately represent structures in the near-wall region (for LES) recommended values are: y+~ 2; Δx+ ~ 50-150; Δz+ ~ 15-40 (see Piomelli and Chasnov, (1995)).

Table 4.2: Grids characteristics for the flow control study

Grid #	**Size (Cells)**	**Number of grids in z direction**	**y+**	**Δz+**	**Δx+**
4	1,500,000	15	0.5	12.6	1 – 100
5	5,900,000	30	0.5	6.3	0.4 – 52
6	11,900,000	54	0.5	0.4 - 3.5	0.4 – 52

Based on results for the pressure coefficient plotted versus dimensionless location on the suction side s/Ls on Fig. 4.3, grid 6 showed closest agreement with the data and therefore was chosen for further computation.

Table 4.3: Specifications of computational grid 6

Number of cells	11.9 millions
Number of nodes on the suction surface	768
Number of nodes on the pressure surface	392
Number of nodes in span direction	54
y+	<1
Δz+	0.4 - 3.5
Δx+	0.4 - 52
Distance from inlet boundary to the leading edge	3.8 C_x
Distance from the trailing edge to the outlet boundary	1.9 C_x

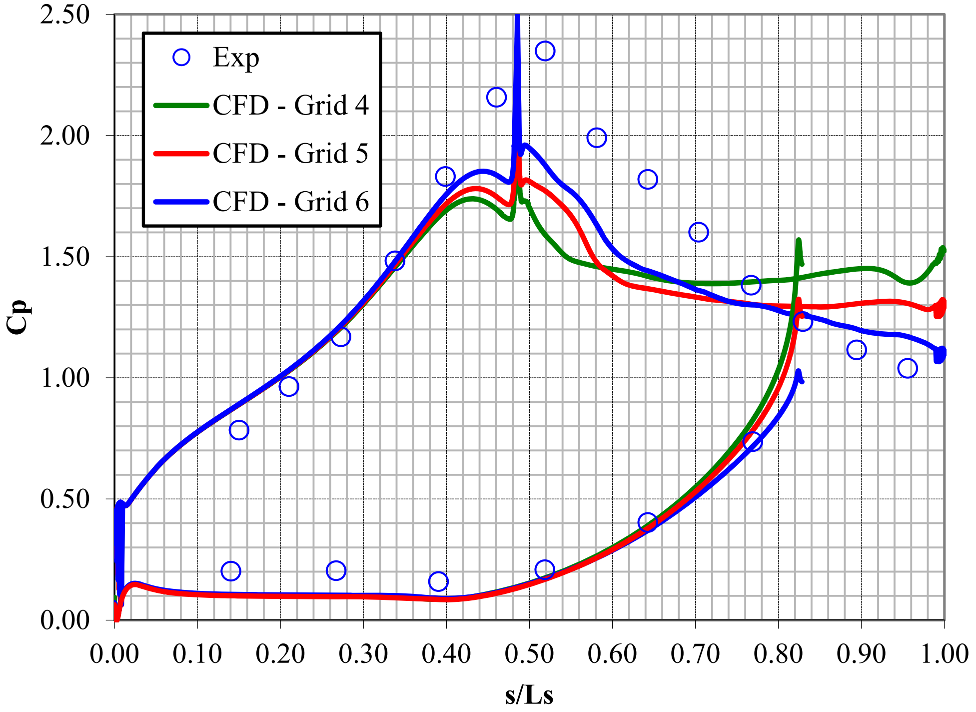

Figure 4.3: Grid Independence Study for the Flow Control cases (Re = 50,000, B=2, Steady Jets, dt = 0.0001 s)

General recommendations for selecting the time step size is that Δt should be small enough to resolve the time-scale of the smallest resolved eddies, such as (ANSYS Fluent Documentation (2009)): U Δt / Δx ~ 1 or less, where U Δt / Δx is the CFL number.

Grid 6 was run with different time steps (0.0005, 0.0001 and 0.00005 s) and time step of 0.0001 s was selected since no improvement was achieved using the smaller one (0.00005 s). In this case, based on freestream velocity and Δx in the separated region, CFL numbers for Δt = 0.0005, 0.0001 and 0.00005 s are equal to 9.30, 1.86 and 0.93 respectively. The results for the time step size effect study are shown on Fig. 4.4.

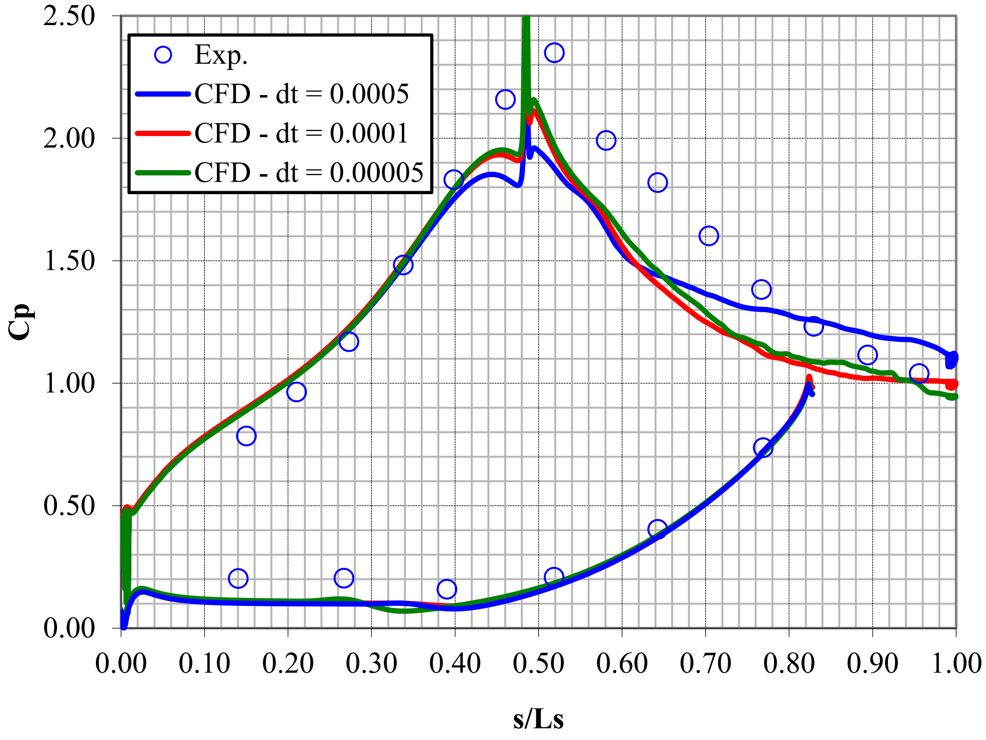

Figure 4.4: Time step size effect study for the Flow Control cases (Re = 50,000, B=2, Steady Jets, grid 6)

Fig. 4.5 shows the grid structure in the vicinity of the jet, near airfoil leading and trailing edges for grid 6.

4.3.2 Boundary conditions influence study

After grid independence was established several inlet velocity boundary conditions were tested in 2D. First, a uniform inlet velocity was applied in the direction of the design inlet flow angle (35°). This condition resulted in a slightly higher pressure on the leading section of the suction side of the airfoil compared to the experiment, indicating that the actual inlet angle could be different from the nominal design angle.

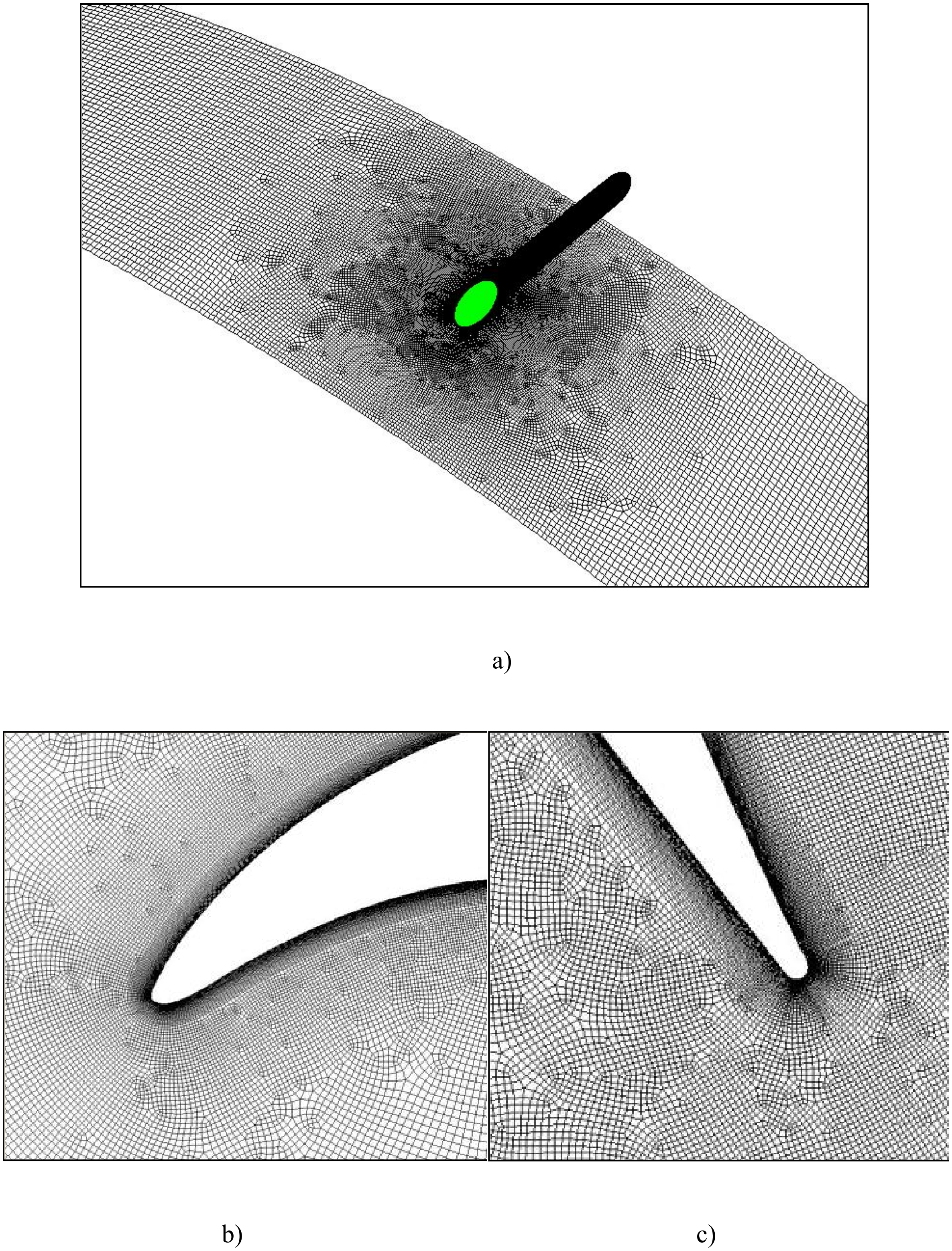

Figure 4.5: Three dimensional computational grid 6 a) in the jet vicinity, b) near leading edge of the airfoil, c) near trailing edge of the airfoil

To investigate this possibility further, a 2D inviscid calculation was done for the full cascade shown in Fig. 4.1, including the tailboard and flaps. The inlet velocity magnitude and direction were taken from the inviscid calculation along a line parallel to the blade row and 1.9 C_x upstream of the blades in the flow direction, and used to set the inlet boundary conditions to the 2 channel domain described above. The inlet boundary conditions tested at Re=100,000 are summarized in Table 4.4. Four different inlet conditions are presented in Table 4.4. The first condition assumed a uniform inlet velocity at the design flow angle of 35°. The second condition used the velocity profile entering the two channel domain as obtained from the invisicid calculation. This condition shows a slight variation in the velocity profile at the inlet both in x and y directions with spatially averaged velocities V_x= 3.78 m/s and V_y = 2.32 m/s, accordingly, the spatial averaged inlet flow angle is 31.5°. The third condition used a uniform inlet velocity and flow angle (V_x= 3.78 m/s and V_y = 2.32 m/s and inlet flow angle = 31.5°) based on the average values across the inlet of the two channel domain from the inviscid calculation. Thus, the difference between conditions (2) and (3) is in the spatial variation in the inlet velocity while the averaged values are the same. The fourth condition was a uniform inlet velocity and angle based on the spatial averaged values across the full cascade (instead of averaging over two channels only as in condition (3)) from the inviscid calculation. The inlet velocity variations chosen in this exercise involve different inlet flow velocity magnitude and angle based on the design or the inviscid CFD results for the 7 blades (see Fig. 4.1).

Table 4.4: Tested inlet boundary conditions at Re=100,000

#	Description	V_x, m/s	V_y, m/s	V_{mag}, m/s	α_1, deg
1	Design condition	3.65	2.56	4.46	35
2	Velocity profile from cascade simulation taken at the inlet into 2 channels	3.78 (avg)	2.32 (avg)	4.43 (avg)	31.5 (avg)
3	Velocity from cascade simulation averaged across inlet into 2 channels	3.78	2.32	4.43	31.5
4	Velocity from cascade simulation averaged across full cascade at streamwise location of inlet into 2 channels.	3.71	2.36	4.4	32.5

Boundary condition 4 produced results in a better agreement with the experimental data and was chosen for the rest of this investigation. The deviation of the inlet angle from the design angle in this case was about 2°, which is within the uncertainty of the experimental measurement.

The developed computational model with modifications for VGJs was used to study flow control. A single spanwise row of holes was modeled on the suction surface of the blade at the inviscid pressure minimum location, s/L_s=0.5 (x/C_x=0.62), where s is the distance from the leading edge and L_s is the suction surface length. The pressure minimum has been shown in the studies listed above to be about the optimal location for flow control devices. The effects of devices located farther upstream are damped by the favorable pressure gradient, and devices located downstream of the separation point can also lose effectiveness. The holes were 0.8 mm in diameter and at 30° to the surface and 90° to the main flow direction (see Fig. 4.2). The jets were spaced 10.6 diameters apart, and had the length to diameter ratio of 12.

The three dimensional computational domain was used in order to predict the flow control effects. A single channel with an airfoil in the middle was considered. The third dimension was necessary for modeling VGJs since compound angle was used.

Transition-sst model of Menter et al., (2006) and Large Eddy Simulation (LES) with dynamic subgrid-scale kinetic energy model of Kim and Menon (1997) were used for turbulence modeling. The full length of the jet tube was included in the simulations, allowing the jet velocity profile to develop before entering the main flow. The upstream plenum was not included in the calculations. The three dimensional grid results were compared to the results from a two dimensional grid for the baseline cases (without VGJs) and no significant differences were observed. The periodic boundary conditions in both pitchwise and spanwise directions were justified by performing calculations for a two channel domain and a domain with three VGJs in the spanwise direction. No significant difference between one channel and two channels domain and between one jet and three jets were observed for a pressure and velocity distributions along the airfoil. Therefore periodic boundary conditions were used at the top and the bottom of the channel and in the spanwise direction. The computational domain included one VGJ.

A uniform velocity boundary condition was specified at the jet’s inlet. For the pulsed jet cases, the inlet velocity was set as a square wave. For a duty cycle of 10% that means the jet is on only for 10% of the cycle and off for the rest of the cycle.

4.4 Separated flow predictions

In this section the effect of freestream turbulence on flow separation will be discussed. The results from the Low Free Stream Turbulence Intensity (LFSTI) runs are presented in sections 4.4.1 to 4.4.4. The effects of High Free Stream Turbulence Intensity (HFSTI) are discussed in section 4.4.5. Different flow regimes (Re = 25,000, 100,000 and 300,000) were studied in order to identify conditions where flow control would be beneficial. The results are presented in form of the pressure distribution on the airfoil surfaces and velocity profiles at six measurement stations along the airfoil suction side downstream of the suction peak. Pressure losses at the vertical location downstream of the cascade and locations of the separation and transition onsets are compared for all cases studied.

4.4.1 Pressure profiles

Figure 4.6 shows the pressure coefficient plotted versus s/L_s along the suction and pressure surfaces for three turbulence models tested (SKW-sst, Trans-sst and V2F) at Re = 25,000. The experimental data shows that the C_p values are a constant on the downstream half of the suction side. This plateau indicates that the boundary layer has separated and never reattached, creating a separation bubble. This of course refers to the time-averaged bubble. All turbulence models predict the pressure coefficient reasonably well with some deviation near the leading edge. The deviation could be partially attributed to uncertainty in the measurements and differences in the inlet velocity profile between calculations and experiment, as discussed in sections 4.2 and 4.3.2 respectively. All the models do well in predicting the size and location of separated region, as seen in the experiment.

Figure 4.7 shows the pressure coefficient plotted versus s/L_s along the suction and pressure surfaces for the turbulence models tested at Re = 100,000. All turbulence models predict the pressure coefficient very well except for the Trans-sst model, which shows under-prediction downstream from the suction peak. One possible explanation for this is that at s/L_s = 0.6 transition starts (as will be discussed in section 4.4.4) and mixing associated with transition will tend to promote reattachment. This would result in a drop in the pressure coefficient. The simulation may be over predicting this tendency toward reattachment in this case, although the velocity profiles shown below do not indicate reattachment.

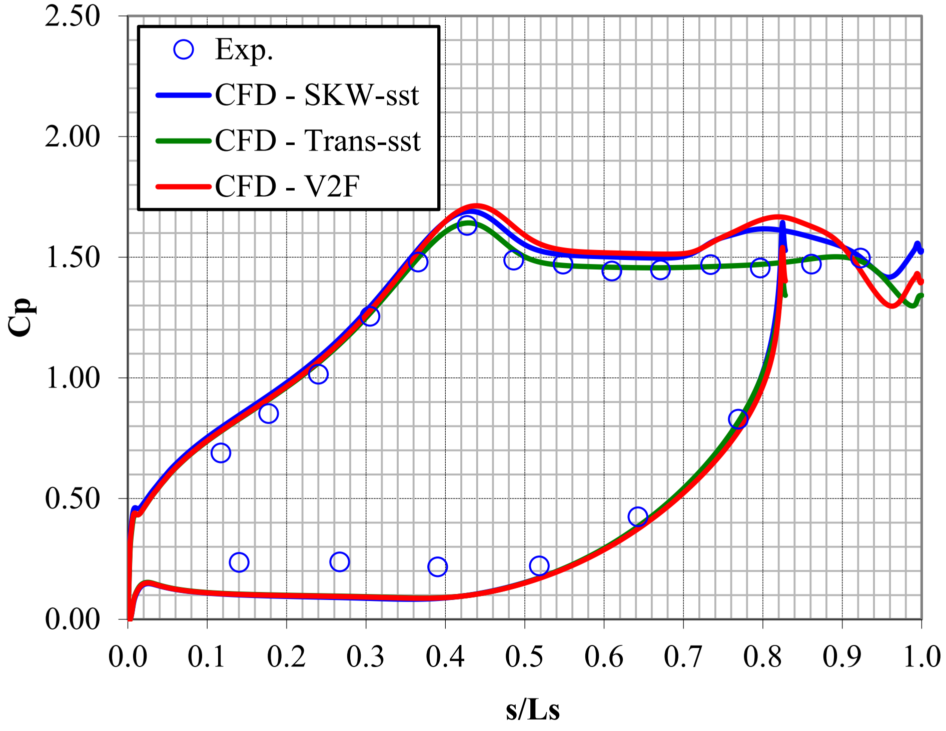

Figure 4.6: C_p profiles, *Re*=25,000

Figure 4.8 shows measured and computed pressure coefficients plotted versus s/L_s along the suction and pressure surfaces of the airfoil at *Re* = 300,000. The experimental data indicate that the boundary layer is attached over most of the airfoil.

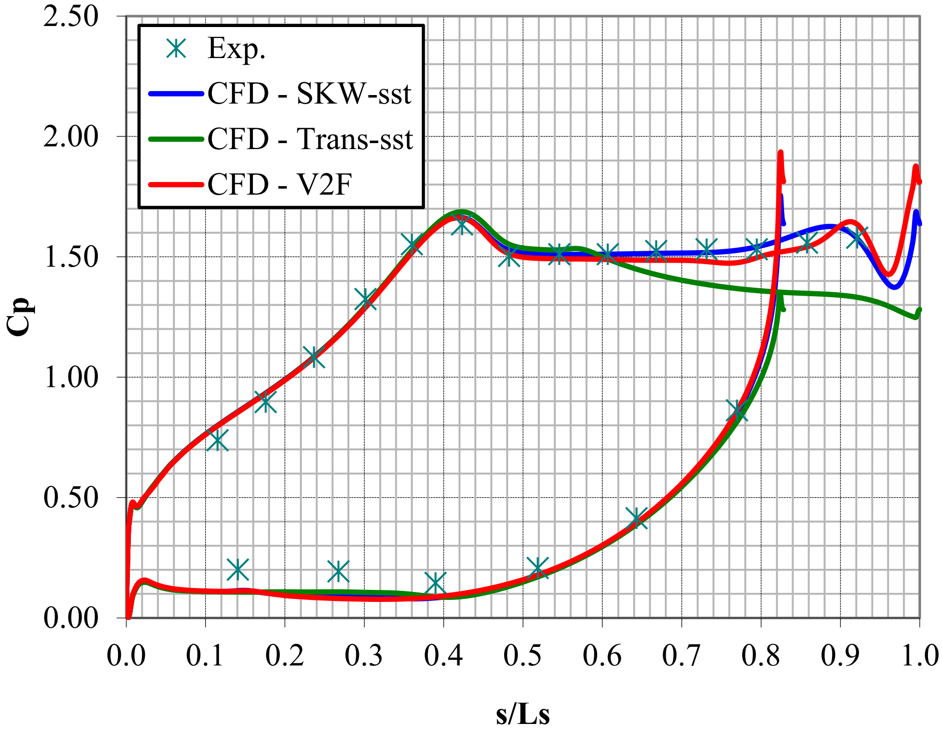

Figure 4.7: C_p profiles, *Re*=100,000

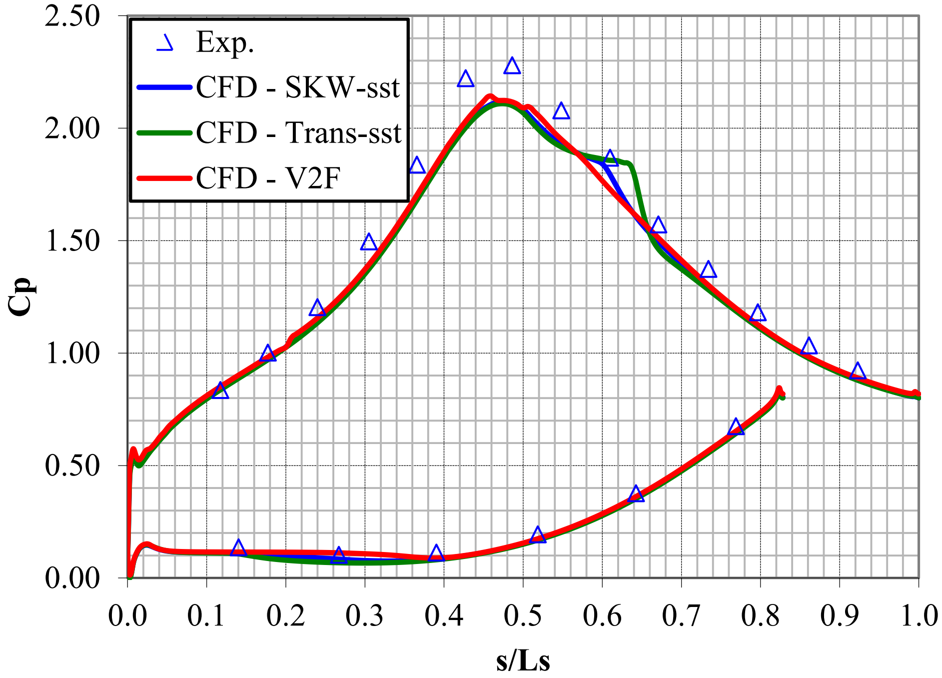

Figure 4.8: C_p profiles, *Re*=300,000

All turbulence models predict the pressure coefficient reasonably well including the area near the leading edge. The Trans-sst model shows a bump at $s/L_s = 0.6$ indicating a small bubble that appears and then closes quickly. Although not as clear in the data, the predicted bubble may be correct. The predicted location is between two pressure measurement locations in the experiment, so the presence of the bubble would not necessarily be visible in the data. Also, a small bubble at this location was clearly noticed in the experimental data at a lower *Re* (=200,000).

4.4.2 Total pressure losses

Figure 4.9 shows the total pressure loss coefficient ψ, plotted versus dimensionless distance (ϕ/L_ϕ) at a location 0.63 C_x downstream of the cascade for Re = 25,000 case. On this figure the middle peak in pressure loss coefficient corresponds to the location downstream of the blade 4 (see Figure 4.1), the peak to the right to it corresponds to the location downstream of the blade 5 and the one to the left to it corresponds to the location downstream of the blade 3. The definition of ψ used in this study is the same as the one used in earlier work by Volino (2008b) and Bons et al., (2008a). By that definition:

$$\psi = (P_T - P_{Te})/(P_T - P_S),$$

where P_T - upstream stagnation pressure, P_{Te} - downstream stagnation pressure, P_S - upstream static pressure.

The coordinate ϕ indicates the distance in the direction perpendicular to the axial chord. The normalizing quantity L_ϕ is the blade spacing (pitch). The origin, $\phi = 0$, corresponds to the location directly downstream of the trailing edge of the center blade (blade 4 on Fig. 4.1) in the direction of the exit design flow angle. At this low Reynolds number the large separation bubble results in high losses and forces the peaks about $0.35L_\phi$ toward the pressure side of each passage. The peaks become noticeably smaller moving from B5 to B3, indicating the effect of the tailboard in reducing the separation bubble thickness in experiment. Due to the lack of periodicity in the experiment, the predicted loss coefficient is not expected to agree closely with the experimental one. The prediction is based on periodic boundary conditions and is not influenced by tailboard effects, so it should show higher losses and possibly lower flow turning (peaks shifted more to the left in the figure). This is indeed the case, as shown in Fig. 4.9.

Figure 4.10 shows the total pressure loss coefficient plotted versus dimensionless distance at 0.63 C_x downstream of the cascade for Re = 100,000 case.

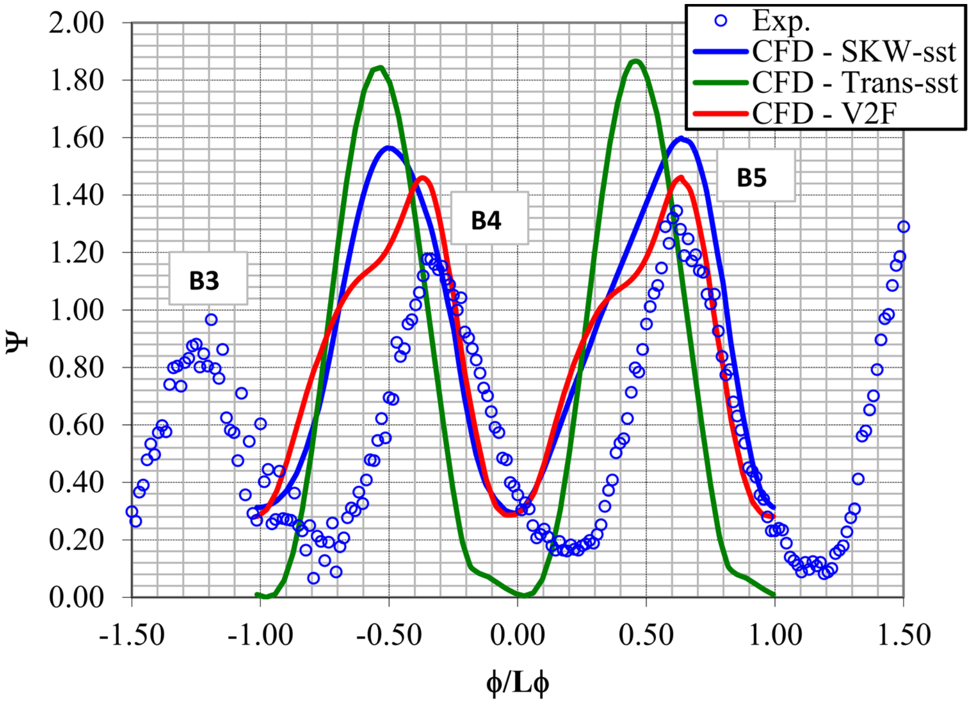

Figure 4.9: Pressure loss coefficients at 0.63 C_x downstream of the cascade, Re=25,000

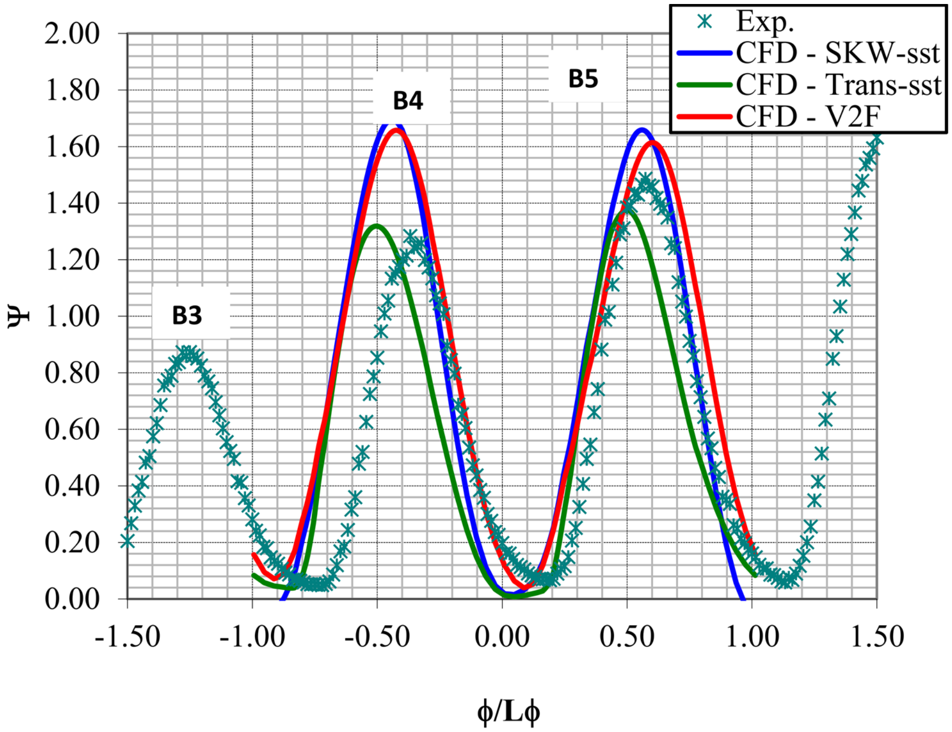

Figure 4.10: Pressure loss coefficients at 0.63 C_x downstream of the cascade, *Re*=100,000

The loss coefficient was predicted reasonably well by all models with the Trans-sst model showing the best agreement with experiment. As in the *Re* = 25,000 case, the experimental results were not periodic, so close agreement is not expected between the prediction and the data.

Figure 4.11 shows the total pressure loss coefficient plotted versus dimensionless distance at 0.63 C_x downstream of the cascade for Re = 300,000 case. The loss coefficient was predicted reasonably well by all models. The experimental data showed periodic results at this higher *Re*. Therefore the periodic boundary condition applied in the CFD is consistent with the experiment. Nevertheless, the magnitude of the pressure loss coefficient is over predicted by about 15%. The location of the peaks is also shifted to the right of the experimental peaks in Fig. 4.11. The amount of the shift corresponds to about a 4° difference in flow angle. Further investigation is required in order to determine the reason for this shift.

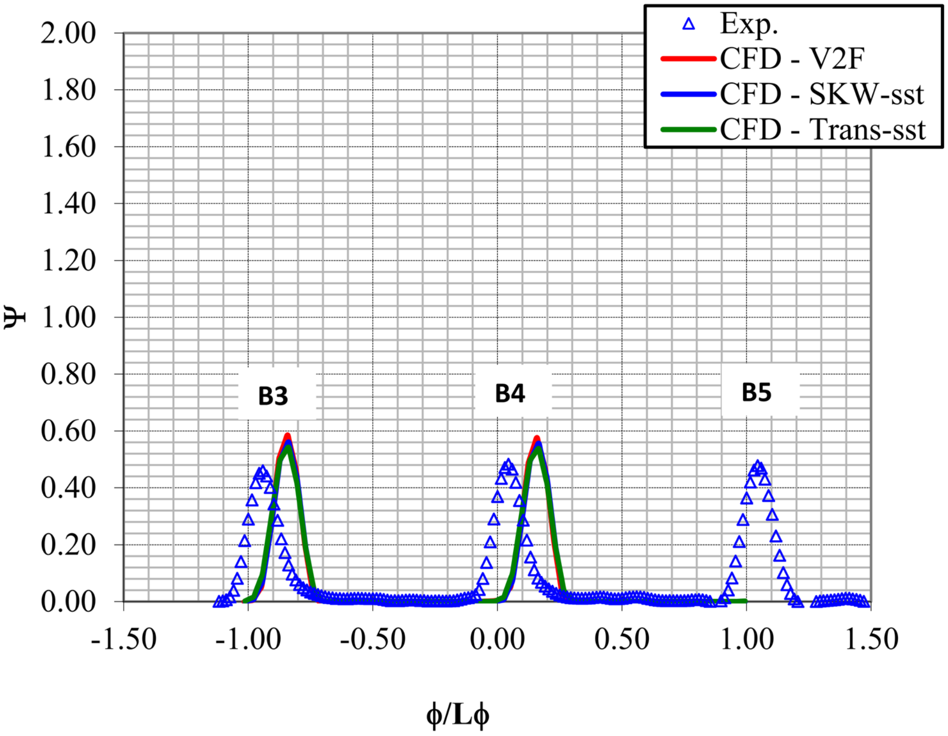

Figure 4.11: Pressure loss coefficients at 0.63 C_x downstream of the cascade, *Re*=300,000

4.4.3 Velocity profiles

Velocity profiles were acquired at 6 different stations downstream of the suction peak (see Table 4.5.). Comparison was made between the velocity profiles at these stations from CFD and experiments.

Table 4.5: Velocity profile measurement stations

Station	**1**	**2**	**3**	**4**	**5**	**6**
s/Ls	0.53	0.59	0.69	0.78	0.88	0.97
x/Cx	0.65	0.72	0.80	0.86	0.92	0.97

Velocity profiles for the six suction surface measurement stations on blade B4 documented in the experiment are shown in Fig. 4.12 for the nominal Re=25,000 case. The figure shows the distance from the wall normalized on the suction surface length plotted against the local mean velocity normalized on the nominal exit velocity, U_e. The boundary layer has just separated at the first measurement station and the separation bubble grows larger at the downstream stations.

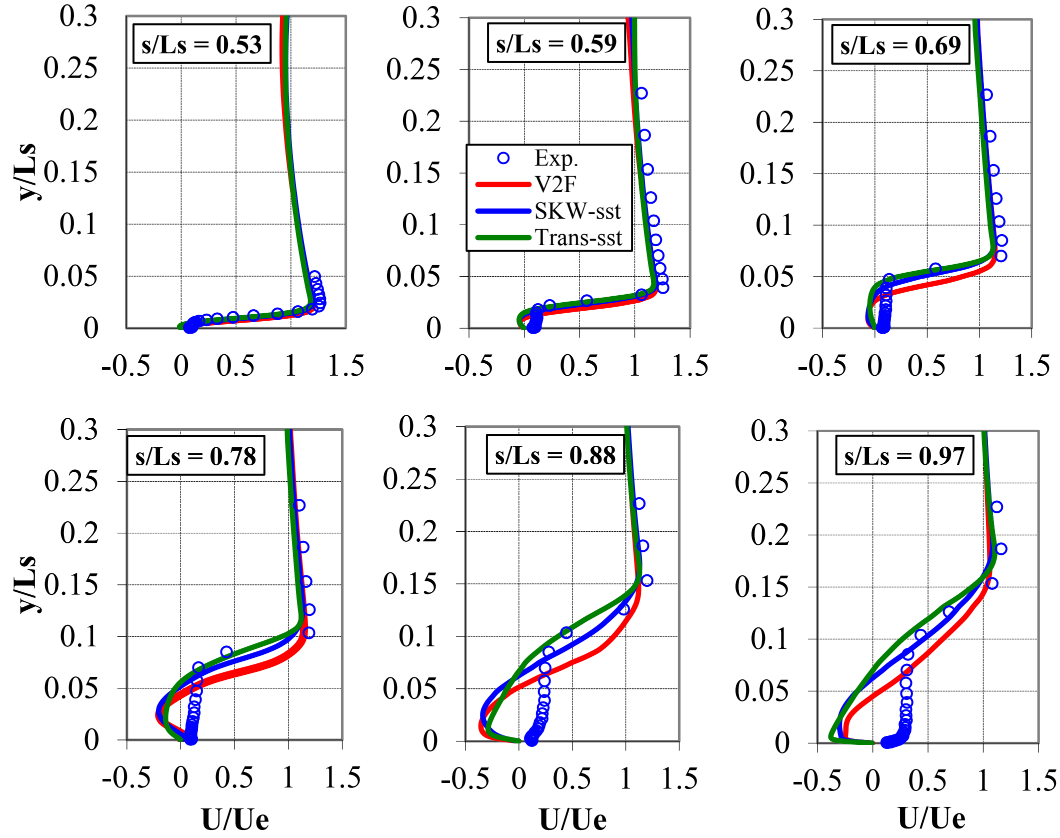

Figure 4.12: Mean velocity profiles, Re = 25,000

The boundary layer does not reattach. The velocity profiles at the six stations along the suction surface are predicted reasonably well by all models with the Trans-sst model doing better overall. The prediction in the near wall region is different than the data since the measurements were done using hot-wire anemometry and therefore cannot register negative velocities when separation occurs.

Figure 4.13 shows u'/U_e profile versus y/L_s at the six different stations along the suction side. Fluctuating streamwise velocity component (u') was obtained from CFD (using the Trans-sst model only because of its best overall performance) from the kinetic energy of turbulence and assuming an isotropic flow field (i.e. $u' = v' = w'$). Despite this assumption the CFD shows reasonable agreement with the data in the magnitude of u'/U_e and the location of maximum value. The CFD shows a peak in the u' profile that moves away from the wall as one travels from station (1) to (6). This peak value will be utilized (as will be shown later in section 4.4.4) to predict the start of transition.

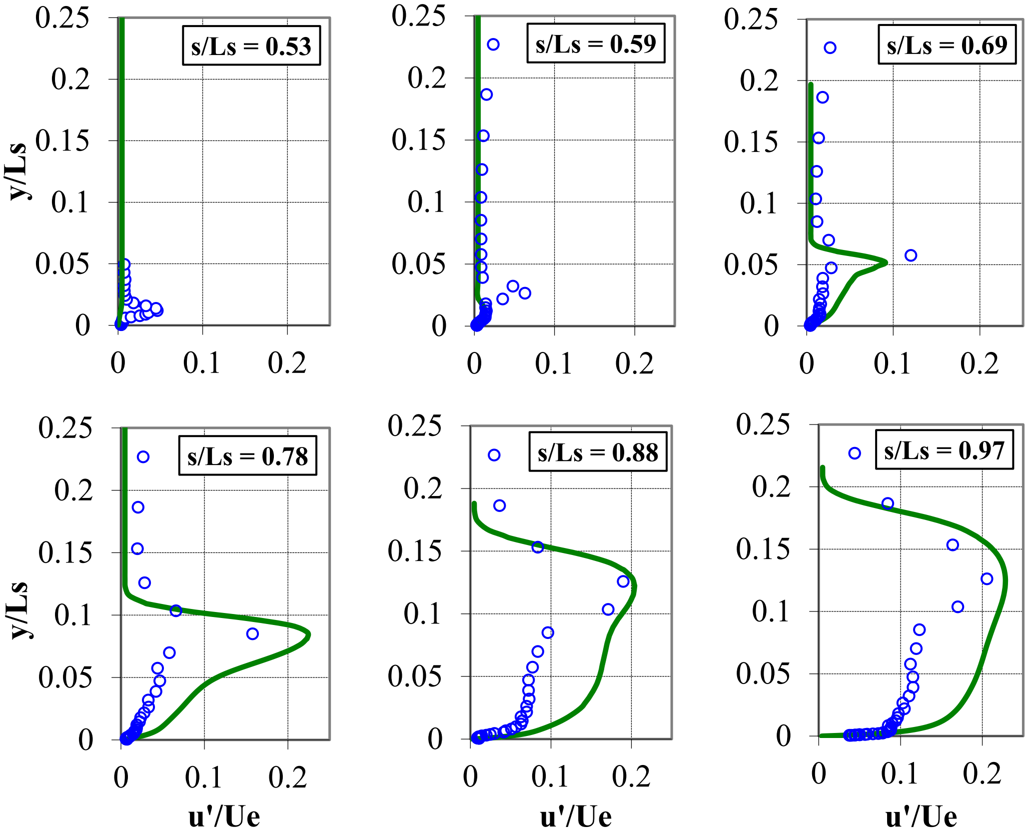

Figure 4.13: Comparison of Trans-sst and experimental u'/U_e profiles, Re= 25,000

Figure 4.14 shows the velocity profiles (normalized with respect to the exit free stream velocity) versus y/L_s at the 6 stations along the suction side for the Re = 100,000 case. The velocity profiles are predicted reasonably well by all models with the Trans-sst model doing better overall.

Figure 4.15 shows u'/U_e profiles versus y/L_s at 6 stations along the suction side for the same case (Re = 100,000). As explained above, u' was obtained from the CFD (using the Trans-sst model) using the kinetic energy of turbulence and assuming an isotropic flow field. The CFD results show a peak in the u' profile that moves away from the wall as one travels from station (1) to (6).

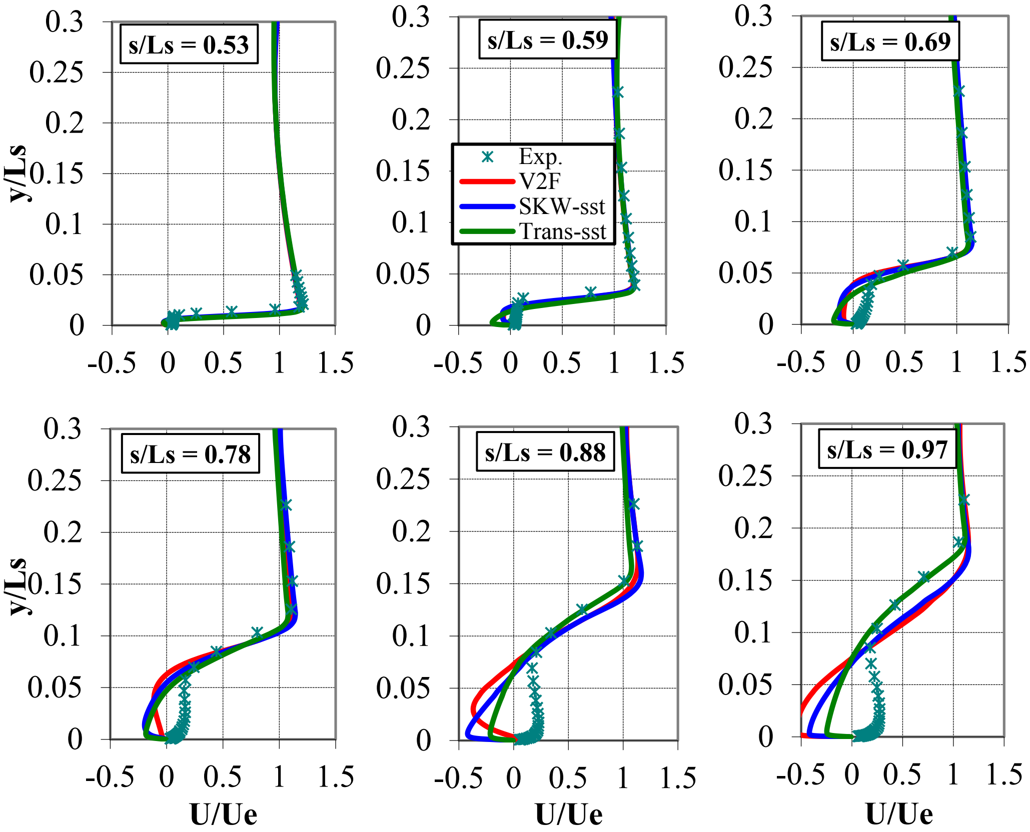

Figure 4.14: Mean velocity profiles, *Re* = 100,000

Similarly, from the experimental data, the separation bubble grows in the streamwise direction, the boundary layer does not reattach, and there is a very high peak in the fluctuating velocity in the shear layer over the separation bubble.

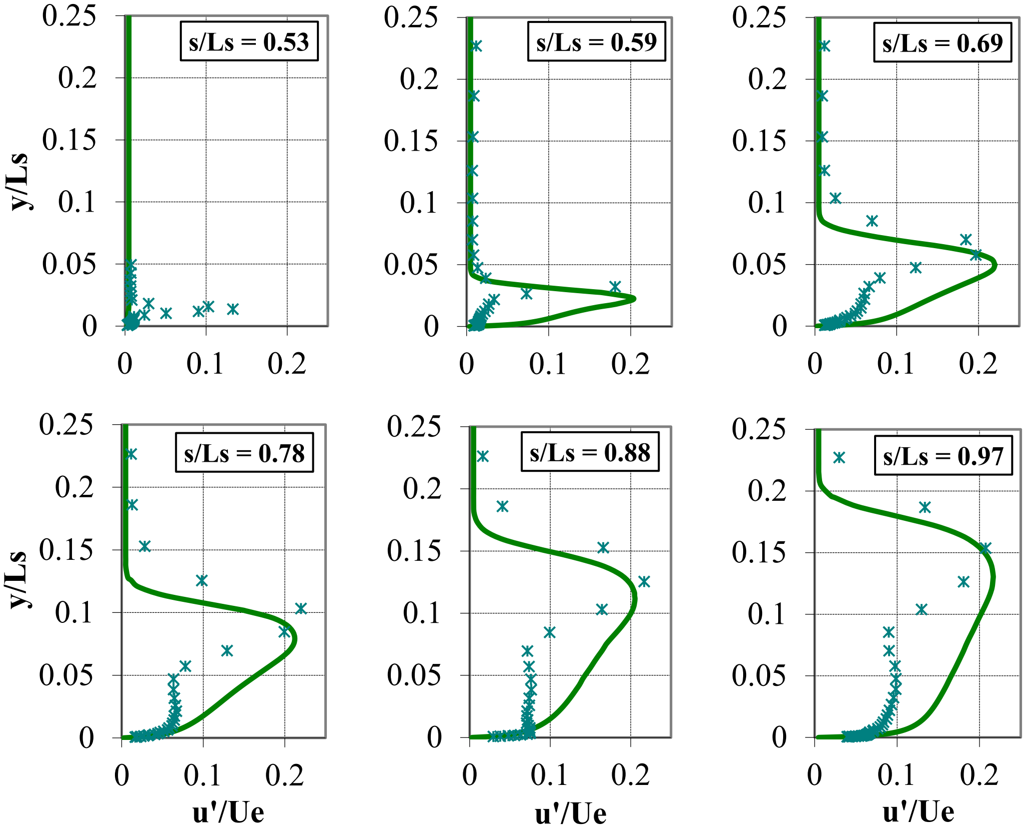

Figure 4.15: Comparison of Trans-sst and experimental u′/U$_e$ profiles, Re= 100,000

Figure 4.16 shows the velocity profile (normalized with respect to the exit free stream velocity) versus y/L_s at 6 stations along the suction side for Re = 300,000 case. The velocity profiles are predicted very well by all models. Figure 4.17 shows u'/U_e profiles versus y/L_s at the 6 stations along the suction side for the same case. The CFD shows good agreement with the data.

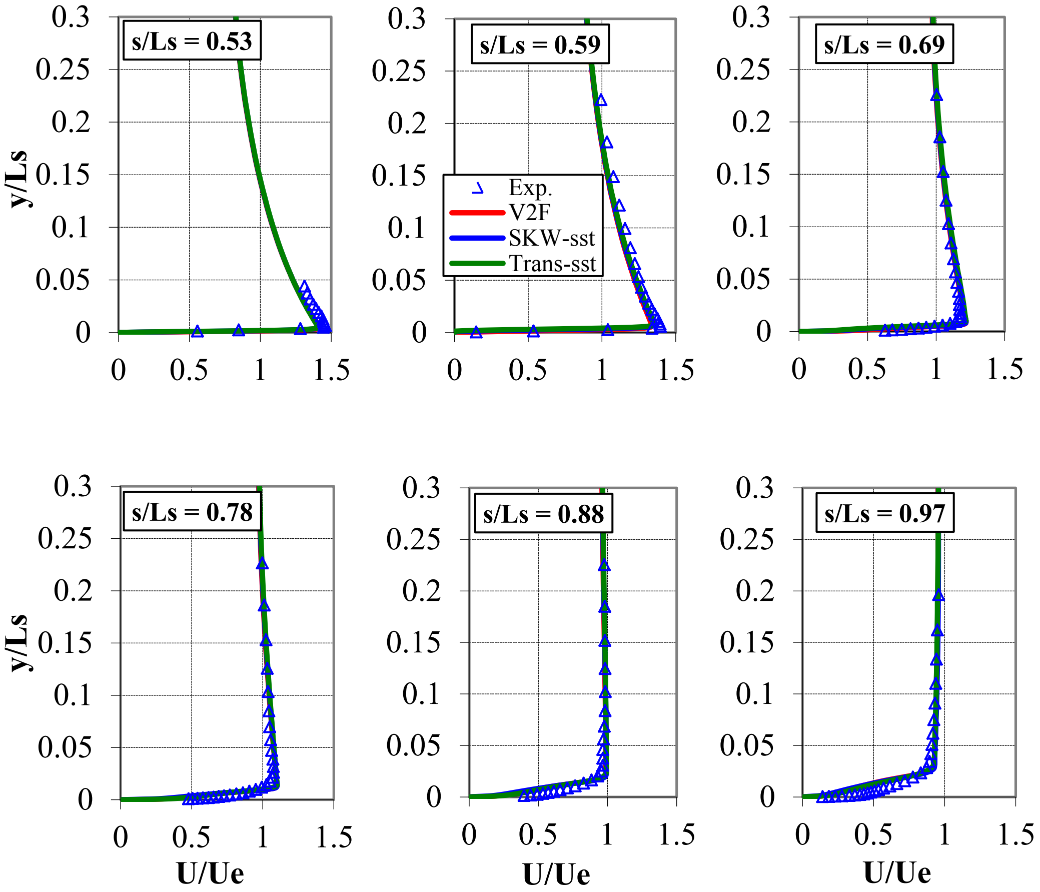

Figure 4.16: Mean velocity profiles, *Re* =300,000

4.4.4 Prediction of Transition

From the above investigation it was concluded that the Trans-sst model shows overall better agreement with the experimental data. Therefore this model was utilized to show how its predictions compare with the data for the locations of separation and the start of transition.

Figure 4.18 shows contours of u'/U_e over the suction side of the airfoil overlapped with velocity vectors at *Re*=25,000 (4.18a), *Re* =100,000 (4.18b) and *Re* = 300,000 (4.18c). On each plot the location of the: 1) suction peak, 2) six stations used earlier in the velocity comparison with the data, 3) separation point and 4) transition start are shown.

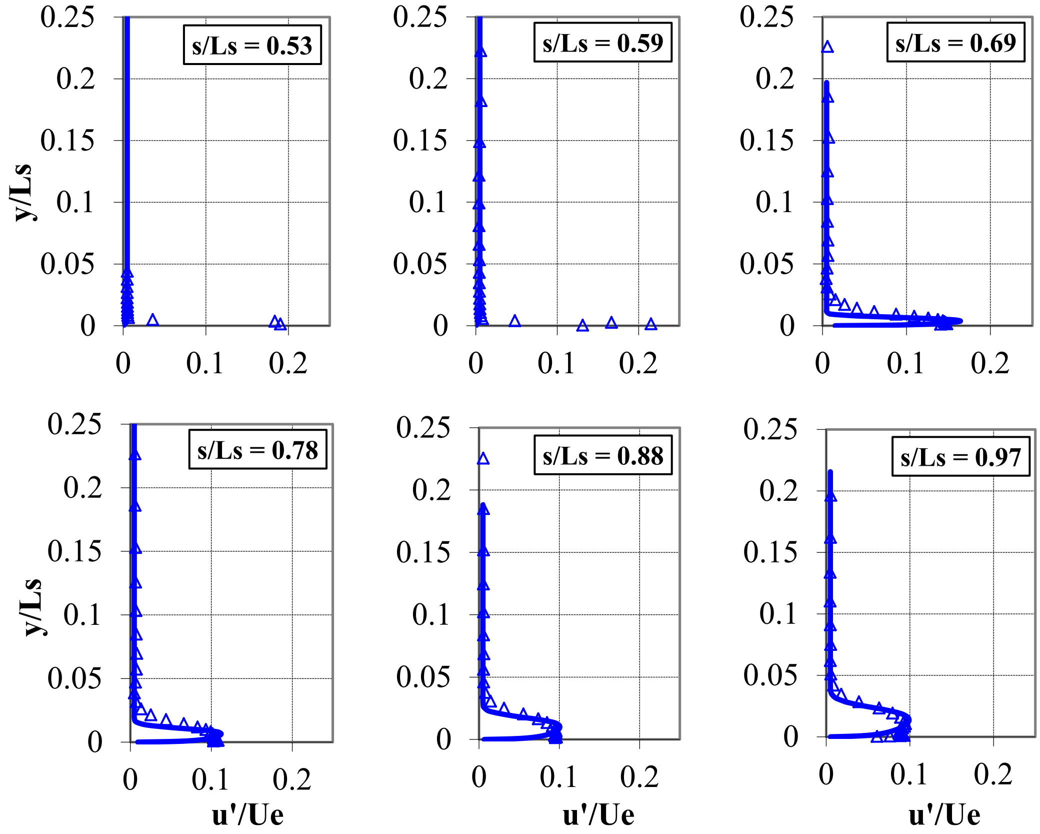

Figure 4.17: Comparison of Trans-sst and experimental u'/U_e profiles, Re= 300,000

The CFD results of Fig. 4.18a show that the flow separates (at station (1)) with no reattachment, as observed experimentally. The location of transition was taken as the location where u'/U_e peaks in the shear layer over the separation bubble (between station (3) and (4) and close to (4)). In Fig. 4.18b the CFD data show that the flow separates (at station (1)) with no reattachment as observed experimentally. Again the location of transition was obtained where u'/U_e peaks in the shear layer (between station (1) and (2)). Notice that the transition location moved upstream as *Re* increased compared to the *Re* = 25,000 case. In Fig. 4.18c the CFD data show that with the possible exception of a small bubble which appears at s/L_s = 0.6, the boundary layer is attached, which is consistent with the experimental data. The location of transition was obtained at the peak of u'/U_e between stations (2) and (3).

To quantify the results in Fig. 4.18, Table 4.6 shows the numerical values of the predicted momentum thickness Reynolds number at the suction peak ($Re_{\theta p}$), the Reynolds number based on the freestream velocity at the suction peak and the streamwise distance from the suction peak to transition (Re_{pt}). The streamwise locations of the suction peak, transition and separation are shown in Table 4.6 as well. Table 4.7 shows corresponding measured quantities from the experiment. Note that $Re_{\theta p}$ and s_s in Table 4.7 were approximated using a laminar boundary layer calculation as explained in Volino (2008b). The ranges given for Re_{pt} and s_t/L_s result from the finite spacing between measurement stations. The transition location (from CFD) is shown in Fig. 4.19 along with a correlation from Volino and Bohl (2004):

$$Re_{pt}=8.80\ [6.37 - \log_{10}(TI^2)]\ Re_{\theta p}^{4/3},$$

where TI – turbulence intensity. The agreement between the CFD and experiment shown in Tables 4.6 and 4.7 and on Fig. 4.19 is reasonably good.

Table 4.6: CFD results for separation and transition locations (Trans-sst model)

Re	**25,000**	**100,000**	**300,000**
$Re_{\theta p}$	45	87	165
Re_{pt}	11274	20816	73145
s_p/L_s	0.43	0.42	0.47
s_t/L_s	0.74	0.59	0.64
s_s/L_s	0.53	0.53	0.6

Table 4.7: Experimental Results for separation and transition locations

Re	**25,000**	**100,000**	**300,000**
$Re_{\theta p}$	48	96	193
Re_{pt}	12140 (+/-3300)	28340 (+/-6500)	71170 (+/-22600)
s_p/L_s	0.44	0.44	0.49
s_t/L_s	0.78 (+/-0.094)	0.64 (+/-0.047)	0.64 (+/-0.047)
s_s/L_s	0.50	0.50	0.54

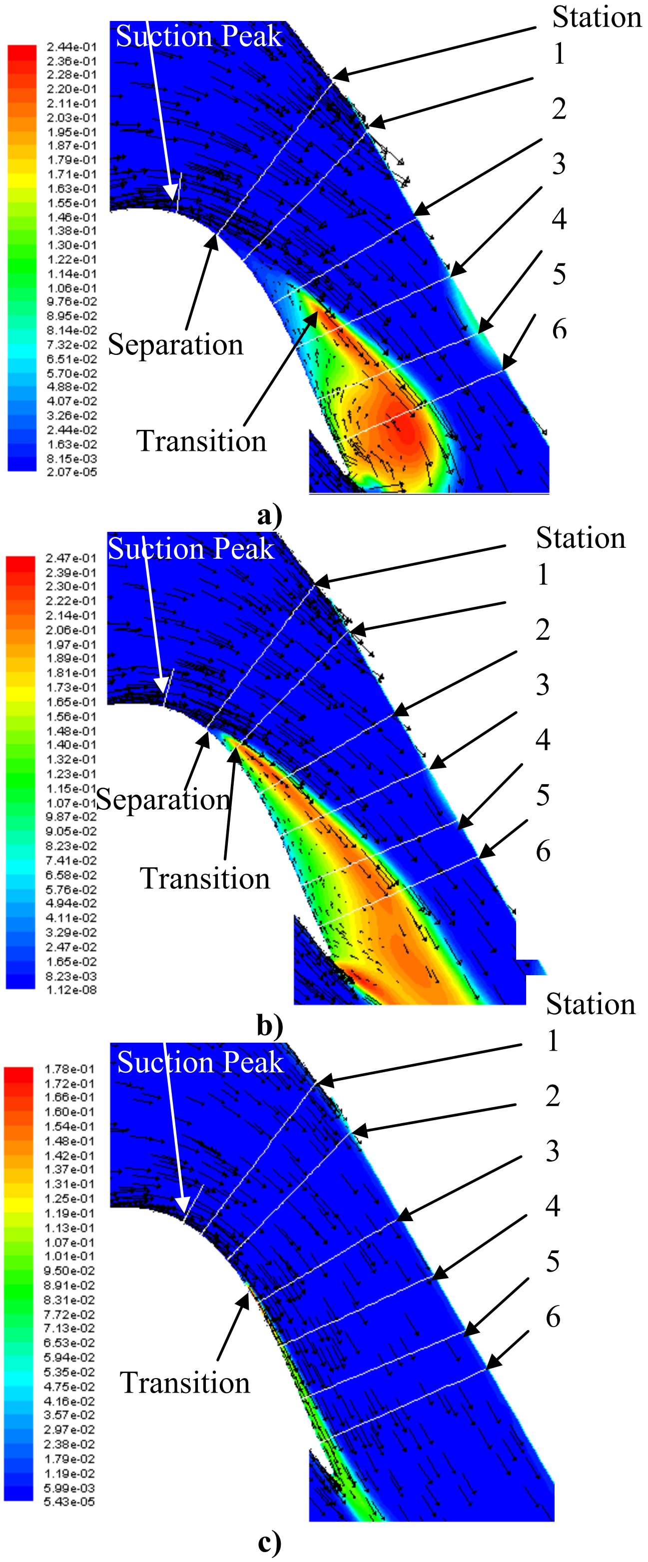

Figure 4.18: Contours of u′/U$_e$, and velocity vectors (for Trans-sst model) showing the location of: 1) suction peak, 2) separation and 3) transition for a) *Re* = 25,000, b) Re = 100,000, and c) Re = 300,000

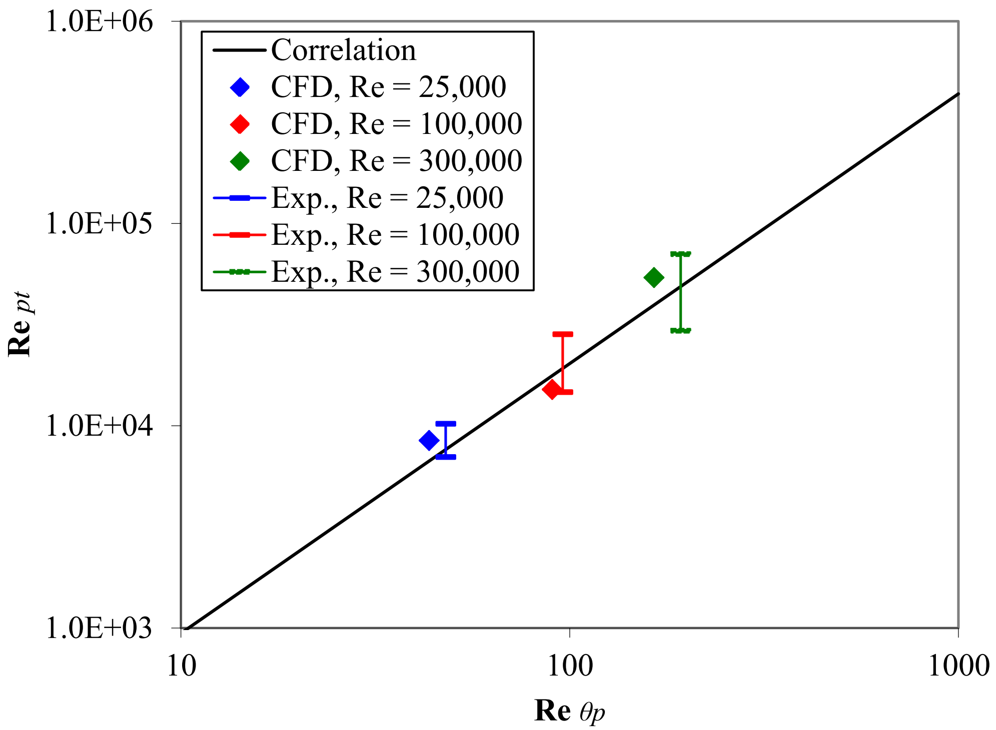

Figure 4.19: Comparison between CFD data (Trans-sst Model) and correlation for the start of transition

Computational study of the flow over the very high lift L1A airfoil based on experiment reported by Volino (2008b) was presented in sections 4.4.1 – 4.4.4. Reynolds numbers based on suction surface length and nominal exit velocity was ranging from 25,000 to 330,000. The experimental data showed that in all cases the laminar suction surface boundary layer separated, but at Reynolds numbers greater than 150,000 the separation bubble was very thin and short, and the boundary layer was attached over most of the surface. At lower Reynolds numbers the boundary layer separated and never reattached. Transition to turbulence occurred in all cases in the shear layer after separation. Transition caused immediate reattachment in the high Reynolds number cases, but the turbulent shear layer remained separated in the low *Re* cases.

Three different unsteady RANS turbulence models models were utilized in the present computational study. They are: the SKW-sst, V2F and the Trans-ss. At *Re*=25,000, the Trans-sst model seemed to perform the best. At *Re*=100,000 the Trans-sst model again had the best agreement with experiment with some under-prediction in the pressure coefficient downstream of the suction peak. At *Re*= 300,000 all models performed very similar with each other. The Trans-sst model showed a small bump in the pressure coefficient downstream from the suction peak indicating the presence of a small bubble at that location.

Upon comparing the pressure loss coefficient at 0.63 C_x downstream of the cascade, the CFD showed a shift toward the pressure side of the passage compared to the data. Further investigation of the cause of this shift is needed.

Reasonably good agreement was obtained upon comparing the start of transition as obtained from CFD (using the Trans-sst model), a published correlation and the experimental data.

In the following section the results from the HFSTI runs are presented.

4.4.5 Effects of free stream turbulence on separation

In order to examine effects of free stream turbulence on separation the freestream turbulence intensity was set to 5% (compared to 0.08% in LFSTI cases) to match the experimental value. Cases with elevated turbulence levels in the crossflow were ran for Re = 25,000, 100,000 and 300,000. The results from these runs in form of pressure coefficient, velocity profiles on the airfoil and pressure loss coefficient downstream of the cascade are presented in this section. Comparison between HFSTI and LFSTI cases is made.

Velocity vectors plotted on top of the contours of the turbulent kinetic energy from High Free Stream Turbulence Intensity (HFSTI) cases are shown in Fig. 4.20 from the simulation results using the Trans-sst model. As will be shown later in this section, the Trans-sst model generally performed better than the SKW-sst model. The flow along the suction side of the airfoil is shown in the figure. For reference, the white lines in the figure correspond to the experimental measurement stations listed in table 4.5. The short white line upstream of the others indicates the location of the suction peak. In agreement with the experimental results, the simulation predicts a large separation bubble at *Re*=25,000. The turbulence level is high in the shear layer above the separation bubble, but the boundary layer does not reattach. The velocity vectors show a significant reduction in flow turning. At Re=100,000 and 300,000, again in agreement with the experiment, the boundary layer is attached. The turbulence contours indicate a thicker boundary layer at Re=100,000 than at 300,000.

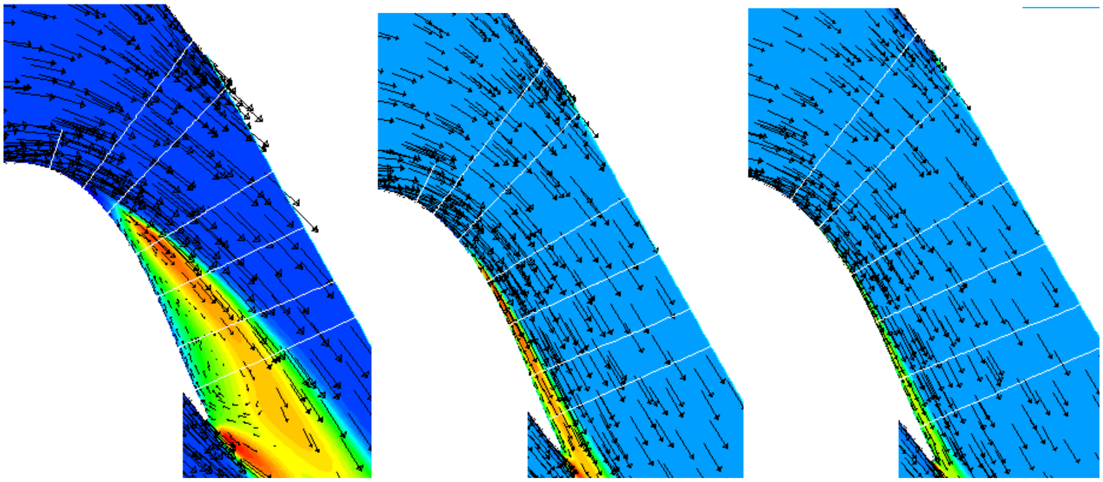
(a) **(b)** **(c)**

Figure 4.20: Flow field on suction side of airfoil showing turbulent kinetic energy (contours) and mean velocity (vectors) for HFSTI cases: a) *Re*=25,000, b) *Re*=100,000, c) *Re*=300,000

The location of the suction peaks and separation locations in fig. 4.20 agree with experimental ones (Volino (2008a)) to within 0.013 and 0.034 in value of s_p/L_s and s_s/L_s respectively.

To quantify the simulation results, pressure profiles for the numerical simulations are compared to the experimental results in Fig. 4.21. At all Reynolds numbers, both the SKW-sst and Trans-sst models agree reasonably well with the experimental data. At *Re*=25,000, the Trans-sst model agrees with the data to within the experimental uncertainty at the locations from s/L_s=0.1 to 0.6. The SKW-sst C_p prediction is slightly lower, but both models correctly predict that the boundary layer does not reattach. The Trans-sst model predicts a drop in C_p downstream of s/L_s=0.6 which is not seen in the data. The drop corresponds to the start of transition, as was discussed in section 4.4.1. At *Re*=100,000 (Fig. 4.21b), both models correctly predict an attached boundary layer. In the low *TI* case at this Re, both models correctly predicted a large separation bubble, so they appear to handle the freestream turbulence effect correctly. The Trans-sst model provides a better prediction than the SKW-sst model at *Re*=100,000, particularly between s/L_s=0.5 and 0.7 where the data and the Trans-sst models show a slight plateau in C_p. The plateau indicates a boundary layer on the verge of separation or possibly a small separation bubble. For the *Re*=300,000 case (Fig. 4.21c), neither model nor the experiment show any indication of separation. Both models agree well with the experiment, with the Trans-sst model providing a slightly better prediction downstream of the suction peak. The simulations under predict the peak C_p in the *Re*=100,000 and 300,000 cases, and although the difference is not large, it is consistent with the difference between the data and the inviscid solution (Volino et al., (2008a) and Bons et al., (2008a)) saw a similar difference between their experimental data and simulations for similar conditions.

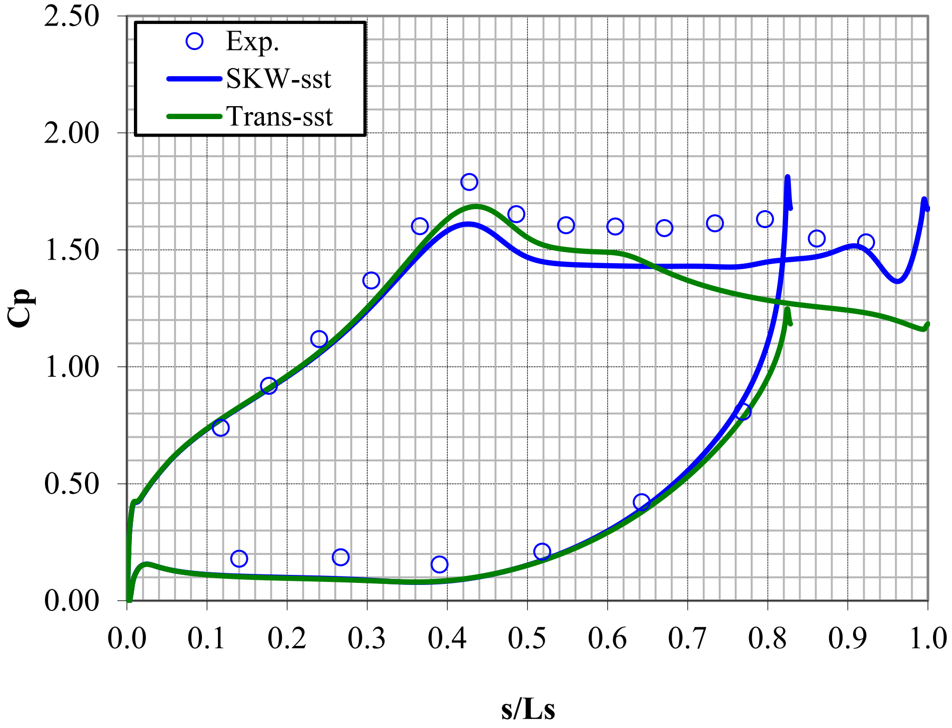

Figure 4.21-a: C_p profiles, *Re*=25,000 (HFSTI)

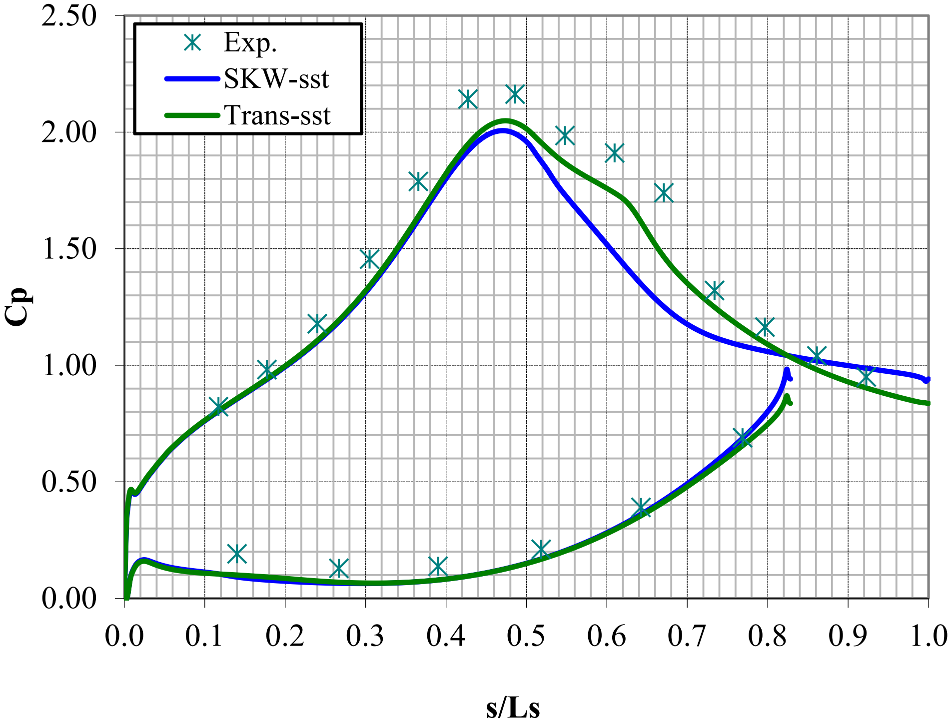

Figure 4.21-b: C_p profiles, *Re*=100,000 (HFSTI)

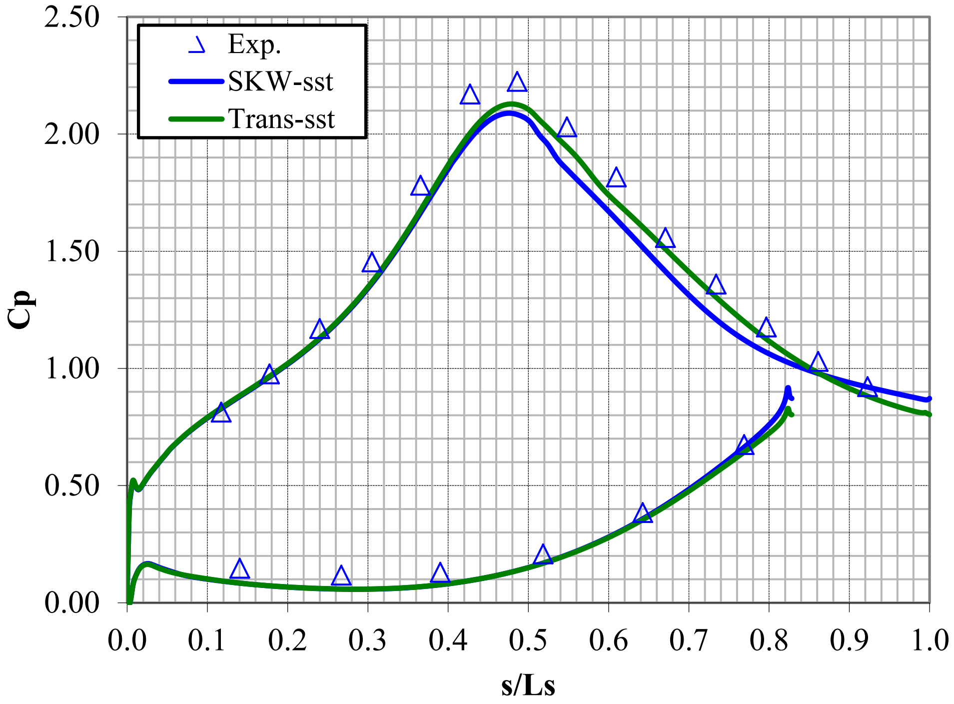

Figure 4.21-c: C_p profiles, *Re*=300,000 (HFSTI)

Mean velocity profiles for the *Re*=25,000 case are compared to the experiment in Fig. 4.22. Up to s/L_s=0.59, the turbulence model predictions agree well with each other and the experiment. Differences from the experiment inside the separation bubble are because of the limitations of the hot wire anemometry method used to measure velocities. The hot wire cannot distinguish the direction of reverse flow. Downstream of s/L_s=0.59, the models correctly predict the growth of the separation bubble. The Trans-sst model generally provides a better match to the data, although the SKW-sst model is closer at s/L_s=0.88. A thicker separation bubble in the simulation than the experiment, as shown at s/L_s=0.97, is expected in cases with large separation bubbles, particularly at downstream stations. This is due to the fact that the tailboard in the experiment suppresses the separation bubble somewhat in cases without reattachment, particularly on the airfoils closest to the tailboard. The simulation, with its periodic boundary conditions, corresponds to an infinite cascade with no tailboard effects.

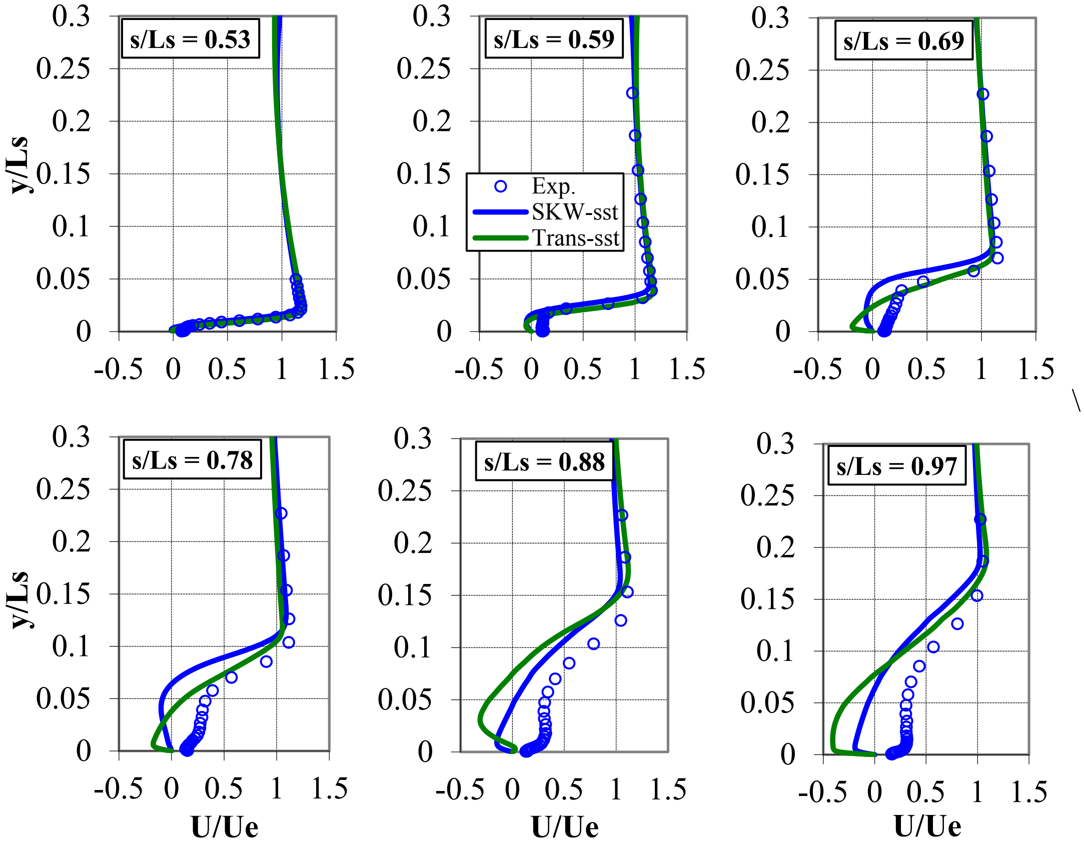

Figure 4.22: Comparison of computed and measured mean velocity profiles, *Re*=25,000 (HFSTI)

The kinetic energy of turbulence provides some information on how the simulation computes transition. The RMS fluctuating streamwise velocity, u', is estimated from the simulations using the computed turbulence kinetic energy and an assumption of isotropic turbulence. This assumption is clearly not strictly correct, but allows an estimate of u' to compare to the experimental data. This comparison is shown in Fig. 4.23 for the Trans-sst model in the *Re*=25,000 case. At s/L_s=0.53, there is a near wall peak in the experimental data which is not captured by the calculation. This is upstream of transition, so the peak is likely caused by the freestream turbulence buffeting the boundary layer. At all the other stations the peak is predicted at the correct distance from the wall. The simulation peak is about 40% too high at s/L_s=0.69, but at all the other stations the simulation and experiment peak magnitudes match closely. An exact match should not be expected given the approximation in estimating u' from the turbulence kinetic energy. Above the peak the match is also good, but closer to the wall the simulation shows higher fluctuating velocity than the experiment. Some of the difference may be attributed to the inability of the hot wire to measure velocity accurately inside the separation bubble, but it appears that the simulation predicts a thicker shear layer than the experiment. A thicker shear layer in the computation than the one observed in experiment was also observed in the low *TI* cases (see section 4.4.3).

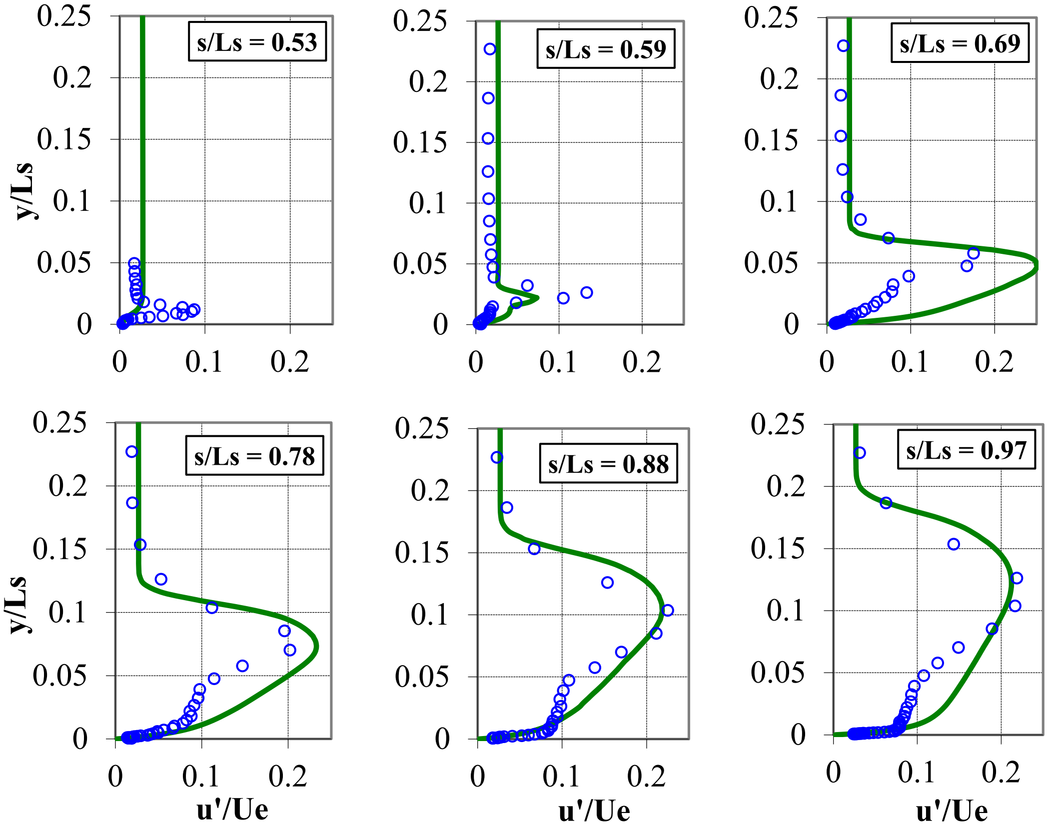

Figure 4.23: Comparison of computed with Trans-sst model and measured u′/U$_e$ profiles, *Re*=25,000 (HFSTI)

The rise in turbulence in the simulation can be used to predict the start of transition. The transition start location is designated as the location of the local maximum in turbulence kinetic energy following the suction peak, determined using the contours of Fig. 4.20. This is the same approach which was used in LFSTI cases. In the *Re*=25,000 case, the simulation predicts transition start at s/L_s=0.64, which agrees with the experimental location (Volino (2008a). The start of transition corresponds to the start of the slow drop in C_p shown in Fig. 4.21a. The mixing associated with transition makes a shear layer more likely to reattach. Perhaps the transition and turbulence predicted by the Trans-sst model is pushing the shear layer closer to reattachment than observed in the experiment, which could cause the lower C_p. The thicker shear layer in the simulation may cause this effect. The effect is not large enough to cause a full reattachment in the simulation, so the simulation and experiment remain in overall good agreement. The same drop in C_p was not observed in the LFSTI *Re*=25,000 case, possibly because transition did not occur until s/L_s=0.74, and the separation bubble had become too thick for any hint of reattachment. In LFSTI *Re*=100,000 case the transition start happened at s/L_s=0.59, and it induced the same slow drop in C_p shown in Fig. 4.21.

Figures 4.24 and 4.25 show the mean velocity and u' profiles for the *Re*=100,000 case. The Trans-sst model predicts the data well at most locations. Some difference in the shape of the mean profile is visible at the two most downstream stations, and the magnitude of the u' peak is underpredicted at the upstream stations. The freestream turbulence level in the experiment has also decayed more than in the simulation. The SKW-sst model does not do as good at the downstream stations, i.e. predicting a thicker boundary layer and a small separation bubble which were not observed in the experiment.

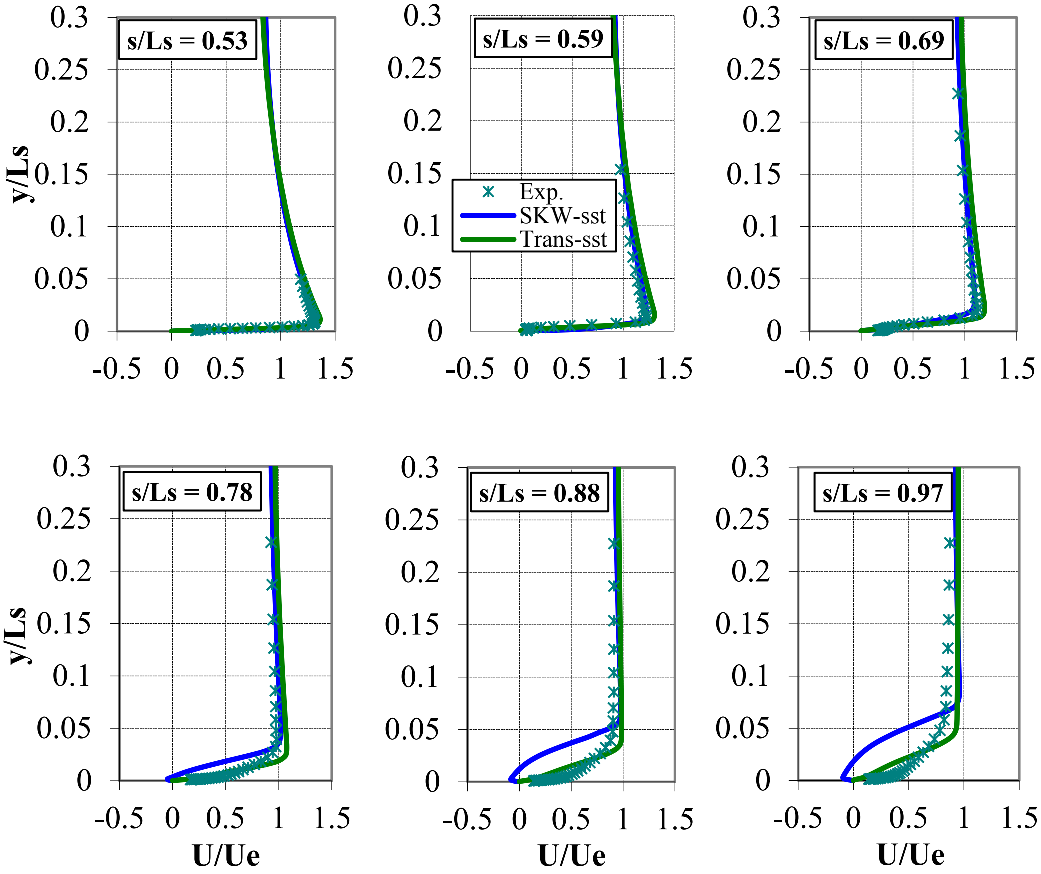

Figure 4.24: Comparison of computed and measured mean velocity profiles, *Re*=100,000 (HFSTI)

Velocity and turbulence profiles for the *Re*=300,000 case are shown in Figures 4.26 and 4.27. The Trans-sst model provides good agreement with the experimental mean profiles at all locations. With the same exceptions noted in Fig. 4.25, agreement is also good for the u' profiles. The SKW-sst model again predicts a thicker boundary layer than the experiment at the downstream stations. The Trans-sst model predicts transition start at s/L_s=0.66 and 0.64 in the *Re*=100,000 and 300,000 cases respectively. To within the experimental uncertainty, these locations agree with the experimental locations shown in Volino (2008a).

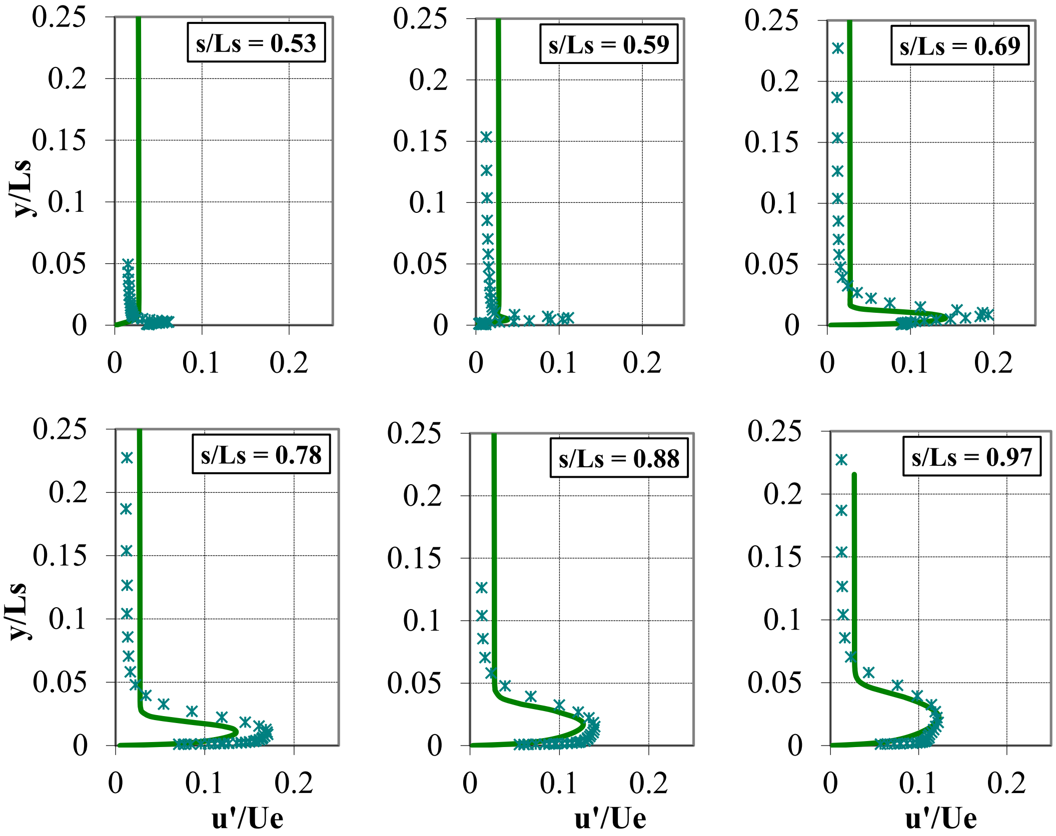

Figure 4.25: Comparison of computed with Trans-sst model and measured u′/U$_e$ profiles, *Re*=100,000 (HFSTI)

Total pressure loss coefficients are shown in Fig. 4.28. The magnitude and width of the loss peaks in the experiments and simulations generally agree, showing the correct trend with Reynolds number. In the *Re*=25,000 case (Fig. 4.28a), the simulations predict higher loss peaks and less flow turning than the experiment. This is expected since the tailboard suppresses the separation bubble somewhat in the experiment, as noted above. A thicker bubble in the simulation will result in higher losses and divert the flow toward the pressure side of the passage, moving the loss peak to lower φ/L_φ. Between wakes the Trans-sst model indicates lower loss than the experiment. This difference may be related to the under prediction of the freestream turbulence decay noted in Figures. 4.25 and 4.27. The *Re*=100,000 and 300,000 cases (Figures. 4.28b and 4.28c) do not suffer from tailboard effects in the experiment since the boundary layer reattaches. In both cases the Trans-sst model predicts the peak magnitudes to within about 5%, but the peak location is shifted slightly toward the pressure side of the passage in the simulation. The SKW-sst model does not do as well, predicting a higher peak and more of a shift toward the pressure side. As in the lower *Re* case, both models underpredict the loss between wakes.

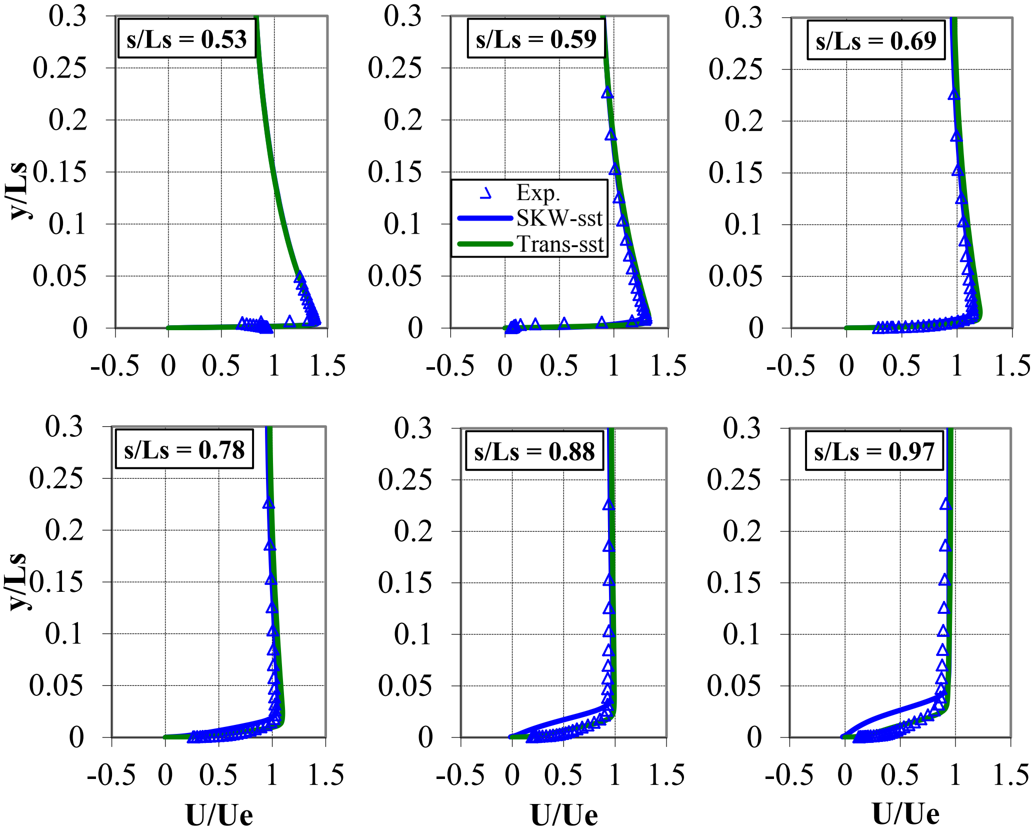

Figure 4.26: Comparison of computed and measured mean velocity profiles, *Re*=300,000 (HFSTI)

The flow over the very high lift L1A airfoil was studied in this section under high freestream turbulence conditions for Reynolds numbers 25,000 100,000 and 300,000. At the lowest Reynolds number, the laminar suction surface boundary layer separated and did not reattach.

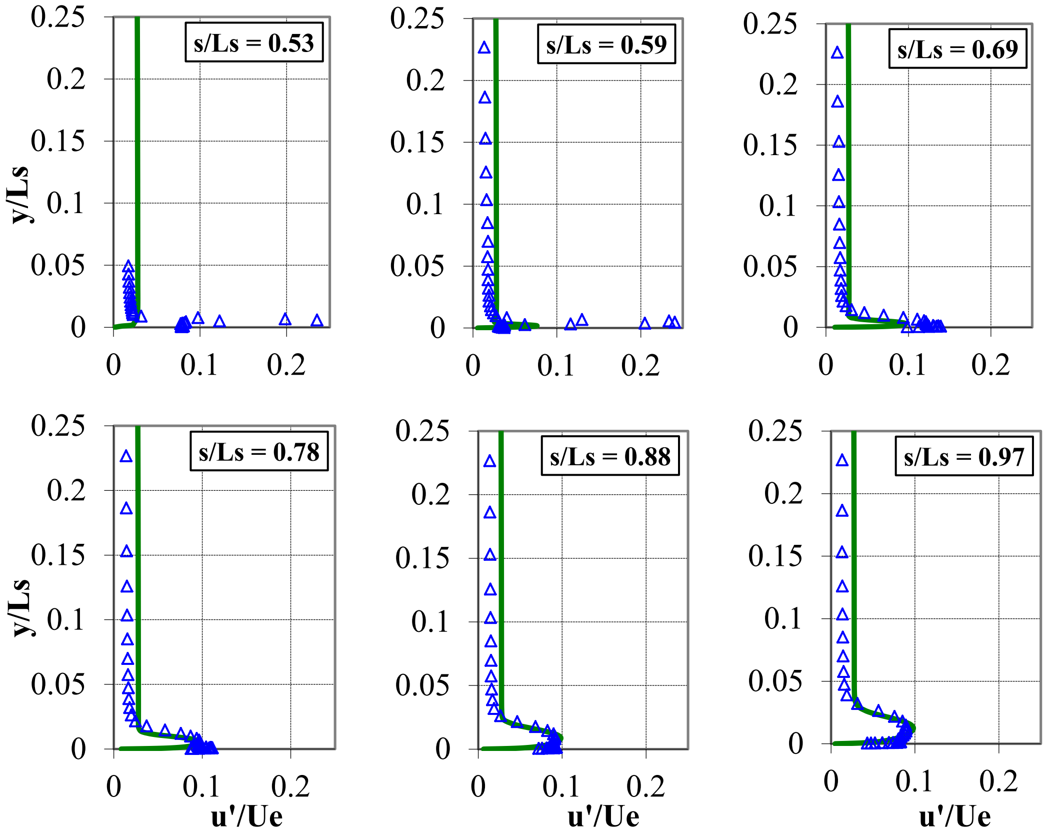

Figure 4.27: Comparison of computed with Transition-sst model and measured u′/U$_e$ profiles, *Re*=300,000 (HFSTI)

At the higher Reynolds numbers, a separation bubble was followed by transition and reattachment. The separation bubble became smaller as Reynolds number increased, and was effectively eliminated at the highest Reynolds number. The tendency toward separation at intermediate Reynolds number was still large enough to increase the boundary layer thickness and significantly increase pressure losses above the high *Re* cases. This results contrast with low freestream turbulence results. With low *TI*, the boundary layer did not reattach at intermediate Reynolds number (Re = 100,000), in spite of transition taking place in the separated shear layer. High freestream turbulence appears to increase the thickness of the shear layer over the separation bubble, thereby decreasing the bubble thickness. The thinner bubble results in turbulence closer to the wall when transition begins, which promotes reattachment. Reattachment changes the pressure distribution on the airfoil, causing the suction peak to rise and move downstream and delaying separation, which results in the higher lift and an even smaller separation bubble.

Numerical simulations with the 4 equation Trans-sst model of Menter et al., (2006) correctly predicted separation, transition and reattachment at all Reynolds numbers. Some discrepancies between the model prediction and the experimental data were noted, but in general the model predicted well the pressure distribution on the airfoil, the total pressure losses, and mean and fluctuating velocity profiles along the suction surface of the airfoil. The SKW-sst model of Menter (1994) did not do quite as good. The simulations correctly predicted the major differences between the high and low freestream turbulence cases.

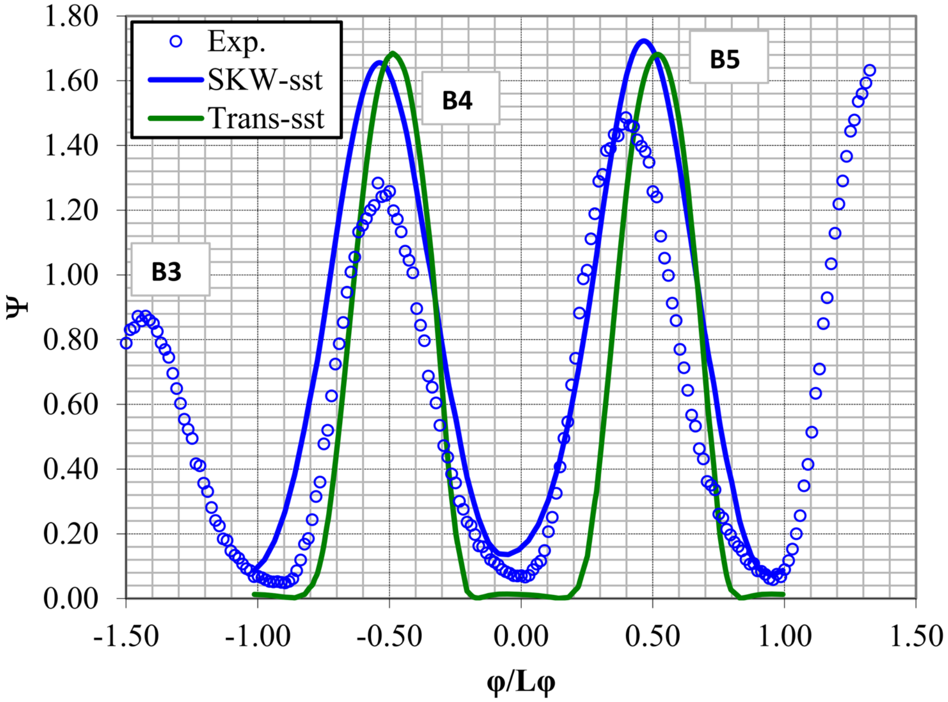

Figure 4.28-a: Total pressure loss coefficient at 0.63 C_x downstream of cascade, *Re*=25,000 (HFSTI)

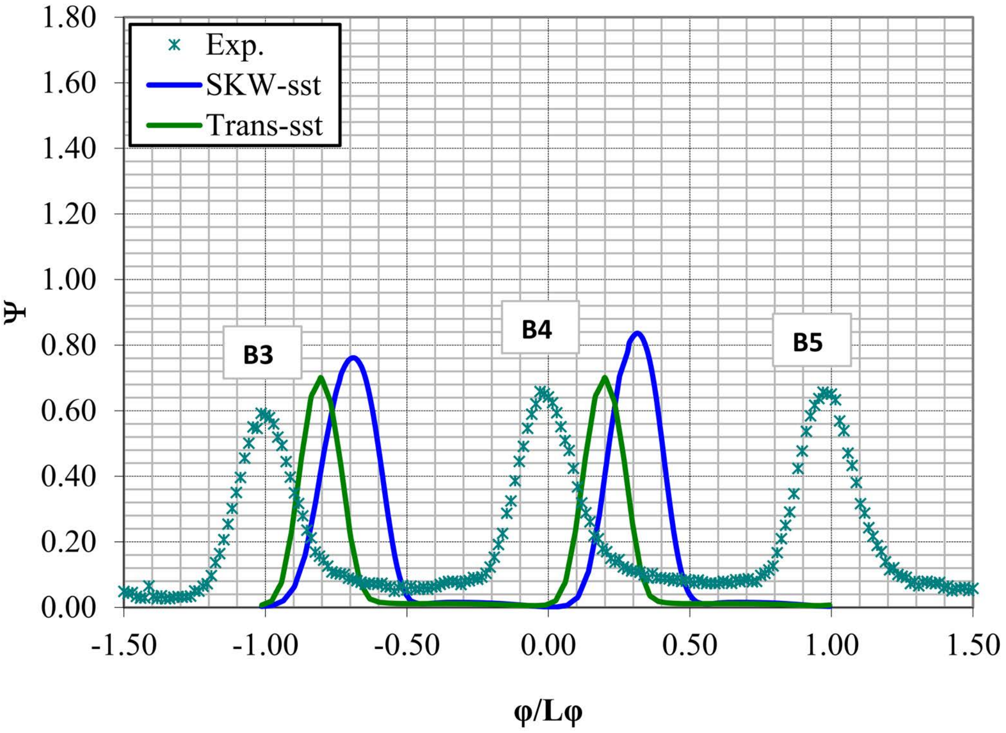

Figure 4.28-b: Total pressure loss coefficient at 0.63 C_x downstream of cascade, *Re*=100,000 (HFSTI)

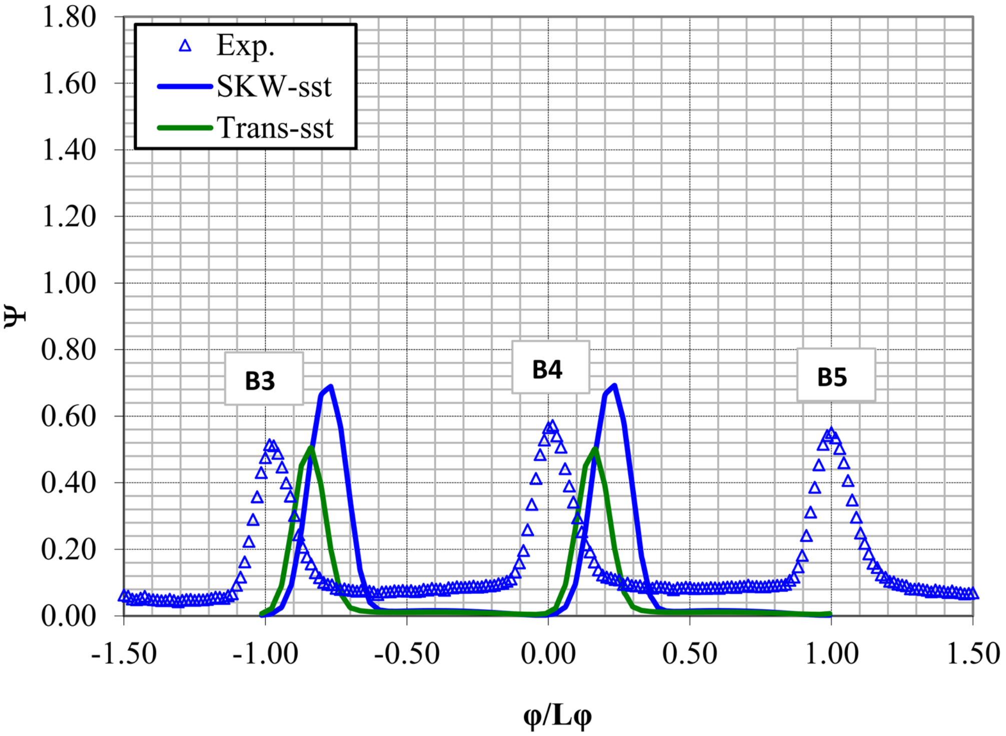

Figure 4.28-c: Total pressure loss coefficient at 0.63 C_x downstream of cascade, *Re*=300,000 (HFSTI)

In the next sections flow control using an active technique called Vortex Generator Jets (VGJs) is implemented in the cases with the large separation (low Re). Section 4.5 is devoted to the effects of the steady VGJs on separation. Effects of jets pulsation are examined in details in section 4.6.

4.5 Flow Control using Steady VGJs

Flow control studies were conducted for a lower range of Re: 25,000, 50,000 and 100,000, since at higher Re the flow was attached. To study an effect of jets blowing ratio on separation control the results of six cases ran are presented in this section. Two blowing ratios (low and high) were considered for each Re, they are: 1 and 3 for Re = 25,000; 0.5 and 2 for Re = 50,000 and 0.25 and 1 for Re = 100,000. Blowing ratio was defined as a ratio of the jet exit (at the center of the jet opening on the airfoil wall) and the crossflow velocities. Blowing ratio of 1, for example, was considered low for Re = 25,000 case and high for Re = 100,000 case. This is because the jet velocity in B=1, Re = 100,000 case was the same as the jet velocity in B=4, Re = 25,000 case.

The results in this section are presented in form of pressure coefficient and velocity and u’ plots on the airfoil. The results for Re = 25,000, B=1 and 3 are enhanced by the isosurfaces of x-velocity as well as x-vorticity and subgrid turbulence kinetic energy contours to illustrate the effect of the blowing ratio.

4.5.1 Re = 25,0000

Pressure coefficients plotted versus dimensionless distance along the suction side of an airfoil are presented on Fig. 4.29 for the Re = 25,000 case from experiment and

CFD using Trans-sst model and LES. Experiment for B=1 shows onset of separation at s/Ls = 0.5 with no reattachment indicated by the “plateau” in C_p downstream of s/Ls = 0.5. At B=3 significant reduction in size of separated region is observed from experiment (absence of the “plateau” in C_p).

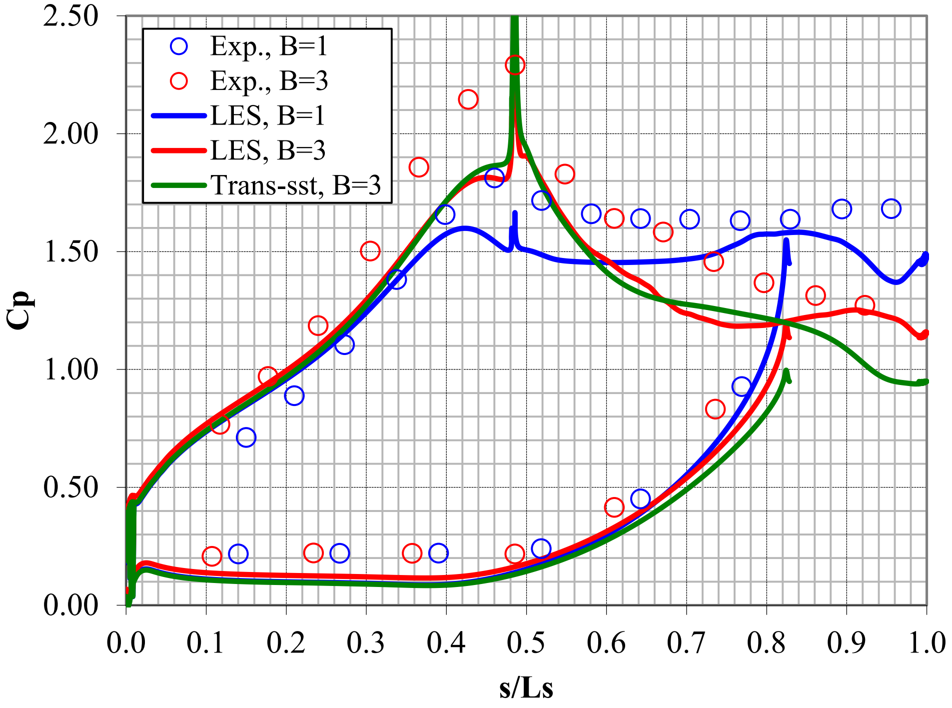

Figure 4.29: Pressure coefficient on the airfoil for steady blown VGJs at Re = 25,000

Computational (LES) results for two different blowing ratios (B = 1 and 3) are compared to the experiment with the same blowing conditions. For B = 1 both LES and experiment show flow separation starting after the suction peak with no reattachment, which is indicated by the large plateau in C_p after the suction peak. C_p at the suction peak is lower in CFD compared to experiment, but it is within the range of experimental uncertainty. The CFD results from Trans-sst turbulence model (B=3) are shown on Fig. 4.29 to show a comparison between RANS and LES. Trans-sst model predicts C_p

similar to LES, except for downstream locations (s/Ls = 0.8 - 1.0), where it predicts lower C_p values, than LES. This indicates smaller separation bubble modeled by RANS than by LES for Re = 25,000 and B = 3. The reason for not showing results from Trans-sst model and B = 1 is that at lower blowing ratio jets have no effect on separation and conditions are close to the "no-jets" case. As shown earlier in section 4.4.1, Trans-sst model predicts C_p reasonably well compared to experiment for "no-jets" cases.

Velocity profiles normalized by the nominal exit velocity are plotted versus dimensionless distance from the wall in the direction normal to the wall on Fig. 4.30 for the same Re (25,000). The results for the 6 measurement stations located downstream of the suction peak of the airfoil are shown. Computational velocity profiles from LES for B = 1 and B = 3 are shown. Experimental data and Transition-sst results are only available for B = 3. For B = 1, LES shows separation starting at station 2 and large separation bubble is present at all stations from 2 to 6, based on negative velocities near the wall at those locations. For B = 3 both Trans-sst and LES show separation started at station 4 and continuing at stations 5 and 6. Separation bubble is smaller than that for B = 1. LES is in a reasonably good agreement with experiment. It should be noted the larger disagreement near the wall is due to limitations of the hot wire anemometry method used in experiment, which is not capable of measuring negative velocities. The Trans-sst model overpredicts velocities near the wall and underpredicts the size of the separation bubble, compared to LES and experiment.

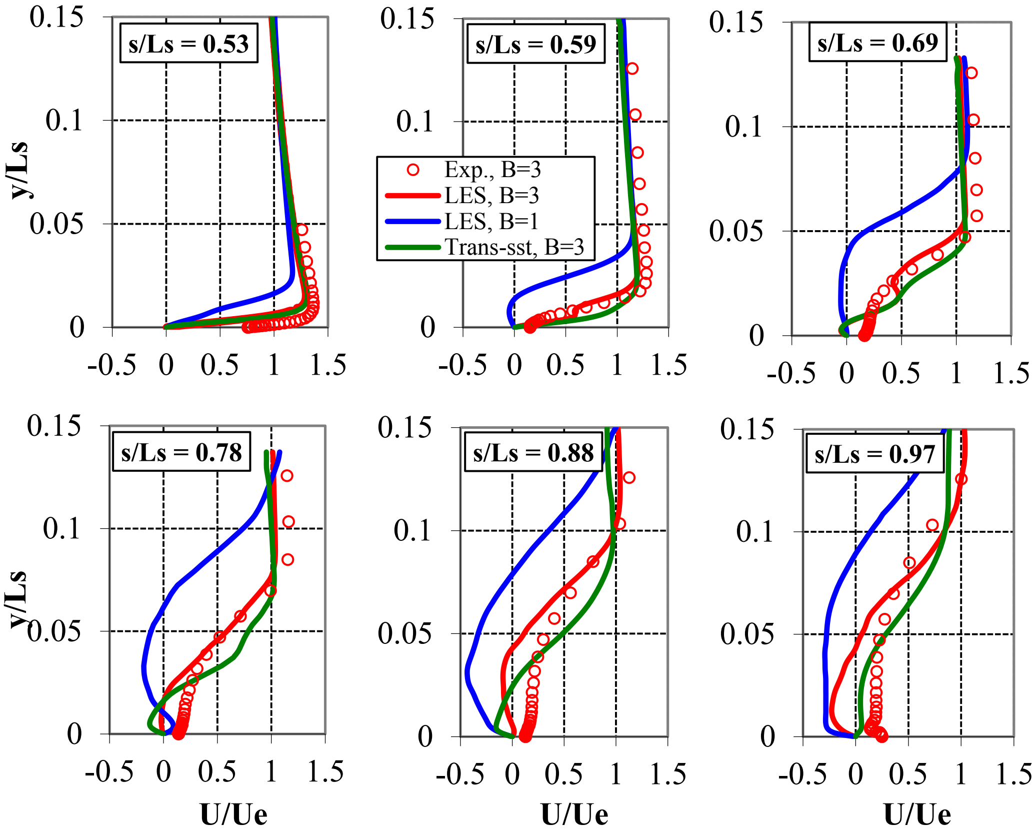

Figure 4.30: Velocity profiles at six measurements stations on the airfoil's suction side for steady blown VGJs at Re = 25,000

Profiles of the streamwise component of the RMS fluctuating velocity, u', normalized by the nominal exit velocity are plotted versus dimensionless distance from the wall in Fig. 4.31 for the same case. The results for 6 measurement stations located downstream of the suction peak of the airfoil are shown. Computational and experimental profiles are for B = 3. The experiment shows the location of the peak is away from the wall indicating the presence of a separation bubble. LES predicts similar bubble size (location of the peak of u') as experiment with some disagreement in magnitude of u' near wall. Since limitations of the hot wire anemometry near the wall, values from CFD and experiment in this region are not expected to match.

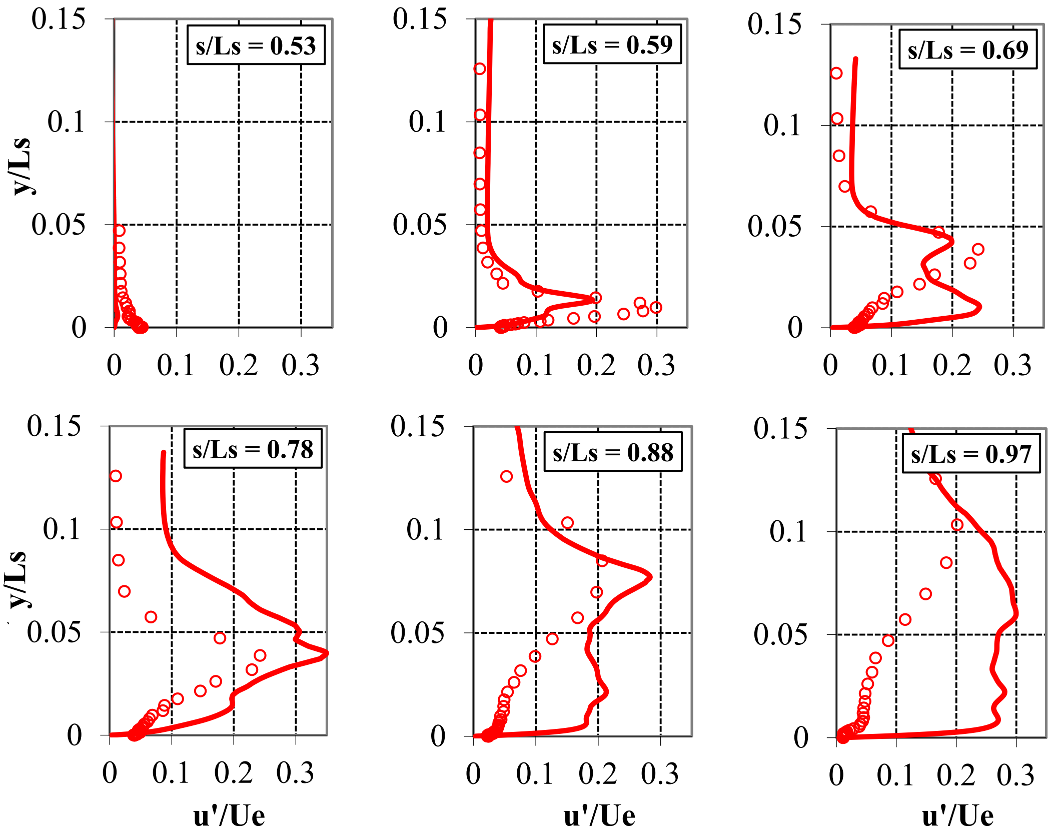

Figure 4.31: RMS of the fluctuating component of the streamwise velocity at six measurements stations on the airfoil's suction side for steady blown VGJs at Re = 25,000, B=3 from the Trans-sst model.

For the purpose of visualization of the separated region and effects of the jet's blowing ratio, iso-surfaces of instantaneous axial velocity (Vx = 0.01 m/s) are shown in Fig. 4.32 for B = 1 and B = 3. These CFD results are from the LES model. The reason for choosing Vx = 0.01 m/s is that this small (but not negative) value represents velocity in the shear layer of the separation bubble and helps to visualize the size of the bubble and shapes of the vortices created by the jets. The airfoil with 3 jets on the suction side near the suction peak is shown as a "mirror" image (only one jet was modeled in CFD). In the case with B = 1 the low velocities in the shear layer of the separation bubble are at a distance from the wall, thus the separation bubble is large. No intense mixing is observed at this iso-surface and the fluid issuing from the jet is moving aligned with the cross flow direction at this low blowing ratio. The separation bubble is smaller in the B = 3 case, low velocities in the shear layer are closer to the wall than in the B = 1 case. The visualization shows more mixing happening near the wall (the iso-surface is less smooth than in B = 1 case). The fluid coming from the jet is moving at an angle with the flow direction downstream of the suction peak of the airfoil due to the high momentum jets at B = 3.

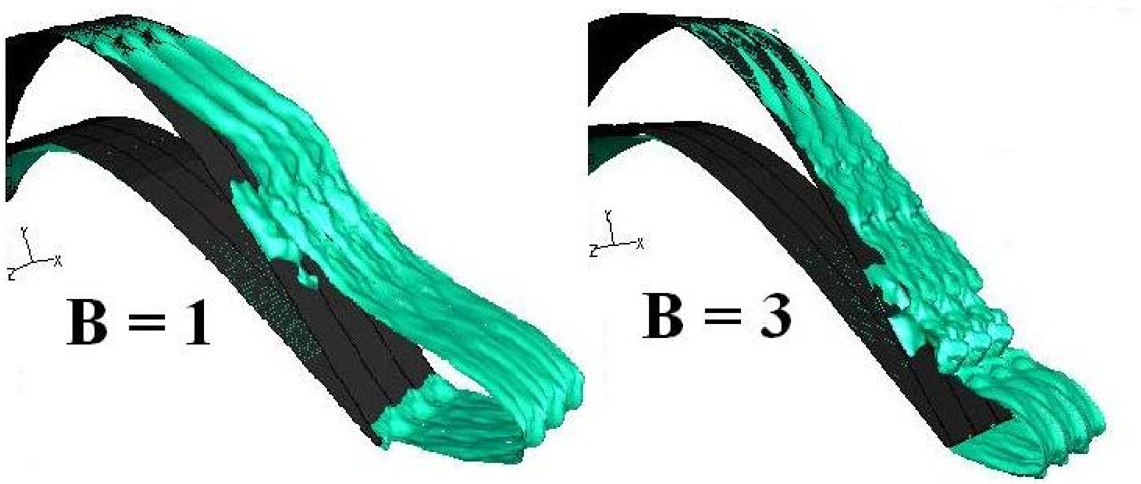

Figure 4.32: Instantaneous isosurfaces of Vx=0.01 m/s for steady blown VGJs at Re = 25,000 from LES

Instantaneous axial vorticity contours are presented in Fig. 4.33 for the B = 1 and B = 3 cases for Re = 25,000 (LES). For B = 1 maximum vorticity is in the shear layer of the separation bubble away from the wall between stations 3 and 4. In the B = 3 case the region with high vorticity (more mixing) is in the shear layer, but closer to the wall than in the B = 1 case. The location of the high vorticity region has moved upstream and it is between stations 2 and 3. More mixing in the high blowing ratio case (indicated by the streamwise vorticity contours) helps to reduce the size of the separation bubble (indicated also by the velocity plots - Fig. 4.30).

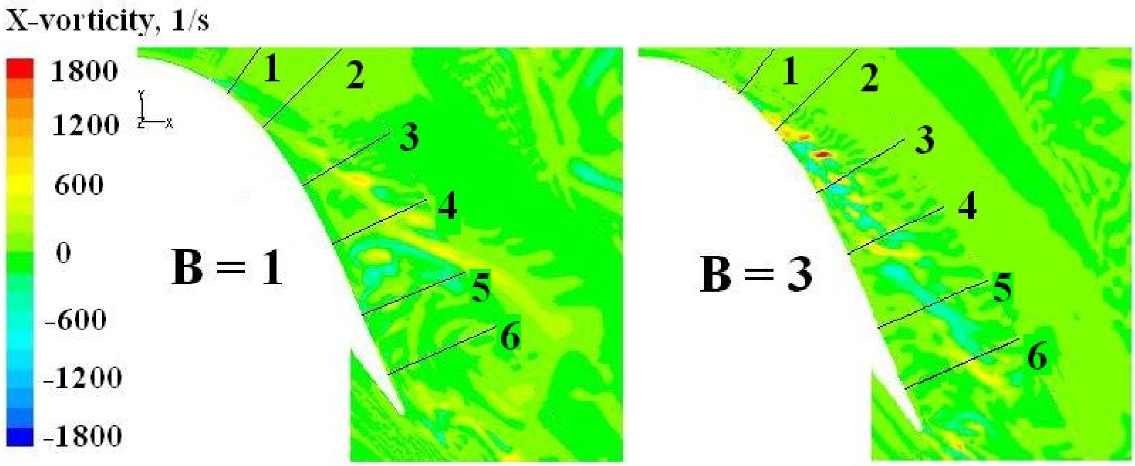

Figure 4.33: Instantaneous X-vorticity for steady blown VGJs at Re = 25,000

Figure 4.34 presents views of 6 planes of measurement stations (see Table 4.5) along the airfoil suction side downstream of the jets locations. Subgrid turbulent kinetic energy (TKE) contours are displayed for Re = 25,000, B = 1 (4.34a) and B = 3 (4.34b) cases. In the low blowing ratio case (B = 1) the high turbulence region is located at station 4 away from the wall. In the high blowing ratio case (B = 3) the high turbulence region is located already at station 1 in the vortex close to the wall. These elevated turbulence levels near the suction peak of the airfoil contribute to the reduction of separation.

4.5.2 Re = 50,000

At Re=50,000, and B =0.5, the flow was still separated with no reattachment. A value of B=2 was needed to get the flow attached with very small separation near the trailing edge. Pressure coefficient plotted versus dimensionless distance along the suction side of an airfoil is presented on Fig. 4.35. Computational LES results for two blowing ratios (B = 0.5 and B = 2) were compared to the experiment with the same blowing conditions.

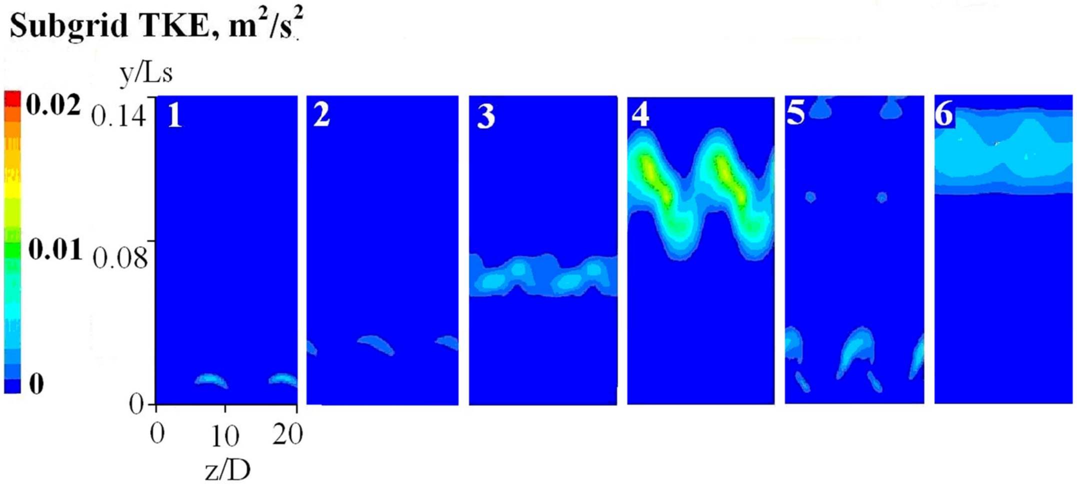

a) B = 1

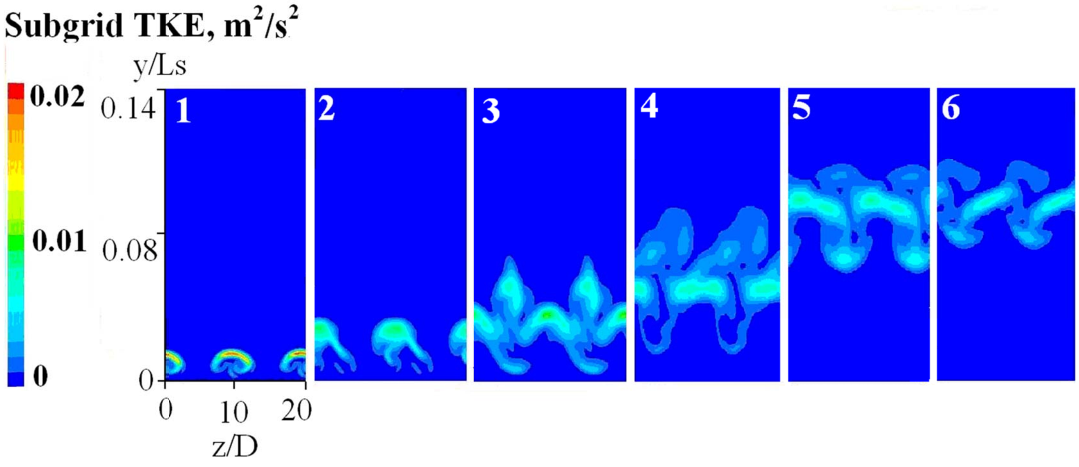

b) B = 3

Figure 4.34: Subgrid turbulence kinetic energy (TKE) at the spanwise oriented planes of 6 measurement stations for steady blown VGJs at Re = 25,000

Blowing ratio of 0.5 results in a large separation shown by both LES and experiment, which is indicated by the large plateau in C_p downstream of the suction peak (starting at s/Ls = 0.5 - upstream of station 1). In B = 2 case separation is reduced in size and delayed to a further downstream location, compared to the B = 0.5 case in LES. The location of the start of the "plateau" in C_p has moved downstream to s/Ls = 0.8 (between stations 3 and 4) in CFD. The C_p values from LES are below the experimental ones and the experiment does not show any "plateau".

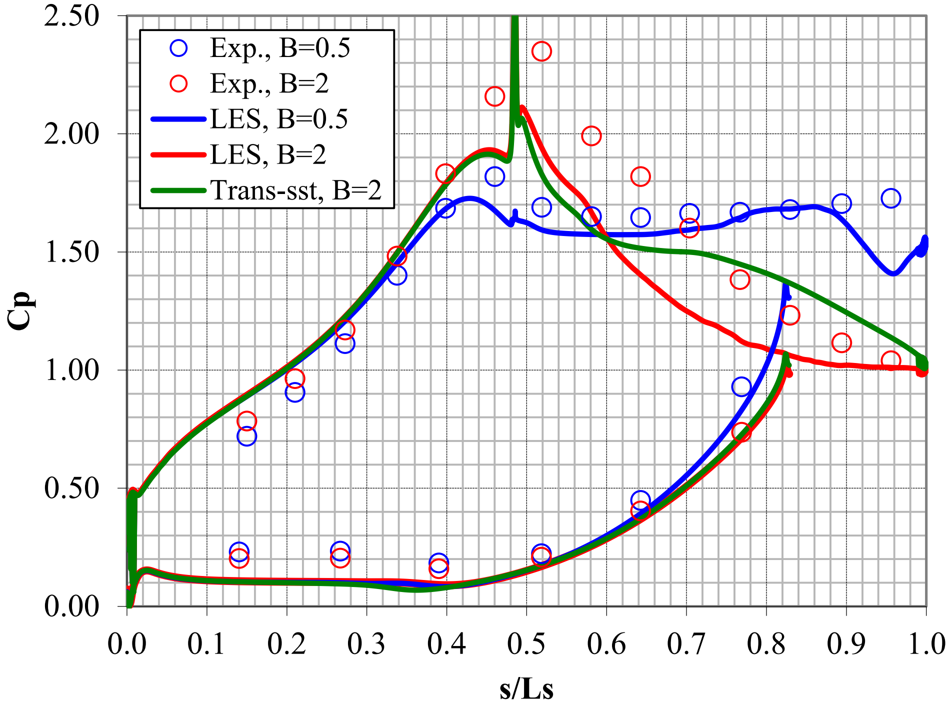

Figure 4.35: Pressure coefficient on the airfoil for steady blown VGJs at Re = 50,000

The Trans-sst model over predicts C_p downstream of the s/Ls = 0.6 (starting at station 2), compared to LES and experiment for the B = 2 case. This indicates a larger separation bubble predicted by the Trans-sst model with the location of the separation moved upstream.

Velocity profiles normalized by the nominal exit velocity, plotted versus dimensionless distance from the wall in the direction normal to the wall for Re = 50,000 are presented on Fig. 4.36. Computational velocity profiles from LES for B = 0.5 and B = 2 are shown. Experimental and Trans-sst model results are only available for B = 2. The results for 6 measurement stations from LES for B = 0.5, show separation present already at station 1 and continuous through station 6, which is consistent with the location of the plateau in C_p, observed from Fig. 4.35. For B = 2 LES shows separation started between stations 4 and 5 with no reattachment. Separation bubble is smaller than in B = 0.5 case.

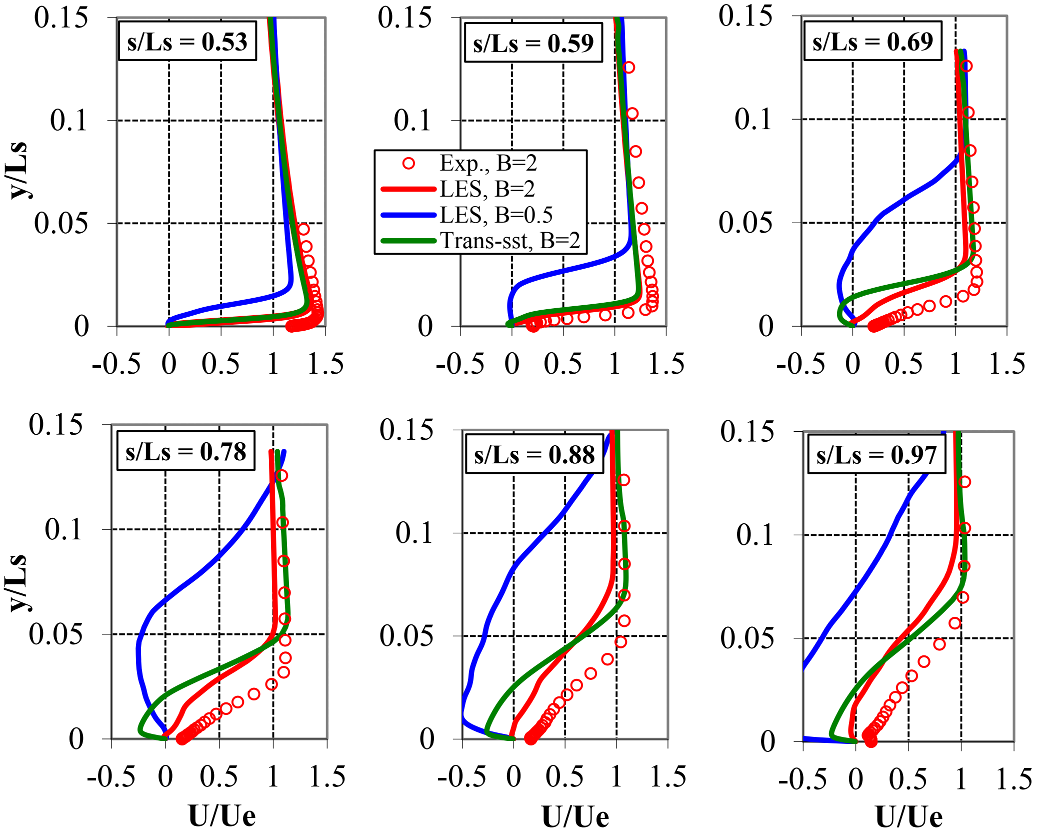

Figure 4.36: Velocity profiles at six measurements stations on the airfoil's suction side for steady blown VGJs at Re = 50,000

These results are in a relatively good agreement with experiment with some under prediction of the velocities at stations 3-6. The difference in the velocities near the wall is due to the hot wire anemometry being used in experiment. Trans-sst model under predicts velocities near the wall and shows larger size of the bubble, compared to LES and experiment. This model predicts separation starting earlier i.e. at station 2.

RMS u' profiles normalized by the nominal exit velocity are plotted versus dimensionless distance from the wall in Fig. 4.37. Computational (LES) and experimental profiles are for B = 2. CFD overpredicts u' at stations 3-6 and underpredicts u' at station 2. This could be responsible for the slightly larger separation bubble predicted under these flow conditions.

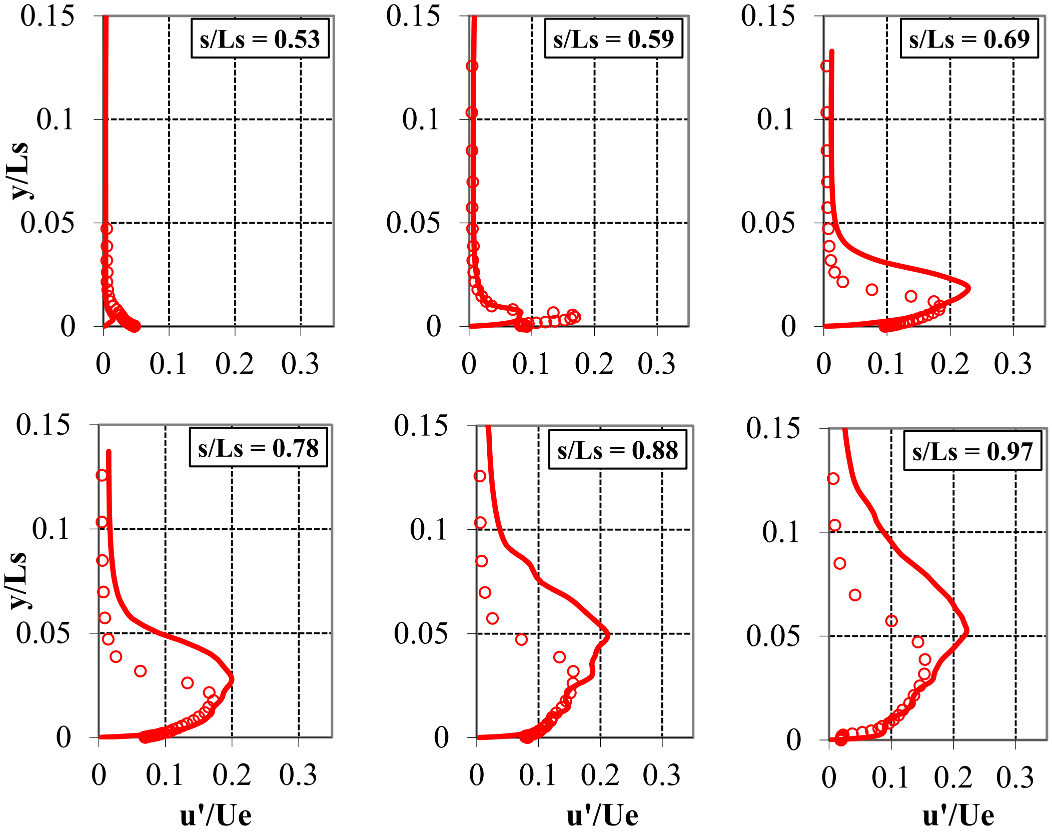

Figure 4.37: RMS of the fluctuating component of the streamwise velocity at six measurements stations on the airfoil's suction side for steady blown VGJs at Re = 50,000, B = 2, from LES.

4.5.3 Re = 100,000

In the case of Re=100,000 and B=0.25 the flow separates with reattachment downstream of the suction peak. At higher blowing ratios (B=1) the flow becomes attached along the whole airfoil length.

On the pressure coefficient plot (Fig. 4.38) computational (LES) results for B = 0.25 and 1 are compared to experimental data for the same blowing ratios. Blowing with B = 0.25 causes flow to reattach after small separation region starting near s/Ls = 0.6 in both CFD and experiment.

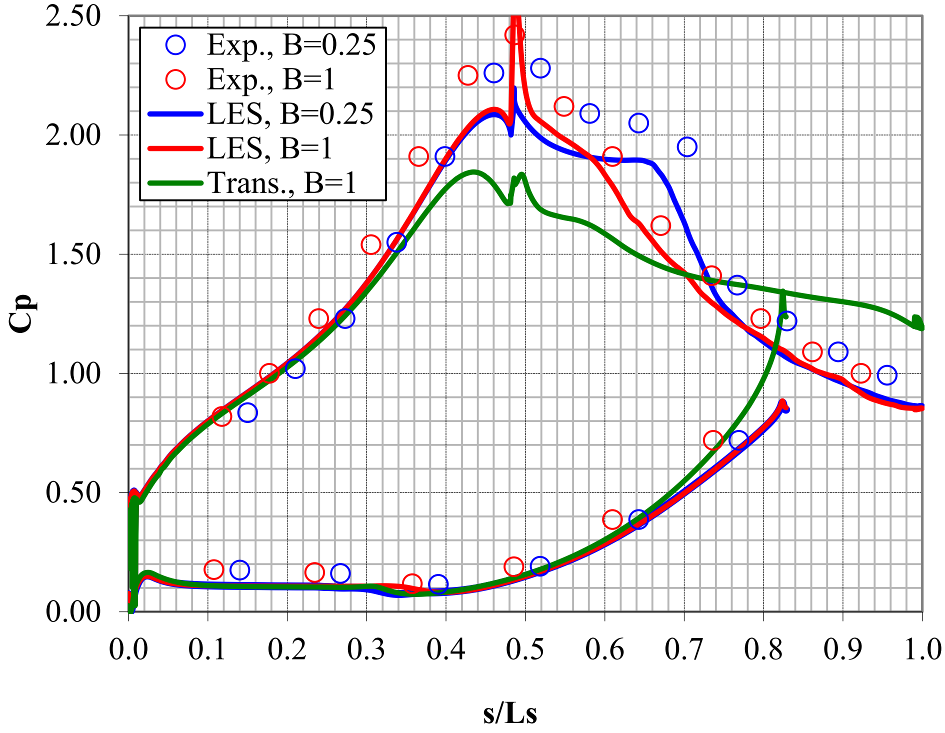

Figure 4.38: Pressure coefficient on the airfoil for steady blown VGJs at Re = 100,000

Experimental and computational (LES) C_p profiles indicate attached flow at all locations on the suction side of the airfoil under high blowing ratio conditions (B=1). The computational C_p profile from the Trans-sst model is shown only for B=1. The Trans-sst model predicts separated flow on the suction side of the airfoil, starting at s/Ls = 0.5 with no reattachment downstream. Overall LES is in a good agreement with experiment, while RANS is not able to predict the flow correctly.

Figure 4.39 shows velocity profiles from LES for B = 0.25 and B = 1 and from Trans-sst model for B = 1. Experimental velocity profiles for B = 1 were not available therefore velocity profiles for B = 0.75 are shown. Experimental C_p profiles for those two cases are very similar and indicate attached flow. The Trans-sst model results are shown for B = 1.

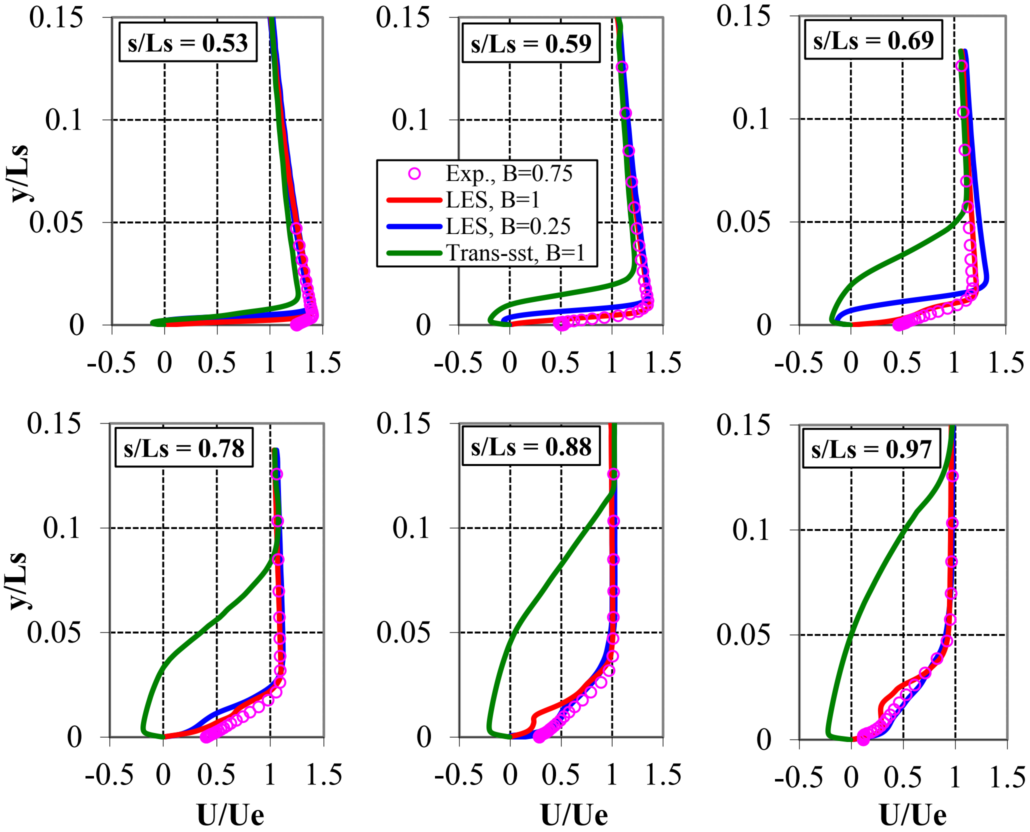

Figure 4.39: Velocity profiles at six measurements stations on the airfoil's suction side for steady blown VGJs at Re = 100,000

The results for 6 measurement stations from LES for B = 0.25 show separation starting at station 2 and reattachment at station 4, which is consistent with the location of the plateau in C_p, observed from Fig. 4.38.

LES with B = 1 shows attached flow at all six measurement stations. Experimental results for B = 0.75 indicate attached flow as well. For stations 1-4 LES velocity profiles for B=1 match the experimental profiles for B=0.75 very well. At stations 5 and 6 the CFD results indicate flow tendency toward separation, which was not observed from the experimental data for B=0.75. The Trans-sst model predicts separation starting at station 2 and continuing through station 6. Velocity profiles from this model show significant underprediction compared to LES and experiment.

RMS of the fluctuating component of streamwise velocity normalized by the nominal exit velocity is plotted versus dimensionless distance from the wall in the direction normal to the wall on Fig.4.40 for Re = 100,000.

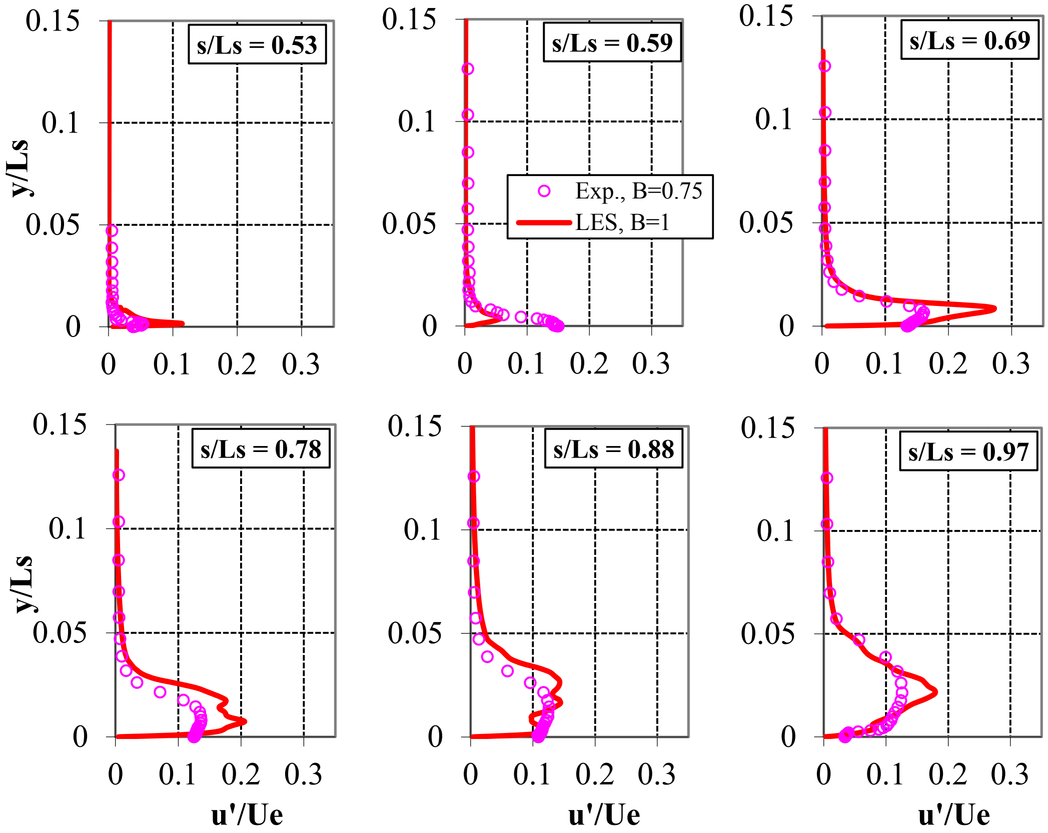

Figure 4.40: RMS of the fluctuating component of the streamwise velocity at six measurements stations on the airfoil’s suction side for steady blown VGJs at Re=100,000

The results for 6 measurement stations located downstream of the suction peak of the airfoil are shown for B = 1 (CFD) and B = 0.75 (experiment). The agreement between CFD and the experiment is reasonable, including the magnitude and location of the maximum u'.

An active flow control was implemented for the L1A airfoil utilizing steady VGJs and then studied computationally with LES and RANS in this section. The study was enhanced by additional grid independence study for the necessary grid resolution around the jets and in the spanwise direction. URANS approach was compared with LES and experiment to test its ability to accurately predict effect of VGJs on the boundary layer separation.

Cases were considered at Reynolds numbers (based on the suction surface length and the nominal exit velocity from the cascade) of 25,000, 50,000 and 100,000. In all cases without flow control, the boundary layer separated and did not reattach.

In Re = 25,000 case experimental data for C_p shows that for B=1, the flow separates at s/Ls between 0.53 and 0.59, with no reattachment; while at B=3, it is not clear if the flow is attached along the airfoil. The velocity profiles data, however, show that the flow separates between s/Ls =0.59 and 0.69. Furthermore the location of the peak of u' is away from the wall indicating the presence of a bubble. The LES results are in a reasonable agreement with the data for B=1; for B=3 both LES and Trans-sst model (for both Cp and U/Ue) are in good agreement with data up to s/Ls = 0.8. The LES data for u' compare well with the experiment. Overall the LES predictions are in a better agreement with the data than the URANS.

In the Re = 50,000 case experimental data for both Cp and velocity profiles show that for B=0.5, the flow separates at s/Ls = 0.53 with no reattachment; while at B=2, flow is almost attached along the airfoil with only a small bubble present. Also, the location of the peak of u' is away from the wall indicating the presence of a bubble. The LES results are in excellent agreement with the data for B=0.5 and showing the same trend for B=2. Also, for B=2, LES compares reasonably well with the data including magnitude and location of u'. As for the Trans-sst model for B=2 it over predicts C_p downstream of the s/Ls = 0.6, and under predicts velocities near the wall. This indicates a larger separation bubble predicted by the Trans-sst model compared to LES and experiment with the location of the separation moved upstream. Overall the LES predictions are superior to the Trans-sst model predictions and in a better agreement with the data.

In Re = 100,000 case experimental data for C_p shows that for B=0.25, the flow separates at s/Ls = 0.53 with reattachment at s/Ls = 0.7; while at B=1, the flow is fully attached along the airfoil. Also, the velocity profiles data for B=0.75 show that the flow does not separate. Furthermore the location of the peak of u' is close to the wall indicating attached flow. The LES results are in excellent agreement with the data. On the other hand the Trans-sst model, B=1, shows separation at s/Ls = 0.59 and no reattachment; it significantly underpredicts velocity profiles compared to LES and experiment. Overall the LES predictions are superior to the Trans-sst model predictions and in a better agreement with the data.

Effect of jets pulsation is examined in the following section.

4.6 Flow Control Using Pulsed VGJs

Seven cases are examined in this section in order to demonstrate jets pulsations effect on the control of separation. Cases at Re = 25,000, 50,000 and 100,000 with different blowing ratios, frequencies and duty cycles of blowing were considered. Table 4.8 shows a summary of pulsed VGJs cases ran.

Table 4.8: Pulsed VGJs Test Matrix (NA = not available)

f, Hz	**DC %**	**Re/B**		
		25,000/1.0	**50,000/0.5**	**100,000/0.25**
3	10	Case (1)	Case (2)	Case (3)
12	10	Case (4)	Case (5)	NA
24	10	NA	Case (6)	NA
12	50	NA	Case (7)	NA

4.6.1 Pressure and velocity distributions

Statistical averages of the pressure coefficient C_p plotted versus dimensionless distance along the suction side of an airfoil are presented on Figures 4.41 to 4.47 for all (7) cases shown in Table 4.8. These cases represent a combination of variation in Re (25,000, 50,000 and 100,000), dimensionless frequency $F = fL_{j\text{-}te}/U_{ave}$, (from 0.035 to 0.56) and duty cycle (10% and 50%).

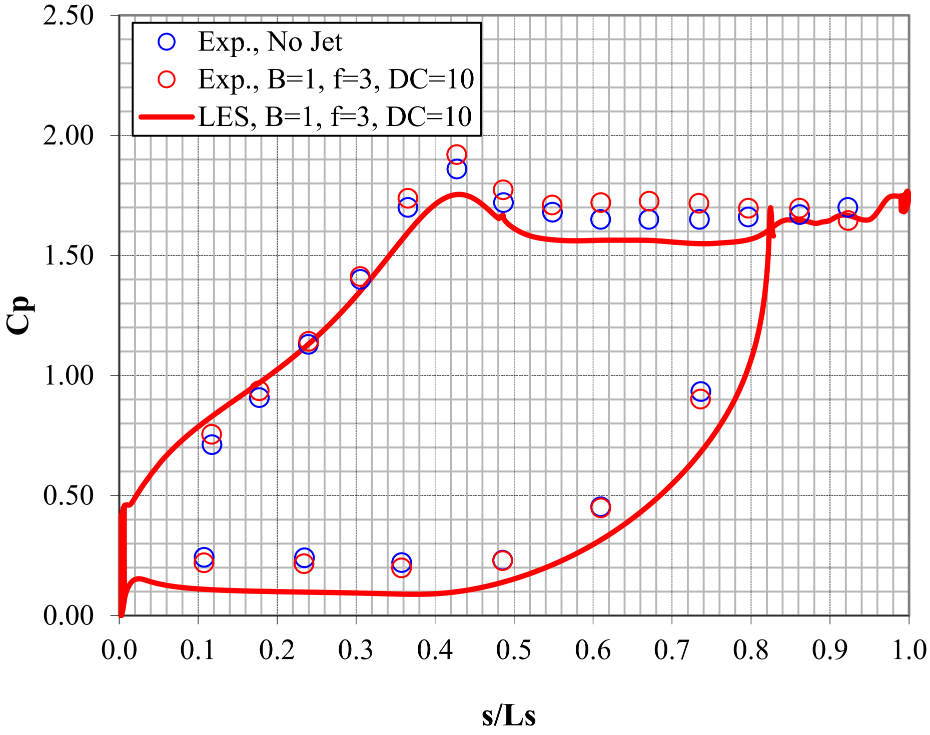

Figure 4.41: C_p for case (1) Re = 25,000, B = 1.0, f = 3 Hz (F = 0.14), DC = 10%

Figures 4.41, 4.42 and 4.43 show C_p for Cases 1 (F=0.14), 2 (F=0.07), and 3 (F=0.035), respectively with the same frequency (f=3 Hz) and duty cycle of 10%. The Re number varied from 25,000 to 100,000. The figures show flow separation starting after the suction peak with no reattachment, which is indicated by the large "plateau" in C_p after the suction peak. Magnitude of C_p at the suction peak is lower in CFD compared to experiment, which could be attributed to experimental uncertainty as well as the differences in B.C. and to the limitations of the present computational model (LES was used for modeling turbulence, when Direct Numerical Simulation (DNS) might be needed to resolve all eddies responsible for the turbulent mixing and therefore for the flow control effects). Despite this fact, the phenomena predicted by the LES agree with experiment (i.e. separation, reattachment or attached flow) under the same flow conditions.

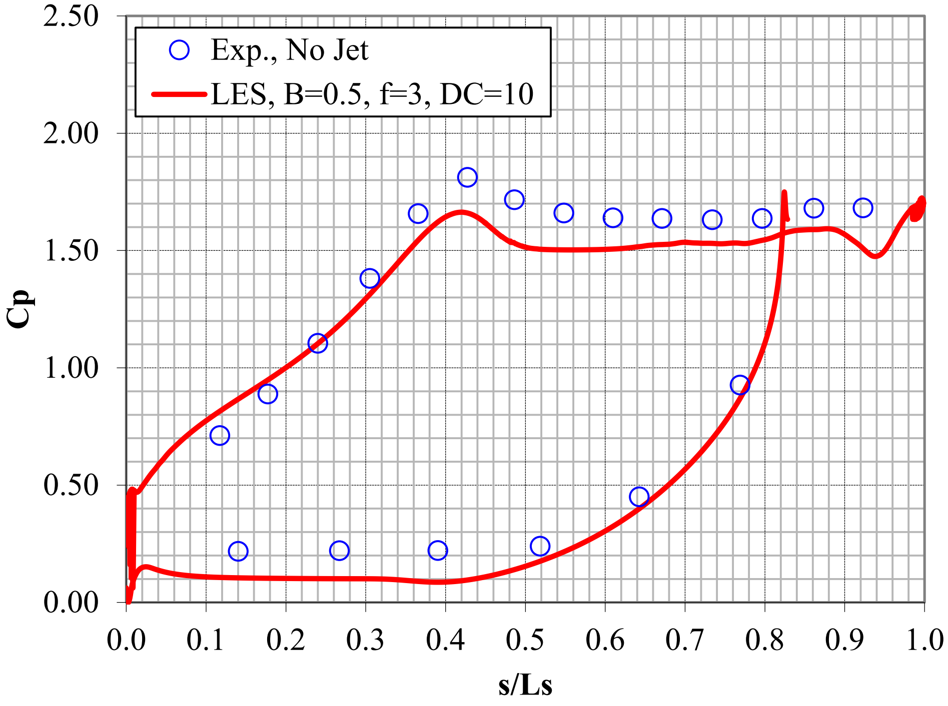

Figure 4.42: C_p for case (2) Re = 50,000, B = 0.5, f = 3 Hz (F = 0.07), DC = 10%

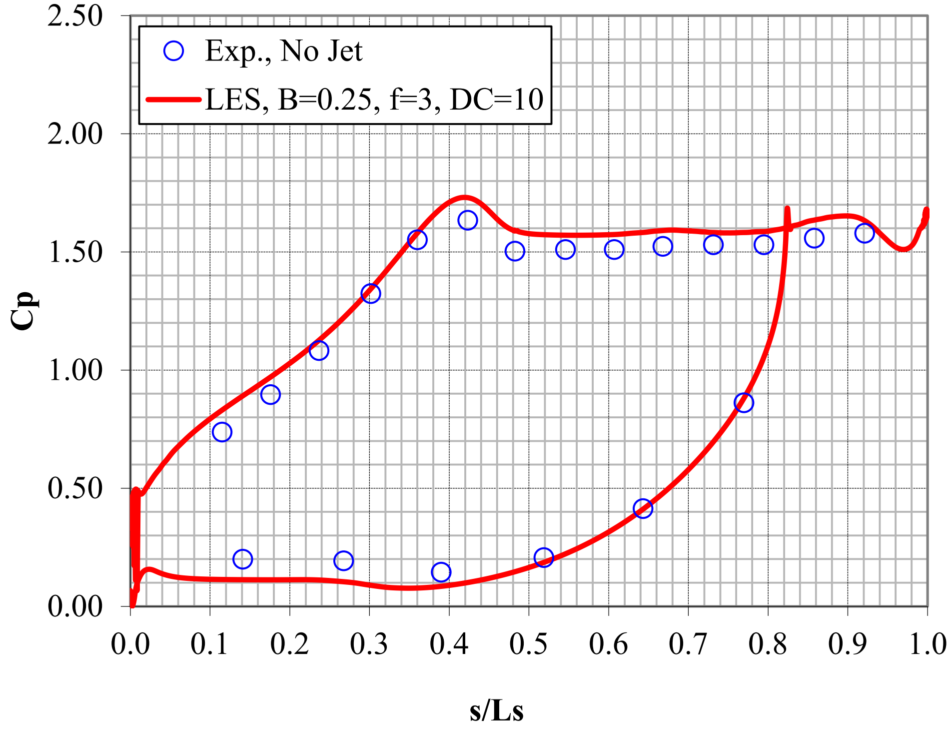

Figure 4.43: C_p for case (3) Re=100,000, B=0.25, f=3 Hz (F=0.035), DC=10%

The LES predictions are shown together with experimental data for the same case or no jet (due to the absence of experimental data for Cases 2 and 3) on Fig. 4.41, 4.42 and 4.43. It is clear that all cases exhibit separation with no attachment similar to the cases without jet blowing. The main reason is the low frequency at which blowing occurred together with a low duty cycle that resulted in minimizing the presence of the jet.

Figures 4.44 and 4.45 show Cp for Cases 4 (F=0.56) and 5 (F=0.28) respectively. For two dimensionless frequencies above the physical frequency has the same value of 12 Hz. The duty cycle is 10%. The Re number varied from 25,000 to 50,000. The figures show flow separation starting after the suction peak with reattachment from experiment for both cases. The LES predictions for case (4) indicate rather reduction of separation bubble than reattachment starting at $s/L_s \sim 0.7$. Disagreement with experiment in this case is expected, since we know that the tailboard has a tendency to suppress separation at low Re in experiment. The agreement between the CFD and experiment is reasonable for case (5), where LES predicts reattachment at $s/L_s \sim 0.7$. In general it was observed that reattachment occurred at the higher frequencies of blowing tested (compare Cases (1), and (4) and Cases (2) and (5)).

Figure 4.46 shows C_p for case (6) with Re =50,000, F=0.56 (f=24 Hz) and duty cycle of 10% from both LES and experiment. The figure shows flow separation starting after the suction peak with reattachment downstream. The LES predictions are in a reasonable agreement with experiment.

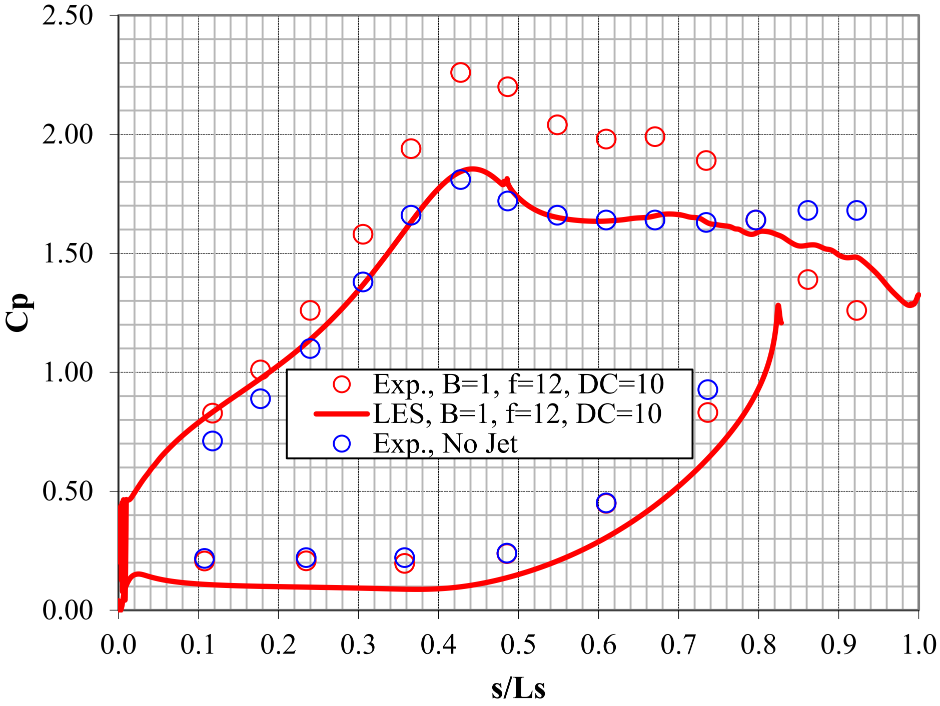

Figure 4.44: C_p for case (4) Re = 25,000, B = 0.1, f = 12 Hz (F = 0.56), DC = 10%

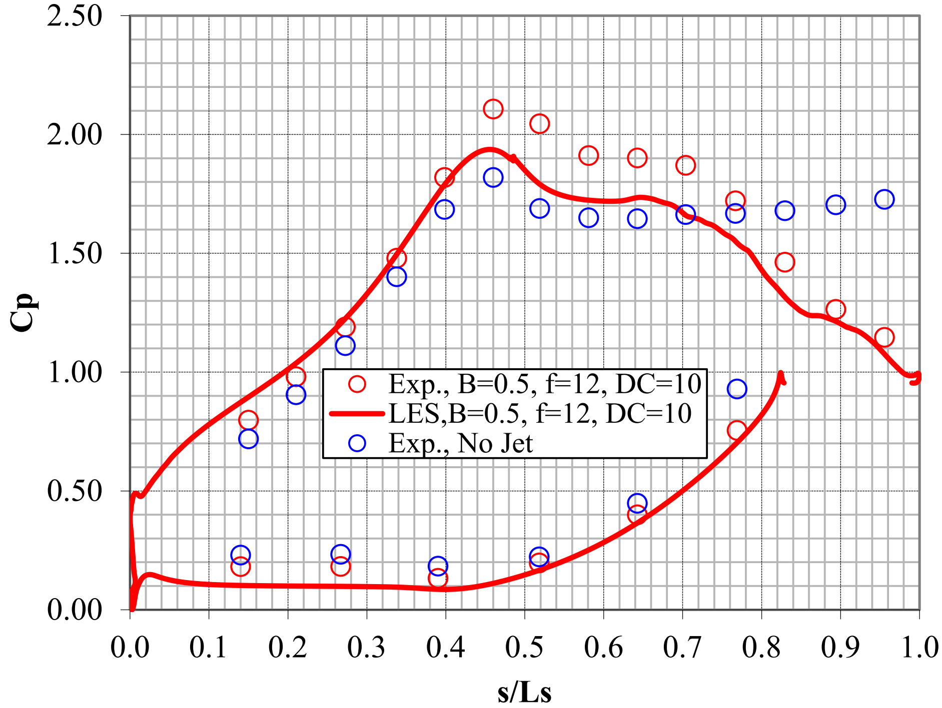

Figure 4.45: C_p for case (5) Re = 50,000, B = 0.5, f = 12 Hz (F = 0.28), DC = 10%

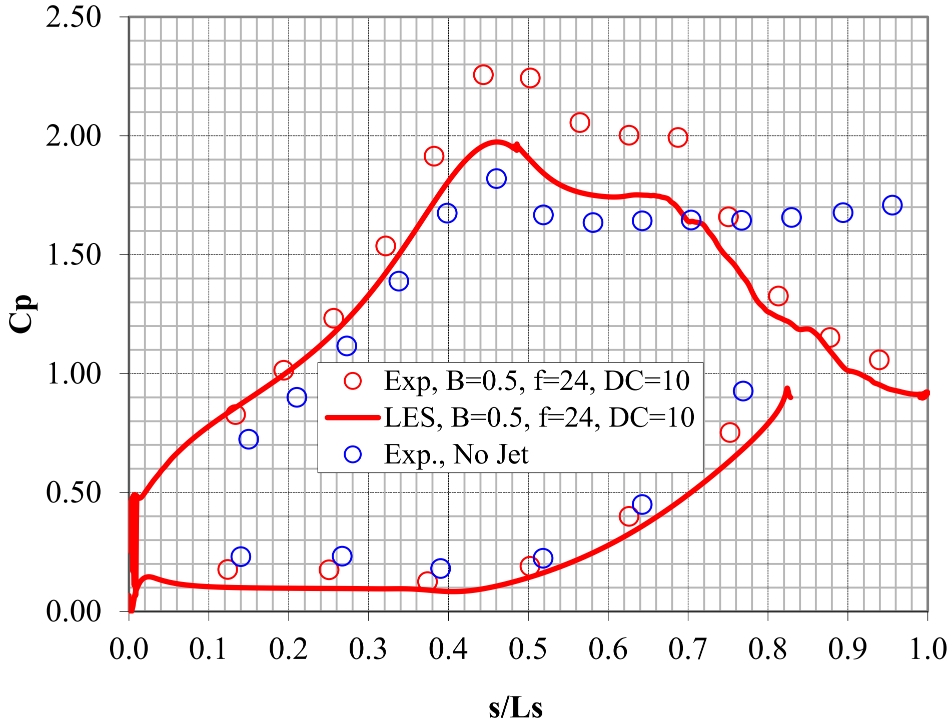

Figure 4.46: C_p for case (6) Re = 50,000, B = 0.5, f = 24 Hz (F = 0.56), DC = 10%

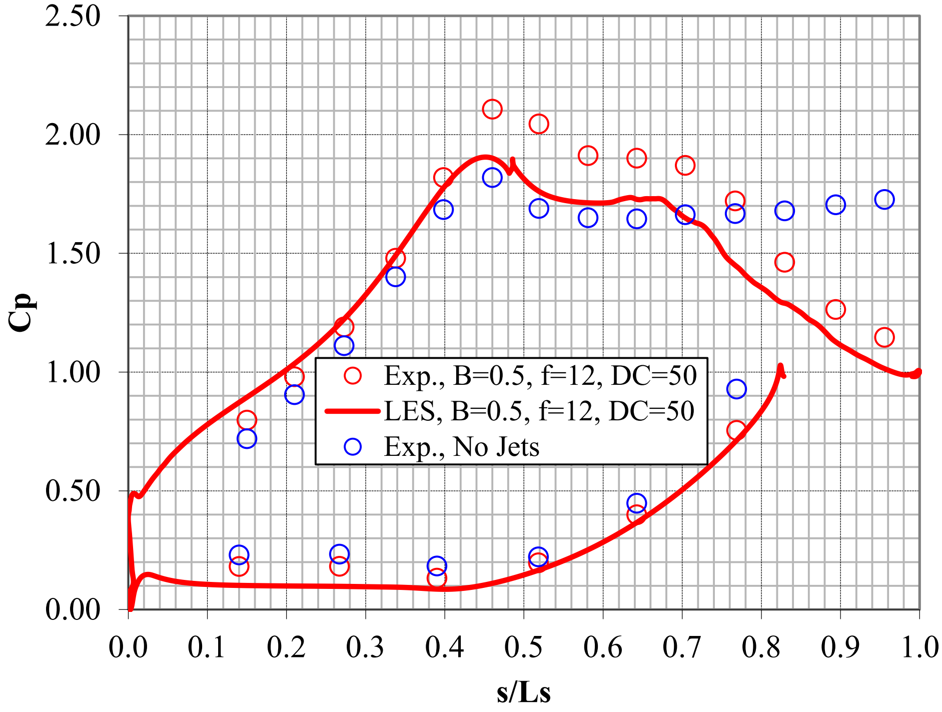

Figure 4.47: C_p for case (7) Re = 50,000, B = 0.5, f = 12 Hz (F = 0.28), DC = 50%

Figure 4.47 shows C_p for case (7) with Re =50,000, F=0.28 (f=12 Hz) and duty cycle of 50%. The figure shows flow separation starting after the suction peak with reattachment. This case yielded similar results to the case 6. It is believed that increasing the duty cycle (from 10% to 50%) could result in the same effect as increasing the frequency from 12 to 24 Hz. More discussion will be presented later on those effects when comparing pressure losses.

From the cases studied above case (6) was selected for more detailed examination since it has experimental velocity profiles for comparison.

Figure 4.48 shows the streamwise velocity contours and velocity vectors for case (6) where a small separation bubble with reattachment was observed.

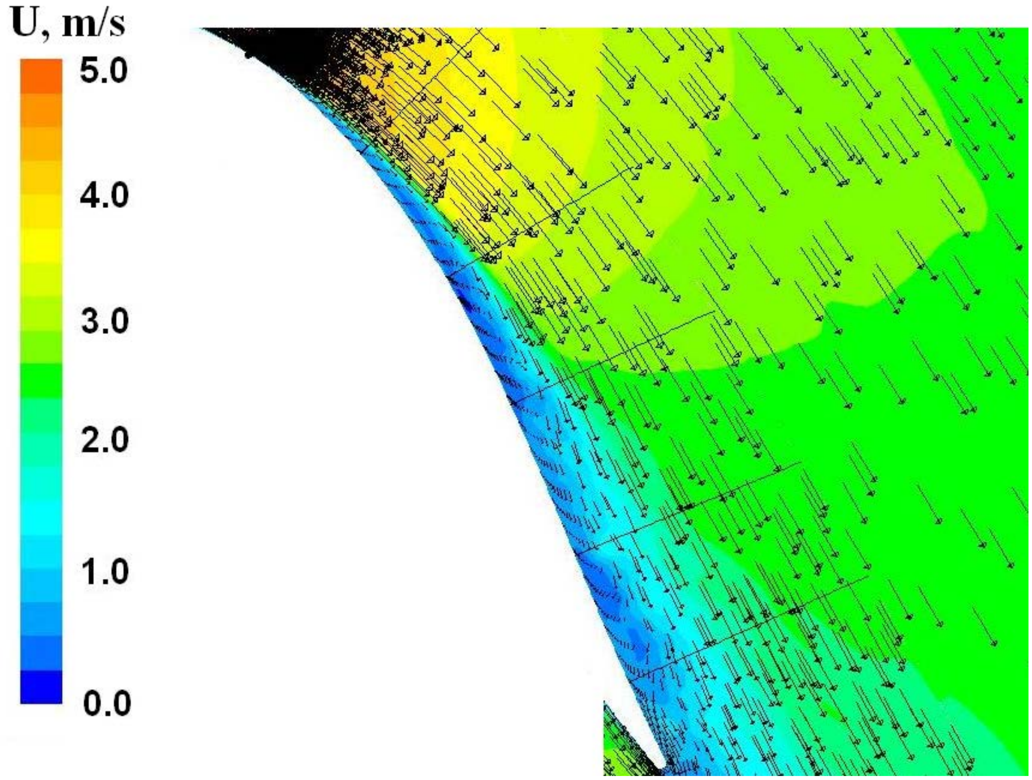

Figure 4.48: Contours of streamwise velocity and velocity vectors for Case (6), Re=50,000, B=0.5, f=24 Hz (F=0.56), DC=10%.

Velocity profiles normalized by the nominal exit velocity are plotted versus dimensionless distance from the wall in the direction normal to the wall on Fig. 4.49. The results for the 6 measurement stations (see Table 4.5) located downstream of the suction peak of the airfoil are shown. The LES shows separation starting at station 2 and small separation bubble present at all stations from 2 to 5, based on negative velocities near the wall at those locations. LES shows reattached flow at station 6. Experiment shows larger (than in LES for the same case) separation bubble present at all stations.

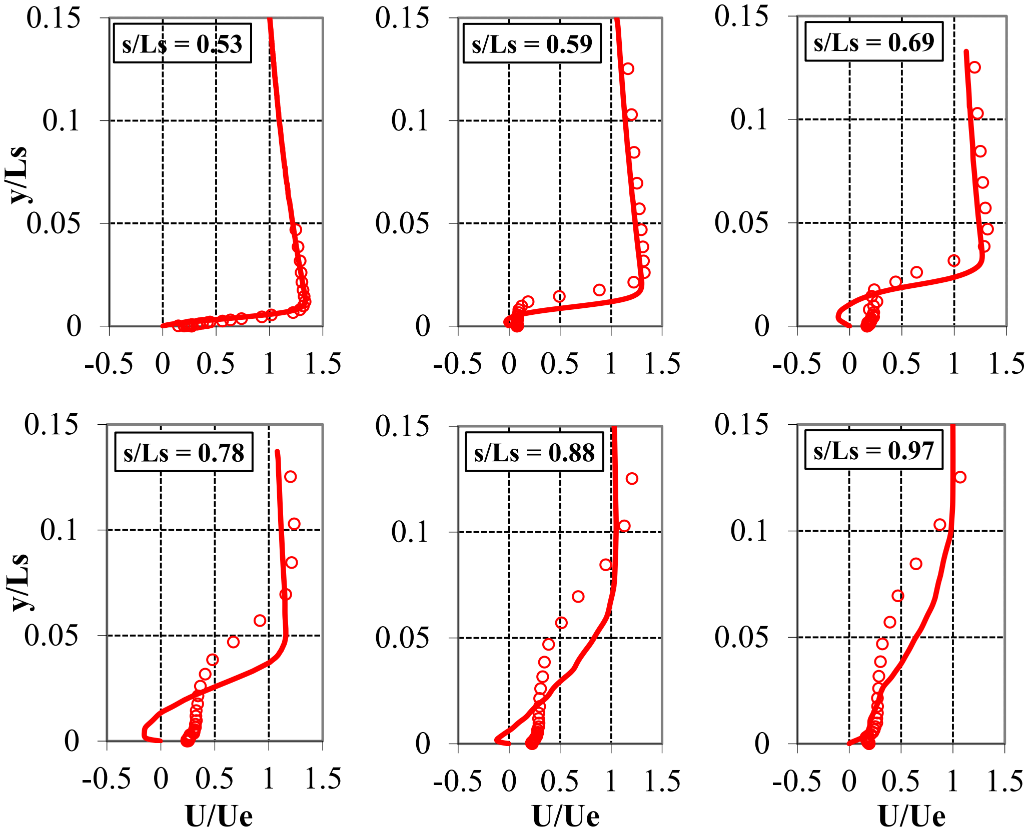

Figure 4.49: U/Ue at the 6 stations for Case (6), Re=50,000, f=24 Hz, (F=0.56), DC=10%

It seems that velocity data from experiment show rather reduction in separation rather than reattachment at downstream locations compared to uncontrolled case. Experimental C_p for the same case suggests flow reattachment at downstream locations (slope of C_p is similar to the one from LES). This could be due to the fact that C_p and velocity were measured at different times.

Profiles of the streamwise component of the RMS fluctuating velocity, u', normalized by the nominal exit velocity are plotted versus dimensionless distance from the wall in Fig. 4.50. The results for the 6 measurement stations located downstream of the suction peak of the airfoil are shown.

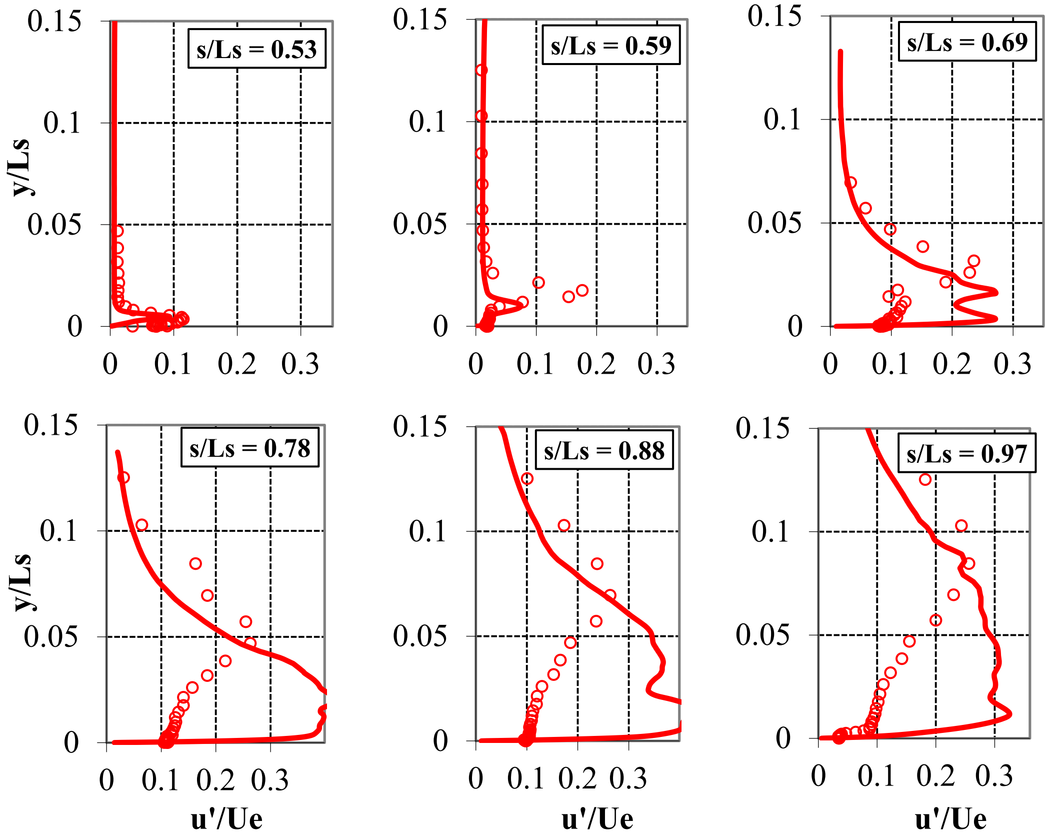

Figure 4.50: u’/Ue at the 6 stations for Case (6), Re=50,000, f=24 Hz, (F=0.56), DC=10%

In LES separation starts at station 2, and transition to turbulence starts between stations 3 and 4 (max subgird TKE, u'). The location of the peak of u' is away from the wall (between station 2 and 5) indicating the presence of a small bubble. The peak of u’ from the experiment is further away from the wall indicating a larger bubble than predicted by CFD.

For the purpose of visualization of the separated region as well as the influence of the jet's blowing ratio, iso-surfaces of the mean axial velocity Vx = 0.01 m/s are shown in Fig. 4.51 for Case (6). The reason for choosing Vx = 0.01 m/s is that this small (but not negative) value represents velocity in the shear layer of the separation bubble and helps to visualize the size of the bubble and shapes of the vortices created by the jets. The airfoil with 3 jets on the suction side near the suction peak is shown. The visualization shows very thin separation bubble. Mixing, happening in the shear layer near the wall, causes flow reattachment near the trailing edge.

Figure 4.51: Isosurface of mean Vx = 0,01 m/s for Case (6), Re=50,000, f=24 Hz, (F=0.56), DC=10%

4.6.2 Velocity Contours at Jet Exit

The CFD provides more insight into the physics of the problem compared to the experiments. Velocity contours at the jet exit for Cases (2), (5), and (6) are examined in this section. Those cases have the same Re=50,000, B=0.5 and DC=10% values but vary in frequency (F = 0.07, 0.28 and 0.56 for the three cases respectively). Figures 4.52, 4.53 and 4.54 show the contours of the velocity magnitude at the jet exit for the three cases respectively. The travelling time in the feeding tube for all cases is about 6.1 ms. The blowing time, however, vary for the three cases it is 33.3 ms for Case (2); 8.33 ms for Case (5); and 4.17 ms for Case (6). Lower frequencies correspond to the higher blowing time. Thus more time is given for the flow to reach the jet exit and exhibit parabolic profile (compare Figures 4.52 and 4.54 for example). On the other hand for the lower frequencies (with the same DC) the quiet (no blowing) time is higher and thus the case gets closer to the one with no blowing. This explains the poor flow control results (flow separation) in case (2), as shown earlier in Figure 4.42.

Figure 4.55 shows the velocity contours at the jet exit for case (7). This case has Re=50,000, B=0.5, DC=50% and F = 0.28. One additional feature exists in this case (that differs from the above cases (2), (5) and (6)) is the fact that the blowing during the 50% DC was split into two parts. The first 10% was at the nominal blowing value while that velocity was reduced to lower values at the second part of the blowing. This was done to achieve the velocity profile seen in the experiment with no cross flow present (see Figure 4.56) to match experimental blowing ratio. The square profile on Fig. 4.56 is the velocity at the jet inlet from CFD applied through User Defined Function (UDF) in Fluent. The solid red line is the velocity monitored at the point near the center of the jet at the jet exit plane from CFD. This line is very close to the red line with symbols, which represents measured velocity at the point near the center of the jet at the jet exit plane from experiment. Blowing ratio in experiment was defined as a maximum blowing ratio during the cycle, which occurred during first 10% of the cycle when the valves were open. After first 10 % of the cycle up to 50% of the cycle the "real" blowing ratio in experiment was about 0.5. From 50% of the cycle to the end of the cycle blowing ratio from experiment varied around some small value. Without modifying the inlet profile in CFD the actual amount of air blown during "on" portion of the cycle would be larger in CFD than in experiment for DC=50% cases and experimental and computational cases wouldn't be comparable.

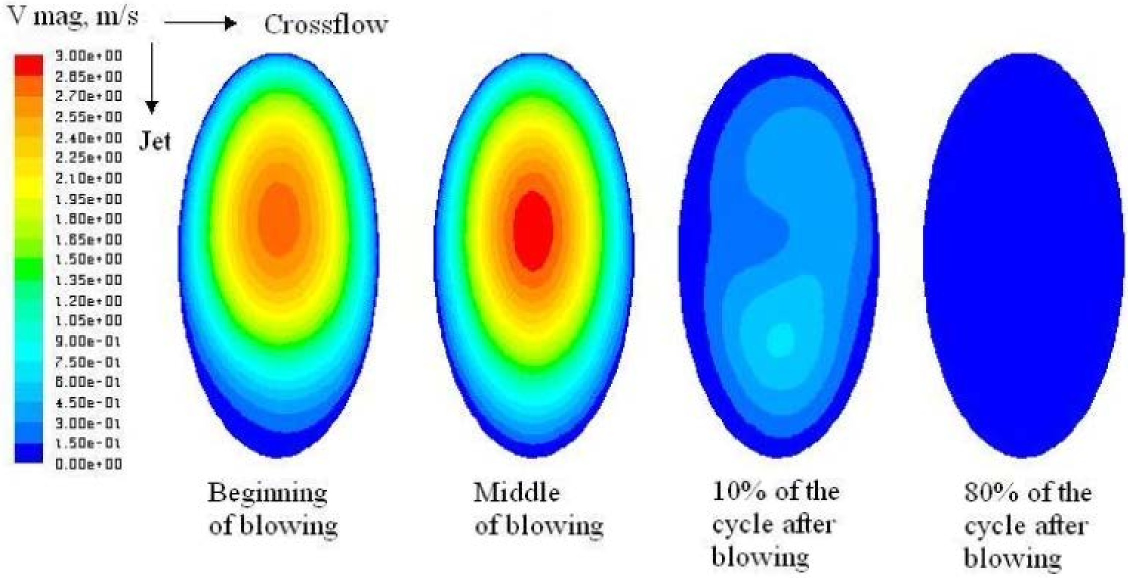

Figure 4.52: Velocity contours (m/s) at the jet exit for Case (2), Re=50,000, f=3Hz, (F=0.07), DC=10%

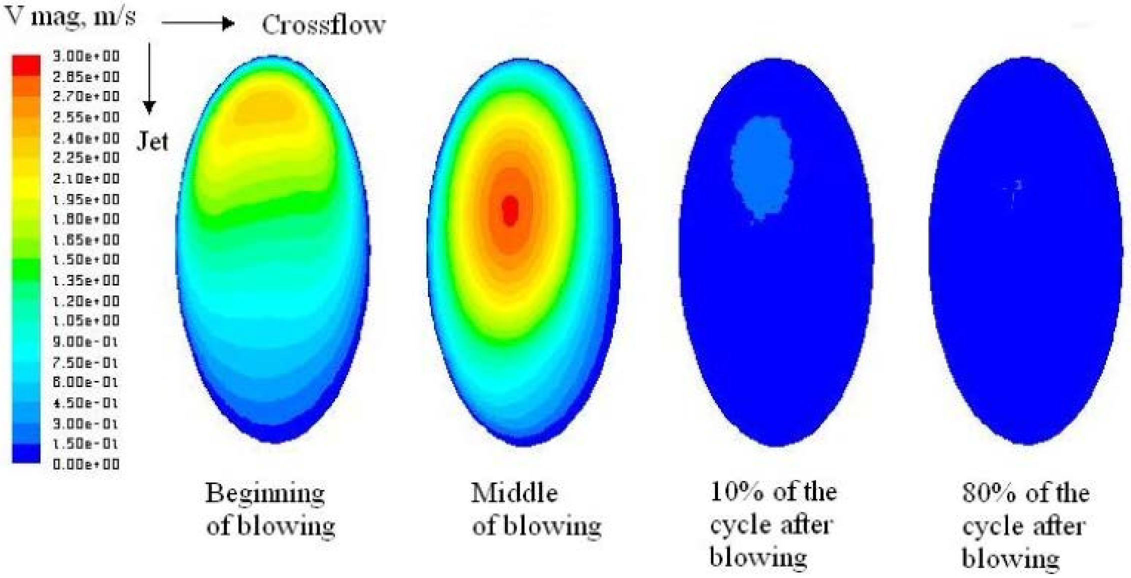

Figure 4.53: Velocity contours (m/s) at the jet exit for Case (5), Re=50,000, f=12 Hz, (F=0.28), DC=10%

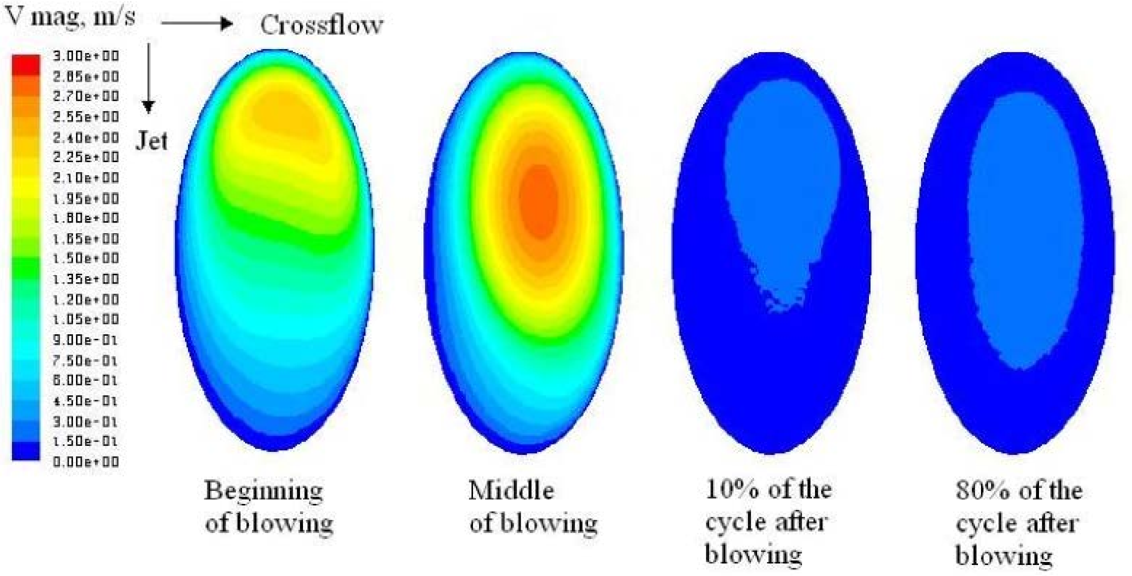

Figure 4.54: Velocity contours (m/s) at the jet exit for Case (6), Re=50,000, B=0.5, f=24 Hz, (F=0.56), DC=10%

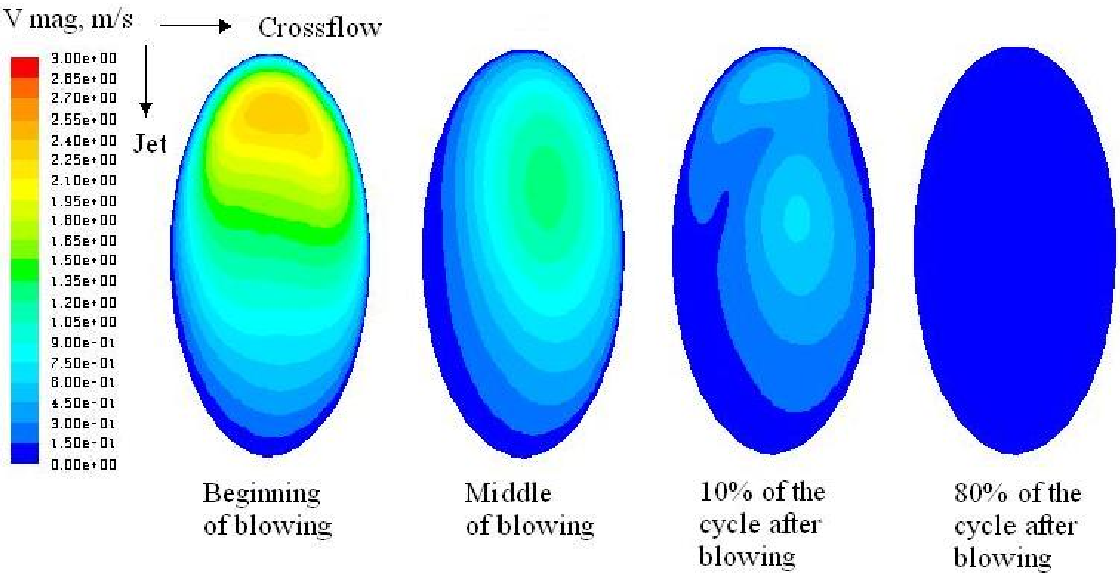

Figure 4.55: Velocity contours (m/s) at the jet exit for Case (7), Re=50,000, B=0.5, f=12Hz, (F=0.28), DC=50%

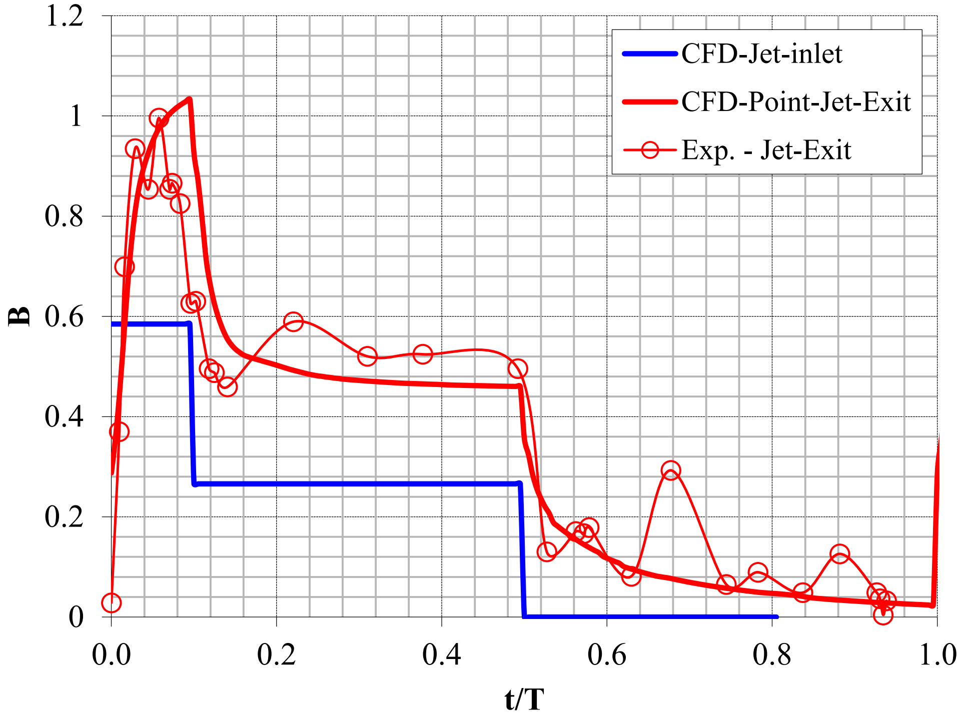

Figure 4.56: Comparison of measured and computed VGJ exit velocity with inlet velocity for B=1, f=12Hz, DC=50% case with no crossflow

4.6.3 Effect of Re and Blowing Characteristics

Table 4.9 shows the main parameters of all pulsed cases examined. The 7 pulsed cases represent a combination of the variation in Re, F and DC. The total pressure losses integrated over blade spacing, ψ_{int} are also shown in the table for both CFD and experiment.

As already known, at lower Re larger separation bubble exist and it is more difficult to remove. As Re increases as the losses decrease. Cases (4) and (6) show that despite having the same F value, more losses are encountered at lower Re.

Table 4.9: Main Parameters of all Pulsed VGJs Cases Examined (NA = Not Available)

Case	**1**	**2**	**3**	**4**	**5**	**6**	**7**
Re/1000	25	50	100	25	50	50	50
B	1.0	0.5	0.25	1.0	0.5	0.5	0.5
DC %	10	10	10	10	10	10	50
f, Hz	3	3	3	12	12	24	12
U_{aver}, m/s	2.17	4.35	8.7	2.17	4.35	4.35	4.35
F	0.14	0.07	0.035	0.56	0.28	0.56	0.28
ψ_{int}, *CFD*	0.923	1.026	0.825	0.515	0.372	0.246	0.384
ψ_{int} *Exp*	NA	NA	NA	0.346	0.356	0.237	0.313

As the value of F increases the losses decease, see cases (2), (5) and (6). It appears from both CFD and experiment that a value of F = 0.28 or above is needed to achieve reattachment and may be removal of the bubble, depending on the Re.

The analysis of cases (6) and (7) suggests that the larger duty cycle could compensate for the lower frequency (case 7). However, the effect of increasing the frequency appears to be stronger than increasing the value of DC.

The comparison between, CFD and Experiment for $\psi_{int,}$ is reasonable for cases (5), (6) and (7). As for Case (4) the larger differences is due to the fact that flow is not fully attached and therefore there is no complete periodicity across the cascade in the experiment. Therefore the experimental value is expected to be lower than the CFD one.

4.6.4 Flow visualization utilizing the *Q*-Criterion

In this section second invariant of velocity gradient tensor (*Q*-criterion) is used for vortex visualization to study effects of pulsed VGJs.

The definition of *Q*-criterion is:

$$Q = -\frac{1}{2}\frac{\partial \bar{u}_i}{\partial x_j}\frac{\partial \bar{u}_j}{\partial x_i} = -\frac{1}{2}\left(\bar{S}_{ij}\bar{S}_{ij} - \bar{\Omega}_{\mathrm{ij}}\bar{\Omega}_{\mathrm{ij}}\right),$$

where $\bar{S}_{ij} = \frac{1}{2}\left(\frac{\partial \bar{u}_i}{\partial x_j} + \frac{\partial \bar{u}_j}{\partial x_i}\right)$, $\bar{\Omega}_{\mathrm{ij}} = \frac{1}{2}\left(\frac{\partial \bar{u}_i}{\partial x_j} - \frac{\partial \bar{u}_j}{\partial x_i}\right)$.

In order to show the effect of frequency the *Q*-Criterion was used for two cases: Case (2)-low frequency, and Case (6)-high frequency. This case of Re=50,000 and B=0.5 under steady blowing demonstrated separation bubble present on the airfoil (see section 4.5). Furthermore at the low frequency (case (2)) separation without reattachment was observed from the time-averaged data (see Figure 4.42). At the higher frequency (case (6)) flow separation followed by the reattachment is seen from the time averaged data (see Figure 4.46).

Figure 4.56a shows the *Q*-Criterion contours colored by x-velocity (m/s), for case (2) at different times in the cycle. At the beginning of the blowing large separation bubble is present and the shear layer above the jet is relatively relaxed. In the middle of the blowing the large separated region remains above the airfoil surface but the boundary layer downstream of the jet is energized. Shortly after jet shut down (t=10% of the cycle), the boundary layer in the vicinity of the jet starts to relax with the energized region moving downstream. This energized region causes shrinkage of the separation bubble downstream of the jet, but it doesn't have neither enough energy or time to travel further downstream to cause reattachment. At t = 80 % of the cycle after jet's shutdown, the flow looks very similar to steady blowing where a large separation bubble does exist as indicated above.

Figure 4.56b shows the Q-Criterion contours colored by x-velocity (m/s), for Case (6) at different times in the cycle. At the beginning of the blowing there is a large separation bubble present near the trailing edge of the airfoil. During blowing the separated region is traveling downstream and the flow becomes attached in that region. Right after shutdown of the jet (t=10% of the cycle time) an overall smaller separation region is observed and the flow starts to reattach at the trailing edge. At t = 80 % of the cycle after jet's shutdown, the flow is attached at the trailing edge, but separated region starts to show up upstream.

Seven different cases were examined experimentally and computationally in this section in order to study LPT flow control using pulsed VGJ's for L1A airfoil. These cases represent a combination of variation in Re (25,000, 50,000 and 100,000), based on the suction surface length and the nominal exit velocity from the cascade, B (from 0.25 to 1.0), F (from 0.035 to 0.56) and duty cycle (10% and 50%). The data were obtained for the pressure distribution along the airfoil and downstream in the wake as well as velocity profiles at 6 different stations downstream of the suction peak.

All cases examined did show flow separation with no jet blowing. At lower Re a larger separation bubble exists and accordingly it is more difficult to remove. As Re increases as separation bubbles size is reduced and the losses decrease. As the value of F increases the losses decease and it appears that a value of F of 0.28 or above is sufficient to cause reattachment and may be removal of the bubble, depending on the Re.

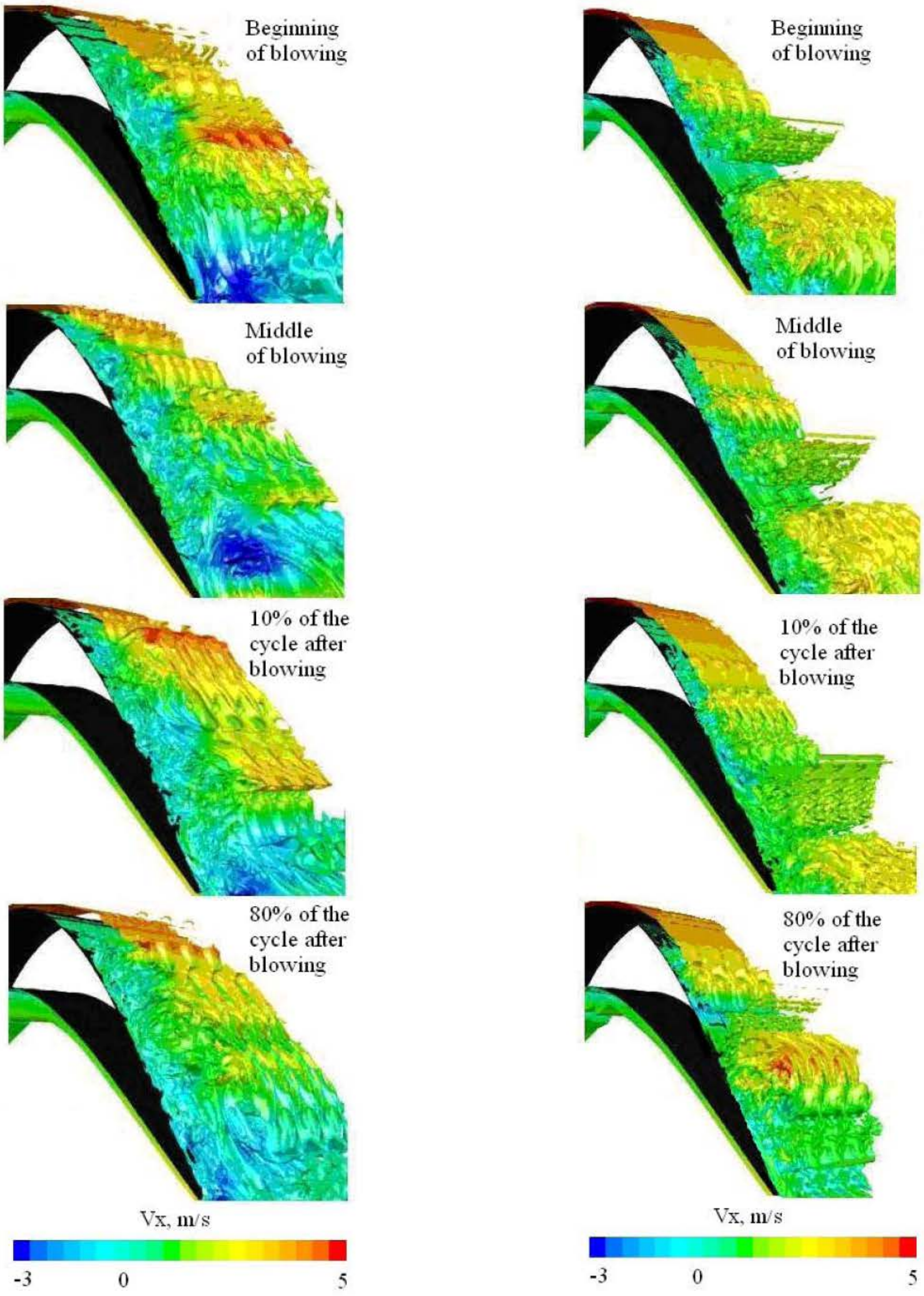

a) b)

Figure 4.56: Iso-surfaces of the Q-criterion colored by Vx (m/s) at different times in the cycle for: a) Case (2), Re=50,000, B=0.5, f=3Hz (F=0.07), DC=50%; b) Case (6), Re=50,000, B=0.5,f=24Hz (F=0.56), DC=10%

Two cases examined did indicate that the higher DC could compensate for the lower F value. However, the effect of increasing the frequency appears to be stronger than increasing the DC value. The comparison between CFD and experiment for C_p, velocity profiles and pressure losses is reasonable for all cases investigated.

Flow visualization via iso-surfaces of second invariant of velocity gradient tensor (Q-criterion) was used to demonstrate the effect of frequency. The visualization clearly illustrates how a separation bubble will persist in the low frequency case and the disturbances created from the jet flow have neither enough energy nor time to travel further downstream to cause reattachment. On the other hand, the higher frequency case did exhibit a penetration of the disturbance created by the jet into the separated region and flow reattachment at the trailing edge. It appears that the jet was capable of breaking the large bubble into smaller ones with reattachments in between at times.

CHAPTER V

CONCLUDING REMARKS

5.1 Film cooling

The flow and heat transfer mechanisms that govern the effectiveness of the pulsed jet film cooling of flat plates were examined. This was done by varying: 1) pulsation frequency, 2) blowing ratio and 3) jet geometry. Film cooling effectiveness, predicted by the realizable $k - \varepsilon$ turbulence model (RKE) was in the closest agreement with the experiment for the cylindrical film hole geometry.

Pulsed jets performance significantly depends on geometry and blowing ratio. Pulsation helps to lower the amount of cool air from compressor, which is desirable for film cooling applications. However, for the conditions in which steady blowing performs well, pulsation considerably decreases the film cooling effectiveness. For the cases, where steady blowing gives poor results (e.g. higher blowing ratios), pulsation helps to increase time and distance averaged effectiveness, while coolant amount decreases. Although pulsation didn't bring overall benefit to film cooling, there are cases where pulsed jets resulted in larger values of film cooling effectiveness compared to the steady blowing case. Therefore, present results might be useful for evaluation of the effect of pulse frequency on film cooling effectiveness in real life gas turbine applications, where jets pulse naturally due to the pressure fluctuations in the engine.

One suggestion for future work would be to computationally investigate the effect of the upstream wake (simulating effect of the upstream airfoil) on the pulsed jets performance. Another suggestion is to conduct computational pulsed jets film cooling study for actual airfoil geometry and possibly use more advanced turbulence modeling (Large Eddy Simulation) or Direct Numerical Simulation.

5.2 Flow control

Three turbulence models (SKW-sst, V2F and Trans-sst) were used to study separation and transition of the flow over highly loaded L1A airfoil at Re = 25,000, 100,000 and 300,000, based on exit velocity and suction side length. The results were compared with experimental data for the pressure distribution and velocity profiles on the airfoil, as well as for the pressure losses.

At Re = 25,000 all models and experiment showed large separation bubble starting at $s/L_s = 0.5$ and no reattachment. Predicted pressure losses were larger than experimental ones since separation was partially suppressed in experiment by the tailboard which resulted in non-periodic pressure distribution downstream of the airfoil. The velocities at six stations along the suction surface were predicted reasonably well by all turbulence models tested with Trans-sst model doing better overall. The location of the peak of u' predicted between stations 3 and 4 ($0.69 < s/L_s < 0.78$) was used for calculation of transition location. It agreed with experimental data for the same Re (within the range of experimental uncertainty) and with correlation.

At Re=100,000, similar to the case of Re=25,000, large separation bubble was observed in CFD and experiment with transition location moved upstream ($s/L_s = 0.59$). The results from the Trans-sst model for the velocity profiles and pressure losses were in the better agreement with experimental data compared to the other turbulence models tested. However, this model showed some under prediction of the pressure coefficient downstream of the suction peak.

At Re = 300,000 very small separation bubble was observed at $s/L_s = 0.6$ followed by transition to turbulence and quick reattachment of the boundary layer. All turbulence models tested showed excellent agreement between predicted and experimental pressures and velocities. Computed pressure distribution downstream of the airfoils showed shift of the peaks of the pressure loss coefficient to the right compared to experimental ones. This could, possibly, be explained by the fact that experimental cascade consisted of seven blades, when periodic boundary conditions were assumed in CFD. To resolve this issue a full cascade calculation would be necessary, as well as possible grid refinement in the wake region.

Location of transition calculated from Trans-sst model agrees with experimental value within the range of experimental uncertainty.

When level of free stream turbulence was raised at the inlet from 0.8% in Low Free Stream Turbulence Intensity (LFSTI) cases to 5% in High Free Stream Turbulence Intensity (HFSTI) cases flow reattachment was already observed at Re = 100,000. Under HFSTI conditions flow was separated in the Re = 25,000 case and was attached at all locations in the Re = 300,000 case.

Large Eddy Simulation (LES) with dynamic subgrid-scale kinetic energy model of Kim and Menon (1997) was used to model turbulence in the flow control cases with Vortex Generator Jets (VGJs). This advanced model was selected since Reynolds Averaged Navier-Stokes (RANS) models were not capable of capturing effects of VGJs (i.e. predicted large separation in cases where reduction of separation or flow reattachment was observed in experiment).

Ability of steady blown VGJs to eliminate or reduce separation was found to be highly dependent on the Re and blowing ratio (B).

In Re = 25,000 cases both low (B = 1) and high (B = 3) blowing ratios tested resulted in flow separation with no reattachment. At the low blowing ratio (B = 1) separation started early between stations 1 and 2 with transition to turbulence taking place between stations 3 and 4. At high blowing ratio (B = 3) separation onset was delayed to near station 3 with transition to turbulence starting early at station 1. Despite early transition in the B = 3 case VGJs were not able to prevent separation because of overall low turbulence levels at this low Re (25,000).

Similar observations were made for Re = 50,000 cases ran, where low blowing ratio (B = 0.5) resulted in flow separation at station 1 with transition to turbulence happening between stations 3 and 4. High blowing ratio (B = 2) for the same Re resulted in flow separation at station 3 and transition to turbulence upstream of station 1. No flow reattachment was observed in this case.

Cases of Re = 100,000 with steady blown VGJs resulted in flow separation with reattachment at the low blowing ratio (B = 0.25). At this Re, in contrast with lower Re cases studied, high blowing ratio (B = 1) resulted in an attached flow on the whole airfoil suction side length.

In the cases where steady blown VGJs were not capable of preventing or reducing separation (low blowing ratio cases) jet pulsation was found beneficial with the value of dimensionless frequency of F = 0.28 or above. Lower frequencies resulted in flow separation, since prolonged no-blowing period brought those cases close to the cases with no flow control. Duty cycle (DC) of 10% proved to be sufficient to control separation at values of F = 0.28 and above. An observation was made that larger DC could, actually, compensate for lower frequency, however, the effect of increasing the frequency appeared to be stronger than increasing DC value.

A suggestion for the future work is to conduct a computational study of the wake effect from the upstream airfoil on the pulsed VGJs performance.

BIBLIOGRAPHY

Acharya, S., Tyagi, M., and Honda, A., 2001. "Flow and Heat Transfer for Film Cooling," In Heat Transfer in Gas Turbine Systems, Vol. 934, Annals of the New York Academy of Sciences, pp. 110-125.

Andreopoulos, J., and Rodi, W., 1984, "Experimental Investigation of Jets in a Crossflow," *Journal of Fluid Mechanics,* **138**, pp. 93-127.

ANSYS Fluent Documentation, 2009.

Bohl, D.G. and Volino, R.J., 2006, “Experiments with Three- Dimensional Passive Flow Control Devices on Low-Pressure Turbine Airfoils,” ASME *Journal of Turbomachinery*, **128**, pp. 251-260.

Bons, J.P., Hansen, L.C., Clark, J.P., Koch, P.J., and Sondergaard, R., 2005, “Designing Low-Pressure Turbine Blades With Integrated Flow Control,” ASME Paper GT2005-68962.

Bons, J.P., Pluim, J., Gompertz, K. and Bloxham, M., 2008, “The Application of Flow Control to an Aft-Loaded Low Pressure Turbine Cascade with Unsteady Wakes” *ASME Paper GT2008-50864*

Bons, J.P., Reimann, D., and Bloxham, M., 2008, “Separated Flow Transition on an LP Turbine Blade With Pulsed Flow Control,” ASME *Journal of Turbomachinery*, **130**, 021014.

Bons, J.P., Sondergaard, R., and Rivir, R.B., 2001, “Turbine Separation Control Using Pulsed Vortex Generator Jets,” ASME *Journal of Turbomachinery*, **123**, pp. 198-206.

Bons, J.P., Sondergaard, R., and Rivir, R.B., 2002, “The Fluid Dynamics of LPT Blade Separation Control Using Pulsed Jets,” ASME *Journal of Turbomachinery*, **124**, pp. 77-85.

Bradshaw, P., Ferriss, D.H., and Atwell, N.P., 1967, “Calculation of Boundary-Layer Development Using the Turbulent Energy Equation,” *Journal of Fluid Mechanics*, **28**(3), pp. 593-616.

Clark, J.P. *Private Communication*, Air Force Research Laboratory, 2007.

Coulthard, S.M., Volino, R.J., and Flack, K.A., 2006, "Effect of Jet Pulsing on Film Cooling, Part 1: Effectiveness and Flowfield Temperature Results," ASME *Journal of Turbomachinery*, **129**, pp.232-246.

Crawford, M.E., and Kays, W.M., 1976, “STAN5 – A Program for Numerical Computation of Two-Dimensional Internal and External Boundary Layer Flows,” NASA CR-2742.

Davis, R.L., Carter, J.E., and Reshotko, E., 1985, “Analysis of Transitional Separation Bubbles on Infinite Swept Wings,” AIAA Paper 85-1685.

Durbin, P.A., 1995, "Separated Flow Computations with the k-ε-v^2 Model," *AIAA Journal,* **33(4)**:659-664.

Ekkad, S.V., Ou, S., and Rivir, R.B., 2006, "Effect of Jet Pulsation and Duty Cycle on Film Cooling from a Single Jet on a Leading Edge Model," ASME *Journal of Turbomachinery*, **128**, pp. 564-571.

Eldredge, R. G., and Bons, J. P., 2004, “Active Control of a Separating Boundary Layer With Steady Vortex Generating Jets—Detailed Flow Measurements,” AIAA Paper 2004-751.

Garg, V.K., 2002, “Low-Pressure Turbine Separation Control - Comparison with Experimental Data” *ASME Paper GT-2002-30229*

Gostelow, J.P., Walker, G.J., Solomon, W.J., Hong, G., and Melwani, N., 1997, “Investigation of the Calmed Region Behind a Turbulent Spot,” ASME *Journal of Turbomachinery*, **119**, pp. 802-809.

Gross, A., Fasel, H.F., 2008 “Strategies for Simulating Flow Through Low-Pressure Turbine Cascade,” ASME *Journal of Fluids Engineering*, **130,** 111105.

Hatman, A., and Wang, T., 1999, “A Prediction Model for Separated Flow Transition,” ASME *Journal of Turbomachinery*, **121**, pp. 594-602.

Hourmouziadis, J., 1989, “Aerodynamic Design of Low Pressure Turbines,” AGARD Lecture Series 167.

Howell, R. J., 1999, “Wake - Separation Bubble Interactions in Low Reynolds Number Turbomachinery,” Ph.D. dissertation, Cambridge University, Cambridge, UK.

Huang, J., Corke, T., and Thomas, F., 2003, “Plasma Actuators for Separation Control on Low Pressure Turbine Blades,” AIAA Paper 2003-1027.

Hughes, J.D. and Walker, G.J., 2001, “Natural Transition Phenomena on an Axial Compressor Blade,” ASME *Journal of Turbomachinery*, **123**, pp. 392-401.

Hyams, D.G., and Leylek, J.H., 2000, "A Detailed Analysis of Film-Cooling Physics: Part III - Streamwise Injection with Shaped Holes," ASME *Journal of Turbomachinery*, **122,** pp.122-132.

Ibrahim, M.B., Kartuzova, O. and Volino, R.J., 2008, “Experimental and Computational Investigations of Separation and Transition on a Highly Loaded Low Pressure Turbine Airfoil: Part 1 – Low Freestream Turbulence Intensity”, *ASME Paper IMECE2008-68879*

Ibrahim, M.B., Kartuzova, O., and Volino, R.J., 2009, “LES and URANS Computational Investigations of LPT Blade (L1A) Separation Control using Vortex Generator Jets,” Proceedings *of Turbulence, Heat and Mass Transfer 6*, 2009, Rome, Italy.

Johnston, J.P. and Nishi, M., 1990, “Vortex Generator Jets. Means for Flow Separation Control”, *AIAA Journal*, **28**, pp. 989-994.

Kim, S.E., 2004, “Large eddy simulation using unstructured meshes and dynamic subgridscale turbulence models,” *Technical Report AIAA-2004-2548, American Institute of Aeronautics and Astronautics*, 34th Fluid Dynamics Conference and Exhibit

Kim, W.W. and Menon, S., 1997, “Application of the localized dynamic subgrid-scale model to turbulent wall-bounded flows” *Technical Report AIAA-97-0210, American Institute of Aeronautics and Astronautics*, 35th Aerospace Sciences Meeting, Reno, NV, 1997.

Lakshminarayana, B., 1996, *Fluid Dynamics and Heat Transfer of Turbomachinery*, Wiley, New York.

Langtry, R.B., Menter, F.R., Likki, S.R., Suzen, Y.B., Huang, P.G., and Völker, S., 2006, “A Correlation based Transition Model using Local Variables Part II: Test Cases and Industrial Applications,” ASME *Journal of Turbomachinery*, **128**, pp. 423-444.

Launder, B.E., and Spalding, D.B., 1974, "The Numerical Computation of Turbulent Flows," Computer Methods in Applied Mechanics and Engineering, **3**, pp. 269-289.

Mahallati, A., and Sjolander, S.A., 2007, “Aerodynamics of a Low-Pressure Turbine Airfoil at Low Reynolds Numbers Part 2 --Blade-Wake Interaction,” ASME Paper GT2007-27348.

Mahallati, A., Sjolander, S.A., McAuliffe, B.R., and Praisner, T.J., 2007, “Aerodynamics of a Low-Pressure Turbine Airfoil at Low-Reynolds Numbers Part 1 -- Steady Flow Measurements, ASME Paper GT2007-27347.

Mayhew, J. E., 1999, *An Experimental Investigation of the Effect of Freestream Turbulence on Film Cooling Using Thermochromic Liquid Crystal Thermography*, Ph.D. Dissertation, University of California, Davis, CA.

Mayle, R.E., 1991, “The Role of Laminar-Turbulent Transition in Gas Turbine Engines,” ASME *Journal of Turbomachinery*, **113**, pp. 509-537

McAuliffe, B.R. and Sjolander, S.A., 2004, “Active Flow Control Using Steady Blowing for a Low-Pressure Turbine Cascade,” ASME *Journal of Turbomachinery*, **126**, pp. 560-569.

McQuilling, M., and Jacob, J., 2004, “Effect of Chord Location on Separation Control With Vortex Generator Jets on Low Pressure Turbine Blades,” AIAA Paper 2004-2205.

Menter, F.R., 1994, “Two-Equation Eddy-Viscosity Turbulence Models for Engineering Applications”, *AIAA Journal*, **32**, pp. 1598-1605.

Menter, F.R., Langtry R.B., Likki, S.R. Suzen, Y.B. Huang P.G. and Völker, S., 2006, “A Correlation Based Transition Model Using Local Variables – Part I: Model Formulation,” *ASME Journal of Turbomachinery*, **128**, pp. 413-422.

Muldoon, F., Acharya, S., 2007, "Computation of Pulsed Film Cooling," ASME paper GT2007-28156.

Piomelli, U. and Chasnov, J.R., 1995, Large-Eddy Simulations: Theory and Applications. *Turbulence and Transition Modeling, lecture notes from the ERCOFTAC/IUTAM* summer school held in Stockholm, 12-20 June, 1995.

Postl, D. Gross, A. and Fasel, H.F., 2004, “Numerical Investigation of Active Control for Low-Pressure Turbine Blade Separation,” *AIAA2004-750, Proceedings of 42nd AIAA Aerospace Science Meeting and Exhibit*, January 5-8, 2004, Reno, Nevada, USA

Praisner, T.J., and Clark, J.P., 2007, “Predicting Transition in Turbomachinery – Part 1: A Review and New Model Development,” ASME *Journal of Turbomachinery*, **129**, pp. 1-13.

Rizzetta, D.P. and Visbal, M.R., 2005, "Numerical Simulation of Separation Control for Transitional Highly Loaded Low-Pressure Turbines", *AIAA Journal*, **43**, pp.1958-1967.

Roberts, S.K, and Yaras, M.I., 2006, "Effects of Surface-Roughness Geometry on Separation-Bubble Transition," ASME *Journal of Turbomachinery*, **128**, pp. 349-356.

Schlichting, H., 1979, *Boundary Layer Theory*, 7th ed., McGraw-Hill, New York.

Schulte, V., and Hodson, H.P., 1998, "Prediction of the Becalmed Region for LP Turbine Profile Design," ASME *Journal of Turbomachinery*, **120**, pp. 839-846.

Sharma, O.P., Ni, R.H., and Tanrikut, S., 1994, "Unsteady Flow in Turbines," AGARD Lecture Series 195, Paper No. 5.

Shih, T.H., Liou, W.W., Shabbir, A., Yang, Z., Zhu, J., 1994 "A New k-ε Eddy Viscosity Model for High Reynolds Number Turbulent Flows," *Computers Fluids,* **24**, pp. 227-238.

Singh, N., 2005, "A Study of Separated Flow through a Low-Pressure Turbine Cascade," MS thesis, University of Cincinnati, Cincinnati, OH.

Sinha, A.K., Bogard D.G., and Crafword, M.E., 1991, "Film Cooling Effectiveness Downstream of a Single Row of Holes with Variable Ratio," ASME *Journal of Turbomachinery*, **113**, pp. 442-449.

Suzen, Y. B., Huang, P. G., Volino, R.J., Corke, T.C., Thomas, F. O., Huang, J, Lake, J. P., King, P.I., 2003, "A Comprehensive CFD Study of Transitional Flows in Low-Pressure Turbines Under a Wide Range of Operating Conditions," AIAA Paper AIAA2003-3591.

Suzen, Y.B., Huang, P.G., Ashpis, D.E., Volino, R.J., Corke, T.C., Thomas, F.O., Huang, J., Lake, J.P. and King, P.I., 2007, "A Computational Fluid Dynamics Study of Transitional Flows in Low-Pressure Turbines Under a Wide Range of Operating Conditions," ASME *Journal of Turbomachinery*, **129**, pp. 527-541.

Volino, R.J, Kartuzova, O., and Ibrahim, M., 2008a, "Experimental and Computational Investigations of Separation and Transition on a Highly Loaded Low Pressure Turbine Airfoil: Part 2 – High Freestream Turbulence Intensity," ASME Paper IMECE2008-68776.

Volino, R.J. Kartuzova, O., and Ibrahim, M.B., 2009, "Experimental and Computational Investigations of Low-Pressure Turbine Separation Control using Vortex Generator Jets," *GT2009-59983, Proceedings of ASME Turbo Expo 2009: Power for Land, Sea and Air GT2009*, June 8-12, 2009, Orlando, Florida, USA

Volino, R.J., 2002a, "Separated Flow Transition under Simulated Low-Pressure Turbine Airfoil Conditions: Part 1 –Mean Flow and Turbulence Statistics," ASME *Journal of Turbomachinery*, **124**, pp. 645-655.

Volino, R.J., 2002b, "Separated Flow Transition under Simulated Low-Pressure Turbine Airfoil Conditions: Part 2 – Turbulence Spectra," ASME *Journal of Turbomachinery*, **124**, pp. 656-664.

Volino, R.J., 2003a, "Passive Flow Control on Low-Pressure Turbine Airfoils," ASME *Journal of Turbomachinery*, **125**, pp. 754-764.

Volino, R.J., 2003b, "Separation Control on Low-Pressure Turbine Airfoils Using Synthetic Vortex Generator Jets," ASME *Journal of Turbomachinery*, **125**, pp. 765-777.

Volino, R.J., 2008b, "Separated Flow Measurements on a Highly Loaded Low-Pressure Turbine Airfoil", ASME Paper GT2008-51445.

Volino, R.J., and Bohl, D.G., 2004, "Separated Flow Transition Mechanisms and Prediction with High and Low Freestream Turbulence under Low Pressure Turbine Conditions," ASME Paper GT2004-63360.

Volino, R.J., and Bohl, D.G., 2005, "Structure of Oscillating Vortex Generator Jets," Proceedings of the Fourth International Symposium on Turbulence and Shear Flow Phenomena, **2**, pp. 589-594.

Volino, R.J., and Hultgren, L.S., 2001, "Measurements in Separated and Transitional Boundary Layers Under Low-Pressure Turbine Airfoil Conditions," ASME *Journal of Turbomachinery*, **123**, pp. 189-197.

Volino, R.J., and Simon, T.W., 1997, "Velocity and Temperature Profiles in Turbulent Boundary Layers Experiencing Streamwise Pressure Gradients," ASME *Journal of Heat Transfer*, **119**, pp. 433-439.

Volino, R.J., Schultz, M.P., and Pratt, C.M., 2001, "Conditional Sampling in a Transitional Boundary Layer Under High Free-Stream Turbulence Conditions," ASME *Journal of Fluids Engineering*, **125**, pp. 28-37.

Walters, D.K., and Leylek, J.H., 1997, "A Systematic Computational Methodology Applied to a Three-Dimensional Film-Cooling Flowfield," ASME *Journal of Turbomachinery*, **119,** pp.777-785.

Walters, D.K., and Leylek, J.H., 2000, "A Detailed Analysis of Film-Cooling Physics: Part 1 - Streamwise Injection with Cylindrical Holes," ASME *Journal of Turbomachinery*, **122,** pp.102-112.

Wilcox, D.C., 1998, Turbulent Modeling for CFD, DCW Industries, Inc., La Canada, California.

Wills, J.A.B., 1962, "The Correction of Hot-Wire Readings for Proximity to a Solid Boundary," *Journal of Fluid Mechanics*, **12**, pp. 65-92.

Yaras, M. I., 2002, "Measurements of the Effects of Freestream Turbulence on Separation-Bubble Transition," ASME Paper GT-2002-30232.

Zhang, X.F. and Hodson, H., 2005, "Combined Effects of Surface Trips and Unsteady Wakes on the Boundary Layer Development of an Ultra-High-Lift LP Turbine Blade", *ASME Journal of Turbomachinery*, **127**, pp. 479-488.

Zhang, X.F., and Hodson, H., 2007, "Effects of Reynolds Number and Freestream Turbulence Intensity on the Unsteady boundary Layer Development on an Ultra-High-Lift LPT airfoil," ASME Paper GT2007-27274

Zhang, X.F., Vera, M., Hodson, H., and Harvey, N., 2007, "Separation and Transition Control on an Aft-Loaded Ultra- High-Lift LP Turbine Blade at Low Reynolds Numbers: Low- Speed Investigation," ASME *Journal of Turbomachinery*, **128**, pp. 517-527.

Zoric, T., Popovic, I., Sjolander, S.A., Praisner, T., and Grover, E., 2007, "Comparative Investigation of Three Highly Loaded LP Turbine Airfoils: Part I -- Measured Profile and Secondary Losses at Design Incidence," ASME Paper GT2007-27537.

REPORT DOCUMENTATION PAGE	*Form Approved* *OMB No. 0704-0188*

1. REPORT DATE *(DD-MM-YYYY)* 01-09-2012	**2. REPORT TYPE** Final Contractor Report	**3. DATES COVERED** *(From - To)* January 2007 to September 2010

4. TITLE AND SUBTITLE A Computational Study for the Utilization of Jet Pulsations in Gas Turbine Film Cooling and Flow Control Final Report	**5a. CONTRACT NUMBER** NNC07IA10I; N00189-07-P-A253
	5b. GRANT NUMBER DE-FC26-06NT42853
	5c. PROGRAM ELEMENT NUMBER
6. AUTHOR(S) Kartuzova, Olga, V.	**5d. PROJECT NUMBER**
	5e. TASK NUMBER
	5f. WORK UNIT NUMBER WBS 561581.02.08.03.47.02.01
7. PERFORMING ORGANIZATION NAME(S) AND ADDRESS(ES) Cleveland State University 2121 Euclid Avenue Cleveland, Ohio 44115	**8. PERFORMING ORGANIZATION REPORT NUMBER** E-18087
9. SPONSORING/MONITORING AGENCY NAME(S) AND ADDRESS(ES) National Aeronautics and Space Administration Washington, DC 20546-0001	**10. SPONSORING/MONITOR'S ACRONYM(S)** NASA
	11. SPONSORING/MONITORING REPORT NUMBER NASA/CR-2012-217416

12. DISTRIBUTION/AVAILABILITY STATEMENT

Unclassified-Unlimited
Subject Categories: 02, 05, 07, and 34
Available electronically at http://www.sti.nasa.gov
This publication is available from the NASA Center for AeroSpace Information, 443-757-5802

Notice for Copyrighted Information

This manuscript has been authored under a NASA Interagency Agreement No. NNC07IA10I (through U.S. Navy Agreement No. N00189-07-P-A253). The United States Government has a nonexclusive, irrevocable, worldwide license to prepare derivative works, publish or reproduce this manuscript, and allow others to do so, for United States Government purposes. Any publisher accepting this manuscript for publication acknowledges that the United States Government retains such a license in any published form of this manuscript. All other rights are retained by the copyright owner. Attachments are reprinted by permission.

13. SUPPLEMENTARY NOTES

This report was submitted as a dissertation in partial fulfillment of the requirements for the degree Doctor of Engineering in Mechanical Engineering to the Cleveland State University, Department of Mechanical Engineering, Cleveland, Ohio, May 2010. Grant technical monitors, Anthony J. Strazisar, Office of the Chief Scientist, Glenn Research Center, organization code ASOO, James D. Heidmann, Aeropropulsion Division, Glenn Research Center, organization code RTTO, David E. Ashpis, Aeropropulsion Division, Glenn Research Center, organization code RTTO, ashpis@nasa.gov

14. ABSTRACT

This report is the second part of a three-part final report of research performed under an NRA cooperative Agreement contract. The first part is NASA/CR-2012-217415. The third part is NASA/CR-2012-217417. Jets have been utilized in various turbomachinery applications in order to improve gas turbines performance. Jet pulsation is a promising technique because of the reduction in the amount of air removed from compressor. In this work two areas of pulsed jets applications were computationally investigated using the commercial code Fluent (ANSYS, Inc.); the first one is film cooling of High Pressure Turbine (HPT) blades and second one is flow separation control over Low Pressure Turbine (LPT) airfoil using Vortex Generator Jets (VGJ). Using pulsed jets for film cooling purposes can help to improve the effectiveness and thus allow higher turbine inlet temperature. Effects of the film hole geometry, blowing ratio and density ratio of the jet, pulsation frequency and duty cycle of blowing on the film cooling effectiveness were investigated. As for the low-pressure turbine (LPT) stages, the boundary layer separation on the suction side of airfoils can occur due to strong adverse pressure gradients. The problem is exacerbated as airfoil loading is increased. Active flow control could provide a means for minimizing separation under conditions where it is most severe (low Reynolds number), without causing additional losses under other conditions (high Reynolds number). The effects of the jet geometry, blowing ratio, density ratio, pulsation frequency and duty cycle on the size of the separated region were examined in this work. The results from Reynolds Averaged Navier-Stokes and Large Eddy Simulation computational approaches were compared with the experimental data.

15. SUBJECT TERMS

Gas turbines; Turbomachinery; Turbine; Low pressure turbine; Turbulence; Flow control; Synthetic jets; CFD; LES; Turbulence models; Wakes; Separation; Vortex generated jets; Film cooling

16. SECURITY CLASSIFICATION OF:			**17. LIMITATION OF ABSTRACT**	**18. NUMBER OF PAGES**	**19a. NAME OF RESPONSIBLE PERSON** STI Help Desk (email:help@sti.nasa.gov)
a. REPORT U	**b. ABSTRACT** U	**c. THIS PAGE** U	UU	182	**19b. TELEPHONE NUMBER** *(include area code)* 443-757-5802